Local Maximum Entropy Approximation-based Modelling of the Canine Heart

Ritesh Rao Rama

Submitted to the Department of Civil Engineering,
University of Cape Town, in partial fulfilment of the requirements
for the degree of Master of Science in Engineering.

25th November 2012

PLAGIARISM FORM

I know the meaning of plagiarism and declare that all the work in the documents, save for which is properly acknowledge is my own.

Name : RITESH RAO RAMA

Student ID : RMXRIT001

Date : 25th November 2012

Signature :

ABSTRACT

Local Maximum Entropy (LME) method [1] is an approximation technique which has been known to have good approximation characteristics. This is due to its non-negative shape functions and the weak Kronecker delta property which allow the solutions to be continuous and smooth as compared to the Moving Least Square method (MLS) which is used in the Element Free Galerkin method (EFG). The method is based on a convex optimisation scheme where a non-linear equation is solved with the help of a Newton algorithm, implemented in an in-house code called SESKA. In this study, the aim is to compare LME and MLS and highlight the differences.

Preliminary benchmark tests of LME are found to be very conclusive. The method is able to approximate deformation of a cantilever beam with higher accuracy as compared to MLS. Moreover, its rapid convergence rate, based on a Cook's membrane problem, demonstrated that it requires a relatively coarser mesh to reach the exact solution.

With those encouraging results, LME is then applied to a larger non-linear cardiac mechanics problem. That is simulating a healthy and a myocardial infarcted canine left ventricle (LV) during one heart beat. The LV is idealised by a prolate spheroidal ellipsoid. It undergoes expansion during the diastolic phase, addressed by a non-linear passive stress model [2] which incorporates the transversely isotropic properties of the material. The contraction, during the systolic phase, is simulated by Guccione's active stress model [3]. The infarct region is considered to be non-contractile and twice as stiff as the healthy tissue. The material loss, specially during the necrotic phase, is incorporated by the use of a homogenisation approach.

Firstly, the loss of the contraction ability of the infarct region counteracts the overall contraction behaviour by a bulging deformation where the occurrence of high stresses are noted. Secondly, with regards to the behaviour of LME, it is found to feature high convergence rate and a decrease in computation time with respect to MLS. However, it is also observed that LME is quite sensitive to the nodal spacing in particular for an unstructured nodal distribution where it produces results that are completely unreliable.

ACKNOWLEDGEMENTS

My gratitude first goes to my supervisor, Dr Sebastian Skatulla, for his inestimable and invaluable critics, counselling and advice throughout the duration of the whole dissertation. He was always available to my requests and inquiries.

Secondly, my thanks go to Dr Dieter Legner whose assistance were very useful in understanding some of the cardiac mechanic aspects.

I am also grateful to the CHPC for providing me funding to undertake this research.

Special thanks goes to James Mbewu in helping me to understand SESKA, Roshan Bhurtha for introducing me to LaTeX and Harish Appa in proof-reading my thesis .

My deepest gratitude also goes towards my family. Their moral and financial supports were, beyond doubt, indispensable.

And finally, I wish to thanks all those who have helped me, in one way or the other.

Contents

List of Figures

List of Tables

Chapter 1

Introduction

1.1 Problem Statement

Approximation functions are special functions that have the ability to approximate a complex function based on a set of known values, so-called *sample points*. Their objective is to fit an approximated curve as closely as possible to the exact one. The difference between the approximated and exact solution determines the accuracy of the method that produces the approximation functions. One of the properties that directly affect the accuracy level is the locality of the approximation scheme. Global approximation functions, which make use of all the points inside the domains, usually produces solutions with larger errors than those which are defined locally (i.e defined by a small set of neighbouring points in the domain). Applied to a physical problem, the approximation functions have a direct impact on the solution quality. Usually they need to at least satisfy some of the most primordial properties, which are:

- The order of continuity should correspond to the occurring differential order of the function to approximated,
- The approximation function should satisfy the partition of unity property,
- Increase of sample point density, so-called *discretisation refinement*, should lead to convergence of approximated solution to the exact solution,
- And the approximation function should, at least, possess the weak Kronecker delta property as this is advantageous when enforcing essential boundary conditions.

In this project, a mesh-free method is dealt with, where the interaction between the nodes are no longer rigid as in the Finite Element method (FEM). The method has been mainly introduced to alleviate problems encountered in mesh refinement and to have higher smoothness compared to FEM. The in-house code SESKA (Appendix A), used in this thesis. has implemented the Element Free Galerkin (EFG) method which employs the Moving Least Square (MLS) approximation (developed by Lancaster and Salkauskas [9]). The approximation functions are derived by minimising the difference between the approximated solution and the exact one.

Even though MLS is quite robust when solving any kinds of engineering problems, it unfortunately has two major disadvantages: The shape functions do not possess the weak Kronecker delta property and are negative near the boundary nodes. The latter is said to be responsible in increasing computational time which causes instability problems and produces results that lack smoothness [10].

Alternatives to MLS already exist. For example Sukumar et al [11] stated that the Radial Basis functions and the natural neighbour interpolation have been employed but do not yield many additional advantages and need to be investigated further. The Finite sphere method [12] and the hp-cloud method [13] could also be used, but these methods make it difficult to directly impose the boundary conditions. However, one new method that has been developed by Arroyo and Ortiz [1], called the Local Maximum Entropy (LME), seems to hold a lot of promise. Built-up on a convex optimisation scheme using information theory from Jaynes [14], the method directly imposes a set of constraints on the approximation functions. In that way, the latter satisfy some properties such as positivity, weak Kronecker delta and form a partition of unity. Preliminary tests, carried out by Sukumar and Wright [11] and Arroyo and Ortiz [1], have shown that LME has a lot of advantageous aspects such as faster convergence and computation time without sacrificing the smoothness of the solution. However, these tests have been carried out using only small benchmark problems. Here, it will be studied how LME behave in large non-linear problems as compare to MLS.

One particular problem that has been selected for testing is related to the modelling of myocardial infarction which is an increasing health problem worldwide. Due to an under-supply of blood, the cardiomyocytes in the affected region permanently lose their ability to contract. This in turn gradually weakens the overall heart function. An accurate computational model is the basis for obtaining a better understanding of the heart mechanics, in particular, how myocardial infarction affects its pumping performance. After implementing LME in the in-house code SESKA, a canine's left ventricle (LV) model is set up from the spheroidal coordinate system along with a predefined infarct region. To model the passive mechanical behaviour, we employ an orthotropic strain energy function of Usyk et al [15]. During the systole, the active stress model from Guccione [3] is used and the focus is laid on the iso-volumetric contraction phase. Obtaining tangible results can help in predicting the heart's behaviour and therefore assist in finding and testing numerous therapies in order to achieve better treatments for myocardial infarction.

1.2 Aim and Objectives

The aim of this project is to implement the Local Maximum Entropy approximation. After validating the method with some benchmark tests, the latter will then be used to simulate an infarcted left ventricle. This will yield results that can ultimately help us to understand LME's performance with respect to MLS and also the impact of myocardial infarction on the performance of the heart.

1.3 Outline

With the problem statement along with the aim and objectives given, a brief outline of each of the upcoming chapters will now be provided in order to understand how the research is carried out.

In Chapter 2, the Continuum Mechanics principles are introduced briefly as these will be heavily used in the following chapters.

Chapter 3 looks at how the MLS approximants are derived and calculated. It also consists of introducing the advantages and limitation of MLS basis.

LME is then defined in Chapter 4. In order to fully understand how it has been obtained, some mathematical concepts of convex optimisation schemes are first elaborated. Then, LME's shape functions are derived and their properties are looked at. Finally, an implementation algorithm is provided.

Chapter 5 gives a description of how the different behaviours of a normal heart have been studied and simulated in literature. The myocardial infarction process is explained followed by the passive constitutive laws. The Eikonal and the active stress model is then described as it will be used in modelling the contraction of the LV in the systolic phase.

In Chapter 6, the benchmarking of the LME is carried out in order to validate its implementation and also to correlate the results with those observed in literature. In addition, a composite beam is setup to demonstrate that the Cardiac Mechanic constitutive laws work as expected.

The results of the left ventricle that has been carried out with both LME and MLS are presented in Chapter 7. The analysis is done by firstly comparing the effect of an infarct on a ventricle and secondly how the LME approximation fared against MLS.

Finally, the conclusions, based on the analysis, are given in chapter 8.

And Chapter 9 will then provide some ideas on how the actual work can be extended to cover other aspects of cardiac mechanics or the LME approximation method.

Chapter 2

Continuum Mechanics

Continuum mechanics is a field consisting of solid and fluids mechanics. In this field, the fundamental assumption made is that if one continuously magnifies a specific piece of a material, the underlying molecular structure is generalised by the overlying material properties. Thus, each point can be now be subjected to any kind of stress and strain, based on certain physical and material laws or kinematic quantities, in the same way as any structure, irrespective of its size.

From this, Continuum Mechanics can now provides the means to analyse a body, being subjected to different boundary conditions, by utilising any kind of discretisation strategies. In this chapter, fundamental equations related to non-linear continuum mechanics will be introduced and the relations of these equations to stress and strain will be highlighted as they have been employed quite extensively afterwards. For more detailed descriptions and derivations, the reader may find the following book useful: Mase and Mase [16].

2.1 Kinematics

Consider a body, $\mathcal{B}$, in a 3D Euclidean vector space characterised as the reference state (i.e the undeformed configuration). $\mathcal{B}$ is parametrised by the Cartesian coordinates X_1, X_2 and X_3 where the associated basis vectors are denoted by e_1, e_2 and e_3. After being subjected to certain boundary conditions, the body, at time t, in its deformed state is referred as $\mathcal{B}_t$. To describe this transition of state, a non-linear deformation mapping $\varphi_t : \mathcal{B} \to \mathcal{B}_t$ is introduced, enabling us to define the relation of a material point in the reference configuration $\mathbf{X} \in \mathcal{B}$ and $\mathbf{x} \in \mathcal{B}$:

$$\mathbf{x} = \varphi(\mathbf{X}, t). \tag{2.1}$$

With φ being known, the corresponding invertible linear tangent map, $\mathbf{F}$, labelled as the deformation gradient, is established as the gradient of φ. For the determinant of $\mathbf{F}$, it must hold that the Jacobian must be positive ($J > 0$) for an admissible deformation.

$$J = \det \mathbf{F} = \det(\text{Grad } \varphi) \tag{2.2}$$

whereby the following operators with respect to reference and current configuration are considered here and in the following:

Operator	Configuration	
	Reference	Current
Gradient	$\text{Grad}(\bullet) = \frac{\partial}{\partial \mathbf{X}}(\bullet) = \boldsymbol{\nabla}(\bullet)$	$\text{grad}(\bullet) = \frac{\partial}{\partial \mathbf{x}}(\bullet) = \boldsymbol{\nabla}_t(\bullet)$
Divergence	$\text{Div}(\bullet) = \frac{\partial}{\partial X_i}(\bullet) \cdot \mathbf{e}_i = \boldsymbol{\nabla} \cdot (\bullet)$	$\text{div}(\bullet) = \frac{\partial}{\partial x_i}(\bullet) \cdot \mathbf{e}_i = \boldsymbol{\nabla}_t \cdot (\bullet)$

Table 2.1: *Gradient and Divergence operation in the Reference and Current configuration*

With the displacement field given by $\mathbf{u}(\mathbf{X}, t) = \mathbf{x}(\mathbf{X}, t) - \mathbf{X}$, the deformation gradient, $\mathbf{F}$, can be alternatively defined as

$$\mathbf{F} = 1 + \text{Grad } \mathbf{u}. \tag{2.3}$$

Any change in time is termed the local rate of change and expressed as,

$$\frac{\partial}{\partial t}(\bullet). \tag{2.4}$$

Therefore, the overall time rate of change is

$$\frac{D}{Dt}(\bullet) = \frac{\partial}{\partial t}(\bullet) + \frac{\partial}{\partial x_i}(\bullet)\frac{dx_i}{dt}. \tag{2.5}$$

Correspondingly, the Jacobian, which defines the change of volumes from different configuration states, can also vary with respect to time:

$$\dot{J} = J \,\text{div}\, \dot{\mathbf{x}}. \tag{2.6}$$

For later usage, we also take into account that a surface element in its material configuration dA with its unit normal $\mathbf{n}$ is related to its counterpart in the spacial configuration da with its unit normal $\boldsymbol{\nu}$ by

$$\boldsymbol{\nu} da = \det(\mathbf{F})\mathbf{F}^{-T}\mathbf{n}\, dA, \tag{2.7}$$

and a volume element in the undeformed configuration dV to its counterpart in the current configuration dv by

$$dv = \det(\mathbf{F})\, dV = J\, dV. \tag{2.8}$$

The change in length of a line after deformation would require the difference between the length in the undeformed configuration, $d\mathbf{x}^2$, and the deformed one, $d\mathbf{X}^2$:

$$d\mathbf{x}^2 - d\mathbf{X}^2 = (\mathbf{F}^T\mathbf{F} - \mathbf{1}) : (d\mathbf{X} \otimes d\mathbf{X}). \tag{2.9}$$

Based on the above, the right *Cauchy-green* tensor is defined as:

$$\mathbf{C} = \mathbf{F}^T\mathbf{F}. \tag{2.10}$$

In turn, the *Green-strain* tensor, symmetric in nature, can now also be introduced as a function of $\mathbf{C}$:

$$\mathbf{E} = \frac{1}{2}(\mathbf{C} - \mathbf{1}) = \frac{1}{2}(\mathbf{F}^T\mathbf{F} - 1). \tag{2.11}$$

The right *Cauchy-green* tensor can also be expressed as,

$$\mathbf{C} = \mathbf{U^2}. \tag{2.12}$$

where $\mathbf{U}$ is the stretch tensor. With the eigenvalues of $\mathbf{U}$, the scalar invariants of $\mathbf{C}$ are:

$$I_1^C = tr(\mathbf{C}) = \lambda_1^2 + \lambda_2^2 + \lambda_3^2 \tag{2.13}$$

$$I_2^C = \frac{1}{2}(tr\ \mathbf{C})^2 - tr(\mathbf{C}^2) = \lambda_1^2\lambda_2^2 + \lambda_2^2\lambda_3^2 + \lambda_3^2\lambda_1^2 \tag{2.14}$$

$$I_3^C = \det(\mathbf{C}) = \lambda_1^2\lambda_2^2\lambda_3^2. \tag{2.15}$$

2.2 Stress Measures

Bodies subjected to forces will undergo deformation, resulting in a redistribution of forces throughout the body. Consider a body, $\mathcal{B}$, subjected to a body force, $\mathbf{b}$, and a surface force, $\mathbf{t}^{(\boldsymbol{\nu})}$, normally known as the traction vector, acting on a surface with a unit normal, $\boldsymbol{\nu}$. Then the following relation holds,

$$\mathbf{t}^{(\boldsymbol{\nu})}(\mathbf{x}, t) = \boldsymbol{\sigma}^T(\mathbf{x}, t)\boldsymbol{\nu}(\mathbf{x}, t) \tag{2.16}$$

with $\boldsymbol{\sigma}$ defined as the *Cauchy stress* tensor in the spatial coordinate of $\mathbf{x}$. If the stress state of the same point in the undeformed configuration is to be found, then the element surface to be considered is dA with a unit normal of $\mathbf{n}$:

$$\mathbf{t}^{(\boldsymbol{n})}(\mathbf{X}, t) = \mathbf{P}(\mathbf{X}, t)\,\mathbf{n}(\mathbf{X}, t) \tag{2.17}$$

with $\mathbf{P}$ being the *first Piola-Kirchhoff stress* tensor which is now a function of the coordinate $\mathbf{X}$. $\mathbf{P}$ relates stresses with forces in the current configuration as acting on areas in the reference configuration and the deformation gradient can be applied to map the forces to the reference configuration. In that case, the new stress tensor is defined as the *second Piola-Kirchhoff stress* tensor, $\mathbf{S}$:

$$\mathbf{P} = \mathbf{FS}. \tag{2.18}$$

Using $\boldsymbol{\sigma}$, $\mathbf{P}$ can be defined differently. This is done by first assuming that a force, $\mathbf{f}$, acting on da is not different to the one applied on dA. Therefore,

$$d\mathbf{f} = \mathbf{P}\mathbf{n}\,dA = \boldsymbol{\sigma}^T\boldsymbol{\nu}da = \boldsymbol{\sigma}^T\det(\mathbf{F})\mathbf{F}^{-T}\mathbf{n}\,dA. \tag{2.19}$$

Where, the first Piola-Kirchhoff stress can also be calculated from:

$$\mathbf{P} = \det(\mathbf{F})\boldsymbol{\sigma}^T\mathbf{F}^{-T}. \tag{2.20}$$

2.3 Balance Law of Continuum Mechanics

If a body is subjected to perturbations of any form (e.g force, temperature or magnetic field), then the following fundamental physical laws can be used to describe the behaviour of the body:

- **The law of Conservation of Mass** ensures that there is no mass loss or gain when the body change from the undeformed to the deformed configuration
- **The law of Linear and Angular Momentum Conservation** is related to Newton's Second Law which defines the rate of change of linear and angular momentum over time, resulting in force and momentum.
- **The law of Energy Conservation** is related to the Principle law of Energy which states that energy can neither be created nor destroyed but can only change forms. However, in this project, we focus mainly on the conversion of energy into deformations.

2.3.1 Conservation of mass

Consider a continuum body $\mathcal{B}_t$ at time t or any arbitrary sub-body, whose mass is calculated by:

$$m = \int_{\mathcal{B}_t} \rho(\mathbf{x}, t)\, dv \tag{2.21}$$

with ρ being in the current configuration. The principle of conservation of mass states that the body will conserve its total mass throughout its motion,

$$\dot{m} = \frac{d}{dt} \int_{\mathcal{B}_t} \rho(\mathbf{x}, t)\, dv = \int_{\mathcal{B}_t} \{\dot{\rho}(\mathbf{x}, t) + \rho(\mathbf{x}, t)\, J \operatorname{div} \dot{\mathbf{x}}\}\, dv = 0. \tag{2.22}$$

Since $\mathcal{B}_t$ is arbitrary,

$$\dot{\rho}(\mathbf{x}, t) + \rho(\mathbf{x}, t)\, J\, , \operatorname{div} \dot{\mathbf{x}} = 0. \tag{2.23}$$

As the mass remains the same, irrespective of the different configurations it went through,

$$m = \int_{\mathcal{B}_t} \rho(\mathbf{x}, t)\, dv = \int_{\mathcal{B}} \rho_0(\mathbf{X})\, dV = 0 \tag{2.24}$$

where, ρ_0, is the density in the reference configuration. Using the Jacobian,

$$\int_{\mathcal{B}} \{\rho(\mathbf{X}, t)\, J - \rho_0(\mathbf{X})\}\, dV = 0. \tag{2.25}$$

Knowing that $\mathcal{B}$ is arbitrary, we are left with,

$$\rho(\mathbf{X}, t)\, J = \rho_0(\mathbf{X}). \tag{2.26}$$

If the derivative of the above is taken with respect to time,

$$\frac{d}{dt}\left(\rho(\mathbf{X}, t)\, J\right) = 0 \qquad \text{as} \qquad \frac{d}{dt}(\rho_0(\mathbf{X})) = 0. \tag{2.27}$$

Another useful equation that is proposed to evaluate the material derivative,

$$\frac{d}{dt}\int_{\mathcal{B}_t}\rho(\mathbf{x},t)\,A(\mathbf{x},t)\,dv=\int_{\mathcal{B}_t}\rho(\mathbf{x},t)\,\dot{A}(\mathbf{x},t)\,dv \tag{2.28}$$

where A is a field of unit mass.

2.3.2 Linear Momentum Conservation

If a material continuum body, $\mathcal{B}$, is subjected to a body force $\mathbf{b}$ and a surface traction $\mathbf{t}^{\boldsymbol{\nu}}$ is applied to a boundary surface, $\partial\mathcal{B}$, the principle of linear momentum states that the rate of change of the linear momentum equals the total resultant force acting on the body:

$$\frac{d}{dt}\int_{\mathcal{B}_t}\rho(\mathbf{x},t)\,\dot{\mathbf{x}}\,dv=\int_{\partial\mathcal{B}_t}\mathbf{t}^{(\boldsymbol{\nu})}(\mathbf{x},t)\,da+\int_{\partial\mathcal{B}_t}\mathbf{b}(\mathbf{x},t)\,dv. \tag{2.29}$$

Introducing the *Cauchy stress lemma* and making use of the Gauss divergence theorem, Eq 2.29 is transformed into the global equation of motion:

$$\int_{\mathcal{B}_t}\left\{\rho(\mathbf{x},t)\,\ddot{\mathbf{x}}-\operatorname{div}\boldsymbol{\sigma}^T-\mathbf{b}(\mathbf{x},t)\right\}\,dv=0. \tag{2.30}$$

The local form of the equation of motion is obtained if one acknowledges that $\mathcal{B}_t$ is arbitrary,

$$\operatorname{div}\boldsymbol{\sigma}^T+\mathbf{b}(\mathbf{x},t)=\rho(\mathbf{x},t)\,\ddot{\mathbf{x}}. \tag{2.31}$$

For constant velocity field, $\dot{\mathbf{x}}(\mathbf{x},t)$, the acceleration field, $\ddot{\mathbf{x}}$, is zero, reducing Eq 2.31 to the equilibrium equation:

$$\operatorname{div}\boldsymbol{\sigma}^T+\mathbf{b}(\mathbf{x},t)=\mathbf{0}. \tag{2.32}$$

The above steps can be repeated for quantities in the reference configuration. The global equation is now:

$$\frac{d}{dt}\int_{\mathcal{B}_t}\rho_0\dot{\mathbf{x}}(\mathbf{X},t)\,dV=\int_{\partial\mathcal{B}_t}\mathbf{t}^{(\boldsymbol{n})}(\mathbf{X},t)\,dA+\int_{\partial\mathcal{B}_t}\mathbf{b}(\mathbf{x},t)\,dV. \tag{2.33}$$

With the elimination of the traction vector and applying the Gauss' divergence theorem,

$$\int_{\mathcal{B}_t}\left\{\rho_0\ddot{\mathbf{x}}(\mathbf{X},t)\;-\operatorname{div}\mathbf{P}-\mathbf{b}(\mathbf{X},t)\right\}\,dV=\mathbf{0}. \tag{2.34}$$

Since $\mathcal{B}_t$ is arbitrary, to get the localised equation of motion which shall now be called the *Lagrangian equation of motion*:

$$\operatorname{div}\mathbf{P}+\mathbf{b}(\mathbf{X},t)\,dV=\rho_0\ddot{\mathbf{x}}(\mathbf{X},\mathbf{t}). \tag{2.35}$$

Finally, the Lagrangian equilibrium equation with constant velocity field is given by,

$$\operatorname{div}\mathbf{P}+\mathbf{b}(\mathbf{X},t)\,dV=\mathbf{0}. \tag{2.36}$$

2.3.3 Angular Momentum Conservation

Angular momentum is defined as a moment of the linear momentum about a particular reference point, which is usually taken as the origin of a coordinate system:

$$\frac{d}{dt}\int_{\mathcal{B}_t} \mathbf{x} \times \rho(\mathbf{x},t)\,\dot{\mathbf{x}}\,dv = \int_{\partial\mathcal{B}_t} \mathbf{x}\times\mathbf{t}^{(\boldsymbol{\nu})}(\mathbf{x},t)\,da + \int_{\mathcal{B}_t} \mathbf{x}\times\mathbf{b}(\mathbf{x},t)\,dv. \tag{2.37}$$

Normalising the integrands by taking the material derivative, using the *Cauchy stress* tensor $\boldsymbol{\sigma}$ and resorting to the Gauss' divergence theorem,

$$\int_{\mathcal{B}_t} \left\{\mathbf{x} \times \rho(\mathbf{x},t)\,\ddot{\mathbf{x}} - \mathrm{div}(\mathbf{x}\times\boldsymbol{\sigma}^T) + \mathbf{x}\times\mathbf{b}(\mathbf{x},t)\right\}\,dv = \mathbf{0} \tag{2.38}$$

with

$$\mathrm{div}(\mathbf{x}\times\boldsymbol{\sigma}^T) = \mathrm{Grad}\,\mathbf{x}\times\boldsymbol{\sigma}^T + \mathbf{x}\times\mathrm{div}\boldsymbol{\sigma}^T. \tag{2.39}$$

Simplifying the above, Eq 2.39 is transformed into:

$$\int_{\mathcal{B}_t} \left\{\mathbf{x} \times \rho(\mathbf{x},t)\,\ddot{\mathbf{x}} + \boldsymbol{\epsilon} : \boldsymbol{\sigma}^T - \mathbf{x}\times\mathrm{div}\boldsymbol{\sigma}^T - \mathbf{x}\times\mathbf{b}(\mathbf{x},t)\right\}\,dv = \mathbf{0} \tag{2.40}$$

Since $\mathcal{B}_t$ is arbitrary,

$$x \times \rho(\mathbf{x},t)\,\ddot{\mathbf{x}} - \mathbf{x}\times\mathrm{div}\boldsymbol{\sigma}^T - \mathbf{x}\times\mathbf{b}(\mathbf{x},t) + \boldsymbol{\epsilon} : \boldsymbol{\sigma}^T = \mathbf{0} \tag{2.41}$$

Then, with Eq 2.31, we have:

$$\boldsymbol{\epsilon} : \boldsymbol{\sigma}^T = \mathbf{0} \tag{2.42}$$

showing the symmetric properties of the *Cauchy stress* tensor.

Setting up the Lagrangian form of the above equations,

$$\frac{d}{dt}\int_{\mathcal{B}} \mathbf{x}(\mathbf{X},t) \times \rho_0\dot{\mathbf{x}}(\mathbf{X},t)\,dV = \int_{\partial\mathcal{B}} \mathbf{x}(\mathbf{X},t) \times \mathbf{t}^{(\boldsymbol{n})}(\mathbf{X},t)\,dA + \int_{\mathcal{B}} \mathbf{x}(\mathbf{X},t) \times \mathbf{b}(\mathbf{X},t)\,dV. \tag{2.43}$$

Introducing the first Piola Kirchhoff stress and using the Gauss Divergence theorem,

$$\int_{\mathcal{B}} \left\{\mathbf{x}(\mathbf{X},t) \times \rho_0\ddot{\mathbf{x}}(\mathbf{X},t) - \mathrm{div}\left(\mathbf{x}(\mathbf{X},t) \times \mathbf{P}\right) - \mathbf{x}(\mathbf{X},t) \times \mathbf{b}(\mathbf{X},t)\right\} dV = \mathbf{0} \tag{2.44}$$

Taking the divergence of $(\mathbf{x}(\mathbf{X},t) \times \mathbf{P})$,

$$\int_{\mathcal{B}} \left\{\mathbf{x}(\mathbf{X},t) \times (\rho_0\ddot{\mathbf{x}}(\mathbf{X},t) - \mathrm{div}\mathbf{P} - \mathbf{b}(\mathbf{X},t)) - \mathrm{Grad}\,\mathbf{x}(\mathbf{X},t) \times \mathbf{P}\right\} dV = \mathbf{0} \tag{2.45}$$

with Eq 2.35

$$\int_{\mathcal{B}} \mathbf{F} \times \mathbf{P}\,dV = \mathbf{0}. \tag{2.46}$$

Since the integrand is arbitrary,

$$\mathbf{F} \times \mathbf{P} = \boldsymbol{\epsilon} : \left(\mathbf{F}\mathbf{P}^T\right) = \mathbf{0} \tag{2.47}$$

this time demonstrating the symmetric property of $(\mathbf{FP})^T$:

$$\mathbf{F}\mathbf{P}^T = \mathbf{P}\mathbf{F}^T. \tag{2.48}$$

As $\mathbf{S} = \mathbf{P}\mathbf{F}^T$, the second Piola-Kirchhoff stress is also symmetric.

Chapter 3

Moving Least Square Approximation

3.1 Introduction

The Moving Least Square Method (MLS) is a widely known approximation technique used in the Element Free Galerkin Method and other mesh independent approximation techniques. The resulting smooth shape functions and their continuous derivatives are computed from a set of point-wise scattered data. Thus, any function being approximated by MLS will represent only the near-best solution with:

$$u(\mathbf{x}) \neq u^h(\mathbf{x}). \tag{3.1}$$

In that regards, MLS cannot be described as interpolation technique, but rather as an approximation one.

3.2 MLS Approximants

In this section, the MLS approximants will be derived thoroughly in order to have a better understanding of their nature, advantages as well as disadvantages. For example, consider the case where the function $u(\mathbf{x})$ is approximated to $u^h(\mathbf{x})$ using $\mathbf{P}$, representing the polynomial and $\mathbf{a}(\mathbf{x})$, the unknowns (the number of unknowns corresponds to the order of the polynomial)

$$u^h(\mathbf{x}) = \mathbf{P}(\mathbf{x}) \cdot \mathbf{a}(\mathbf{x}). \tag{3.2}$$

For a typical Least Square (LS) problem, the aim is to minimise the difference between the approximated solution and the exact one,

$$\text{minimise } (J = \sum_I |u^h(\mathbf{x}_I) - u(\mathbf{x}_I)|^2). \tag{3.3}$$

The equation helps in finding an adequate set of u^h that are as close as possible to u and whereby the difference between them will be nearly zero.

In the current situation, the resulting shape functions are global, since all nodes of the domain will influence $u(\mathbf{x}_I)$. Unfortunately, such approximation schemes are known to produce very weak approximation characteristics, resulting in large errors and high demand in computational resources with long calculation processes. In order to solve these problems, a localised version of the Least Square method was proposed by Lancaster and Salkauskas in [9] by incorporating a weight function of compact support in the J function.

The weight function takes into account the Euclidean distance of the nodal coordinates with respect to the principal node, to determine by how the latter will be influenced by a neighbour node. In that respect, each point will only need a few supporting nodes that will be used to calculate the shape functions.

Modifying the LS functional from Eq 3.3, the MLS problem is now posed as

$$\min\{\sum_{I=1}^{N} w(\mathbf{x}-\mathbf{x}_I)[\mathbf{P}^T(\mathbf{x}_I)\mathbf{a}(\mathbf{x}) - u(\mathbf{x}_I)]^2\}. \tag{3.4}$$

Carrying out the minimisation results in an equation that can find $\mathbf{a}(\mathbf{x})$.

$$\mathbf{a}(\mathbf{x}) = [\sum_{I=1}^{N} w(\mathbf{x}-\mathbf{x}_I)\mathbf{P}(\mathbf{x}_I)\mathbf{P}^T(\mathbf{x}_I)]^{-1} \sum_{I=1}^{N} w(\mathbf{x}-\mathbf{x}_I)\mathbf{P}(\mathbf{x}_I)u(\mathbf{x}_I). \tag{3.5}$$

with $\sum_{I=1}^{N} w(\mathbf{x}-\mathbf{x}_I)\mathbf{P}(\mathbf{x}_I) \otimes \mathbf{P}(\mathbf{x}_I)$ known as the so-called *moment matrix*, $\mathbf{M}$. Hence, Eq 3.2 can be represented as

$$u^h(\mathbf{x}) = \mathbf{P}(\mathbf{x}) \cdot \mathbf{M}^{-1}(\mathbf{x}) \sum_{I=1}^{N} \mathbf{P}(\mathbf{x}_I) w(\mathbf{x}-\mathbf{x}_I)\ u(\mathbf{x}_I). \tag{3.6}$$

3.3 The weight function

As previously noted, the weight function incorporates some locality features into the LS approximation technique. It requires an influence radius which will define the local region where all interior nodes will be called the *supporting nodes*. Thus, in respect to the locality condition, the weight function should be defined in such a way that the supporting nodes will a have non-zero contribution compared to the exterior ones. Moreover, since the smoothness of the basis function is of primary importance, the weight functions are chosen in such a way that they are C^1 continuous, as shown by Lancaster and Salkauskas. The shape-profile that is most frequently used in describing the distribution of the the shape functions is shown in Fig 3.1.

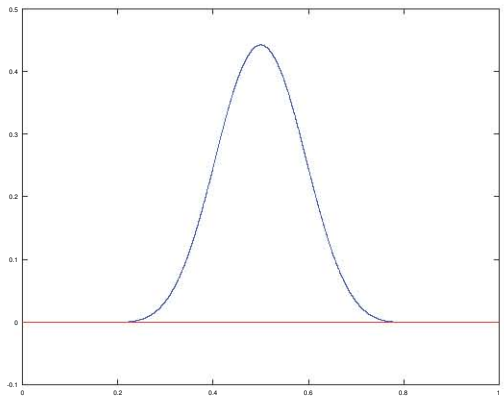

Figure 3.1: *Bell-shape profile of the weight function*

The latter aligns with our requirement that spacial distances will determine by how much the neighbouring nodes will affect the point $\mathbf{x}$. If one considers the profile in terms of equation, the curve can then be described as a cubic spline with:

$$w(\mathbf{x}-\mathbf{x}_I)\begin{cases}\frac{2}{3}-4r^2+4r^3 & \text{for } r\leq\frac{1}{2}\\ \frac{4}{3}-4r+4r^2-\frac{4}{3}r^3 & \text{for } \frac{1}{2}\leq r<1\\ 0 & \text{for } r>\frac{1}{2}\end{cases} \tag{3.7}$$

with $r=\frac{|(\mathbf{x}-\mathbf{x}_I)|}{D}$, D is the influence radius and $\mathbf{x}_I$ are the supporting nodes. The spacial derivatives of the shape functions are given as:

$$\frac{dw}{d\mathbf{x}}=\frac{dw}{dr}\frac{dr}{d\mathbf{x}}\begin{cases}(-8r+12r^2)sign(\mathbf{x}-\mathbf{x}_i) & \text{for } r\leq\frac{1}{2}\\ (-4+8r-12r^2)sign(\mathbf{x}-\mathbf{x}_i) & \text{for } \frac{1}{2}\leq r<1\\ 0 & \text{for } r>\frac{1}{2}.\end{cases} \tag{3.8}$$

A visual representation of the shape function distribution and its derivative are shown in Fig. 3.2

Two alternative spline that can be used instead of the cubic one is given below:

- The Quartic Spline, given by

$$w(r)\begin{cases}1-6r^2+8r^3-3r^4 & \text{for } |r|\leq 1\\ 0 & \text{for } |r|>1\end{cases} \tag{3.9}$$

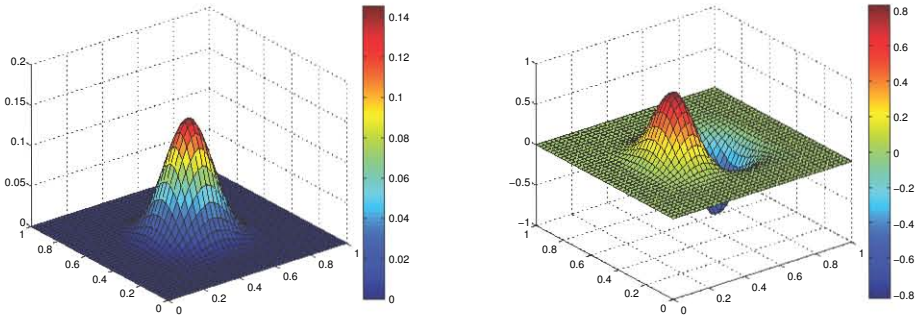

(a) (b)

Figure 3.2: *In 2D, the mid-node cubic spline plot of MLS : (a) Shape functions (b)first derivative of shape function*

- The Gaussian spline, expressed by

$$w(r)\begin{cases} e^{-(r/0.4)^2} & \text{for } |r| \leq 1 \\ 0 & \text{for } |r| > 1 \end{cases} \tag{3.10}$$

3.4 Advantages and Disadvantages

The following section gives the major advantages. The disadvantages are also included as the alternative method to MLS, elaborated in the next chapter, will not incorporate them.

3.4.1 Advantages

- The smoothness of the MLS basis is dependent on the weight function. Even if lower order polynomials are used, high order accuracy can be achieved if the order of the weight function is higher.
- The shape functions are quite easy to compute. There is no requirement to establish an iterative method for calculating the coefficients of the polynomial.
- Higher order polynomials can be easily incorporated.
- Computation of approximants are not mesh dependent. Only the nodal coordinate is required.
- The locality feature brought by the weight function reduces the computational resources and time of calculating shape functions, since only a few nodes are required as compared to the global node set needed for LS-based scheme. However, it should be noted that the FEM approximation scheme is still more local.

3.4.2 Disadvantages

- The continuity of MLS basis and the smoothness of the approximated solution can be affected by the negative shape function values that are usually encountered at boundary nodes, found close to the end of the influence zone, as shown in Fig 3.3.

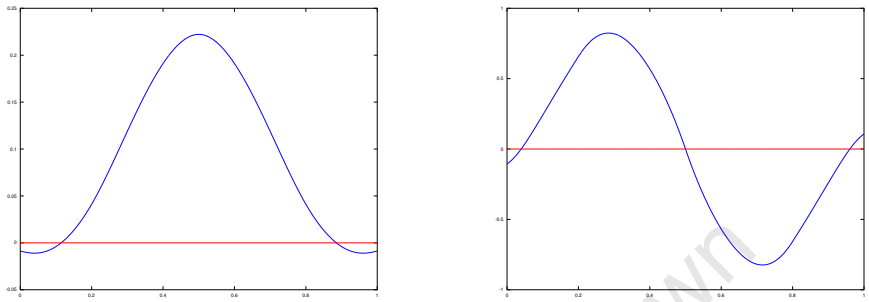

(a) (b)

Figure 3.3: *In 1D, the mid-node plot of MLS : (a) Shape functions (b)first derivative of shape function*

- Shape functions at the boundary nodes do not possess the Kronecker delta property (Fig 3.4) which indicates that imposition of the boundary conditions is not straight forward. Hence different techniques such as the Lagrange Multipliers, the modified variational principle or the penalty method needs to be employed.

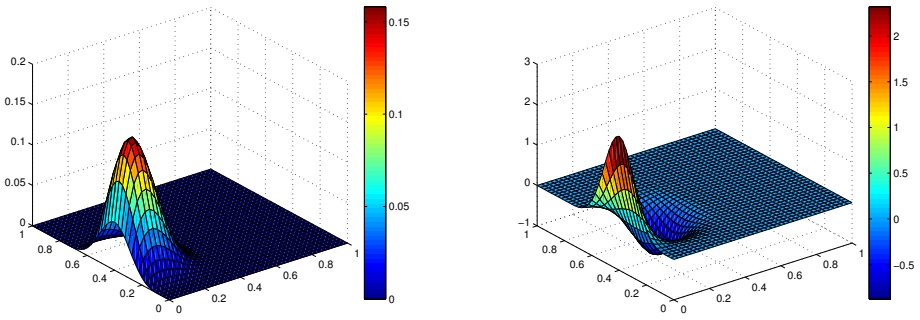

(a) (b)

Figure 3.4: *In 2D, the boundary-node plot of MLS : (a) Shape functions (b)first derivative of shape function*

3.5 Implementation of Mesh-Free method

In this section, the actual implementation of the mesh free method in Seska is given as an algorithm with some brief explanations of the processing taking place in a parallel computing

environment:

1. Seska loads in the input parameters and the mesh data of the geometry.
2. The Particles belonging to the mesh is sorted according to their identity numbers. This step is quite useful as latter on, it helps in building the stiffness matrix with the desired characteristic of having a banded and symmetric matrix. The identity is defined as is defined by,
$$d_J^I = I \cdot n + J \tag{3.11}$$
by assuming that Particle P_I has got n parameters d_J^I
3. The elements of the domain is splitted among the number of processes that Seska is being run with.
4. Each process computes the Gauss quadrature coordinates and weights as well as the particles weight of portion of elements attributed to it during the previous step.
5. The influence zone of the particles are set-up and neighbouring nodes are identified.
6. The Gauss quadrature points are distributed over the processes. The distribution is done in such a way that the communication between the processes will be limited.
7. The shape functions and their corresponding derivatives at the particles and integration points are calculated using MLS.
8. The shape functions and their derivatives are modified in order to allow the boundary collocation method to apply the essential boundary conditions.
9. The stiffness matrix, the internal and the external force vector are assembled. Using the modified shape functions, the stiffness matrix $\mathbf{K}$ is set-up. The natural boundary conditions is then expressed in terms of the force vector $\mathbf{f}_{ext}$ and $\mathbf{f}_{int}$. Then the discrete equation system is build up to form:
$$\mathbf{Kd} = \mathbf{f}_{ext} - \mathbf{f}_{int} = \mathbf{\Psi} \tag{3.12}$$
where
   - $\mathbf{d}$ is the displacement field increment $\Delta\mathbf{u}$
   - $\mathbf{f}_{ext} = \lambda\mathbf{f}_{ext,0}$
   - $\mathbf{f}_{ext,0}$ is the final external loading vector
   - λ is the current loading vector which takes values between 0 and 1.
   - $\mathbf{\Psi} = \mathbf{\Psi}(\mathbf{u}^i)$ is the residual vector.
10. The Discrete equation system is then solved and the displacement for all particles P_I can be updated:
$$u_I^{i+1} = \Delta u_I + u_I^i \tag{3.13}$$
with i being the iteration step.

Chapter 4

Local Maximum Entropy Approximation

In this chapter, the Local Maximum Entropy approximation will be introduced. The mathematical concept from which this method has been developed is first provided in section 4.1. Thereafter, the Local Maximum Entropy method, along with its derivation and properties, will be looked at in section 4.2.

4.1 Preliminary Mathematical Concepts

The main mathematical concepts that will be explained here are related to the Convex Approximation scheme which is itself considered as a Convex Optimisation problem. After looking at these theories, the Lagrange Multipliers and the saddle point concept will be applied in solving the convex problem. For more information, the reader is referred to the textbook: *Convex Optimization* by Boyd and Vandenberghe [17] .

4.1.1 Convex Approximation Schemes

"*A convex approximation scheme is one in which the objective and constraint functions are convex*" (Boyd and Vandenberghe [17]). It usually forms part of a mathematical optimisation problem which takes the form of:

$$\begin{aligned} &\text{minimise } f_0(\mathbf{x}) \\ &\text{subject to } f_i(\mathbf{x}) \leq b_i, i = 1, ..., n \end{aligned} \tag{4.1}$$

with the objective function $f_0 : \mathbb{R}^n \to \mathbb{R}$ and the constraints or inequality constraints $f_i : \mathbb{R}^n \to \mathbb{R}$ which provide a numerical limit b_i. Here, n, is the number of constraints. The goal is to define a spatial coordinate vector $\mathbf{x}$ or so-called *optimal solution*, which minimises the objective function while satisfying one or more constraints. However, before solving the above problems, some concepts, from which the convex approximation method has been derived, will

be explained.

4.1.2 Convex Optimisation Problems

The form of optimisation problems are similar to Eq 4.1 except that, in the case of a convex optimisation problem, the newly added constraints differ. The objective function, on the other hand, will be defined in the same way. The standard definition of the problem is as follows:

$$\text{minimise } f_0(\mathbf{x}) \tag{4.2}$$

$$\text{subject to } \begin{cases} f_i(\mathbf{x}) \leq 0, i = 1, ..., m \\ h_i(\mathbf{x}) = 0, i = 1, ..., p \end{cases} \tag{4.3}$$

whereby,

- $f_0 : \mathbb{R}^n \to \mathbb{R}$: Objective function
- $f_i(\mathbf{x}) \leq 0$: inequality constraints
- $h_i(\mathbf{x}) = 0$: equality constraints
- m and n : number of constraints

Note :

- If no constraints are specified, the problem is considered as an *unconstrained* one.
- Any set of points related to an objective function and its constraints are called a "*domain of optimisation*" problem.

Most of the time, the solution of a convex optimisation problem is determined and promoted as a so-called "*optimal point*" $\mathbf{x}^\star$, while a set of the optimal points will be regarded as an "*optimal set*". Achieving such results will establish the problem as a "*solvable*" convex optimisation problem. However, poorly defined or unbounded problems can sometimes result in an empty optimal set where no optimal points have been found, concluding the problem as unsolvable.

In the same context, some optimal points which are termed as "*global optimal points*" or "*local optimal points*", are referred to the locality of the convex set over which the value of $\mathbf{x}$ has been solved for.

4.1.3 Maximisation Problem

The following standard form is frequently used to define a maximisation problem:

$$\text{maximise } -f_0(\mathbf{x}) \tag{4.4}$$

$$\text{subject to } \begin{cases} f_i(\mathbf{x}) \leq 0, i = 1, ..., m \\ h_i(\mathbf{x}) = 0, i = 1, ..., p. \end{cases} \tag{4.5}$$

In this case, the only difference that can be noted, when compared to minimisation problems, is the maximisation of a negative objective function.

4.1.3.1 Solving a maximisation problem

Since Maximum Entropy is known as a maximisation problem, the Lagrange multipliers are needed in solving these problems.

4.1.3.1.1 The Lagrangian

Consider an optimisation problem similar to 4.4. In order to solve such a maximisation problem, one needs to enforce the constraints to obtain the required set of solutions that respect all the stated conditions. The correct way of doing so is by using the Lagrange multipliers. The constraints are now multiplied by a weighted value and then added to the objective function. The complete equation is called the "*Lagrangian*", which takes the form of :

$$L(\mathbf{x}, \boldsymbol{\lambda}, \boldsymbol{\nu}) = f_0(\mathbf{x}) + \sum_{i=1}^{m} \lambda_i f_i(\mathbf{x}) + \sum_{i=1}^{p} \nu_i h_i(\mathbf{x}) \tag{4.6}$$

where λ_i and ν_i are the weighted contribution of the inequality constraints of the i^{th} term. However, for a group of points, the Lagrange multipliers will be represented by a vector of $\boldsymbol{\lambda}$ and $\boldsymbol{\nu}$ which is normally stated as the "*dual variables*" or "*Lagrange Multipliers' vector*".

4.1.3.1.2 The Lagrange Primal Problem

With the Lagrangian now available, the aim is to minimise Eq 4.6 with respect to $\mathbf{x}$. The resulting equation obtained is called the *Lagrange Dual function* and given by the function $g(\boldsymbol{\lambda}, \boldsymbol{\nu})$ in Eq 4.7.

$$g(\boldsymbol{\lambda}, \boldsymbol{\nu}) = \min\, L(\mathbf{x}, \boldsymbol{\lambda}, \boldsymbol{\nu}). \tag{4.7}$$

The optimal point, $\mathbf{x}^\star$, which can minimise the primal problem, yields a *primal solution* $p^\star$ when $f_0(\mathbf{x}^\star)$ is calculated.

4.1.3.1.3 The Lagrange Dual Problem

Minimising Eq 4.7 does not provide the solution of an optimisation directly since the Lagrangian is also a function of $\boldsymbol{\lambda}$ and $\boldsymbol{\nu}$. Hence, the values of the Lagrange multipliers need to be found. Therefore, this gives rise to a second optimisation problem (known as the *Lagrange dual problem*) which needs to be solved in the following form:

$$\text{maximise } g(\boldsymbol{\lambda}, \boldsymbol{\nu}) \tag{4.8}$$

$$\text{subject to } \boldsymbol{\lambda} \geq 0 \tag{4.9}$$

In this case, the imposed constraint specifies that the Lagrange multiplier be non-negative. If $\boldsymbol{\lambda}^\star$ and $\boldsymbol{\nu}^\star$ (referred to as *Dual Optimal* or *Optimal Lagrange Multipliers*) is the pair which satisfies the above problem, then the resulting optimal solution of the dual problem is denoted as $d^\star$.

4.1.3.1.4 Explicit Expression of the dual function

Usually, the Lagrange dual problems are not presented as shown above but rather it is expressed in an explicit way. That is, the constraints are not "hidden" inside the $g(\boldsymbol{\lambda}, \boldsymbol{\nu})$ function. To better understand the somewhat aesthetic and very useful transformation, consider the following problem:

$$\text{minimise } \mathbf{c^T x} \tag{4.10}$$

$$\text{subjected to } \mathbf{Ax} = \mathbf{b} \tag{4.11}$$

$$\mathbf{x} \geq 0 \tag{4.12}$$

which has an inequality constraint function $f_i(\mathbf{x}) = -\mathbf{x}_i, i = 1, ..., n$. The resulting Lagrangian,

$$L(\mathbf{x}, \boldsymbol{\lambda}, \boldsymbol{\nu}) = \mathbf{c^T x} - \boldsymbol{\lambda}^T \mathbf{x} + \boldsymbol{\nu}^T(\mathbf{Ax} - \mathbf{b}) \tag{4.13}$$

$$= -\mathbf{b}^T\boldsymbol{\nu} + (\mathbf{c} + \mathbf{A}^T\boldsymbol{\nu} - \boldsymbol{\lambda})^T\mathbf{x} \tag{4.14}$$

where the Dual function is given by,

$$g(\boldsymbol{\lambda}, \boldsymbol{\nu}) = \inf L(\mathbf{x}, \boldsymbol{\lambda}, \boldsymbol{\nu}) = -\mathbf{b}^T\boldsymbol{\nu} + \inf(\mathbf{c} + \mathbf{A}^T\boldsymbol{\nu} - \boldsymbol{\lambda})^T\mathbf{x} \tag{4.15}$$

So, instead of Eq 4.15,

$$\text{minimise } g(\boldsymbol{\lambda}, \boldsymbol{\nu}) \tag{4.16}$$

$$\text{subjected to } \boldsymbol{\lambda} \geq 0 \tag{4.17}$$

we now have an explicitly stated problem,

$$\text{minimise } -\mathbf{b}^T\boldsymbol{\nu} \tag{4.18}$$

$$\text{subjected to } \mathbf{c} + \mathbf{A}^T\boldsymbol{\nu} - \boldsymbol{\lambda} = 0 \tag{4.19}$$

$$\boldsymbol{\lambda} \geq 0. \tag{4.20}$$

4.1.3.2 Weak and Strong Duality

Analysing the optimal solution, $p^\star$ and the Lagrangian Dual Problem solution, $d^\star$, with respect to each other can be very useful. In that sense, the following sections will consider two possibilities that may arise, that is, either one is smaller compared to the other or they are equal.

4.1.3.2.1 Weak Duality

$$d^\star \leq p^\star. \tag{4.21}$$

This situation mostly arises when $d^\star$ and $p^\star$ are infinite. That is,

- a bottom unbounded primal problem having $p^\star = -\infty$ will also need that $d^\star = -\infty$. Hence, the Lagrange Dual problem is infeasible.

- a top unbounded primal problem with $p^\star = +\infty$ will have $d^\star = +\infty$ resulting in the primal problem being infeasible too.

However, Boyd and Vandenberghe [17] states that one should not disregard the values of $d^\star$ and $p^\star$ as infinite since some crucial information can still be extracted. For example, if one finds the difference between $d^\star$ and $p^\star$ (which is known as the *Optimal Duality gap* and is always non-negative), the value obtained can help in locating the lower bound of a complex and difficult to solve for problem.

4.1.3.2.2 Strong Duality

A strong duality condition holds when

$$d^\star = p^\star. \tag{4.22}$$

This means that the optimum bound between d^* and p^* is extremely close or has a zero optimal duality gap. Normally, a strong duality case does not hold unless the primal problem is convex or, in some cases, the established conditions, that do not have convexity properties, may influence the objective function. In the latter scenario, these conditions are labelled "*constraint qualifications*.

One of the qualifications that we will elaborate on and which will be quite useful later on, specially when deriving the Maximum Entropy shape function equations is the "*Slater's condition*". Consider a problem such as the one shown below:

$$\text{minimise } f_0(\mathbf{x}) \tag{4.23}$$

$$\text{subject to } \begin{cases} f_i(\mathbf{x}) \leq 0, i = 1, ..., m \\ \mathbf{A}\mathbf{x} = \mathbf{b}. \end{cases} \tag{4.24}$$

Slater's condition states that strong duality prevails, if $\mathbf{x} \in \mathbf{relintC}$ (where $\mathbf{relintC}$ is the relative interior of set $\mathbf{C}$ and set $\mathbf{C}$ consists of points which are not on the edge of the set) while $f_i(x)$ is convex. If obeyed, this statement can be of much help in obtaining the dual optimal solution with $\boldsymbol{\lambda}^\star$ and $\boldsymbol{\nu}^\star$.

4.1.3.3 Saddle Point Problem

Up to now, the primal and dual problem set have only been derived from the Lagrangian. From there, the two problems are combined into one where it is required :

- Firstly, minimise the maximisation of $L(\mathbf{x}, \boldsymbol{\lambda})$ over $\mathbf{x}$ while making sure that $\boldsymbol{\lambda} \leq 0$
- and secondly, maximise the minimisation of $L(\mathbf{x}, \boldsymbol{\lambda})$ over $\boldsymbol{\lambda}$ with $\mathbf{x} \in \mathbf{X}$.

Our problem has only doubled since the application of the Lagrange multipliers, instead of really gearing towards solving for $\mathbf{x}$.

Now, the final step that will bring in ultimate solution will be taken. To begin with, the *min-max characterisation*, a method which helps in finding a balance between the minimum

and maximum bound, is going to be made use of:

The primal and dual problem is first expressed in a symmetric form

$$\sup\ L(\mathbf{x}, \boldsymbol{\lambda}) = \sup(f_0(\mathbf{x}) + \boldsymbol{\lambda}^T \mathbf{x}). \tag{4.25}$$

To generate an optimal solution, two conditions need to be satisfied,

- $f_i \leq 0$
- $\boldsymbol{\lambda} = 0$ and $\sup\ L(\mathbf{x}, \boldsymbol{\lambda}) = f_0(\mathbf{x})$

which result in the optimal value of the primal problem being

$$p^\star = \inf \sup\ L(\mathbf{x}^\star, \boldsymbol{\lambda}^\star) \tag{4.26}$$

while the solution for the dual function is:

$$d^\star = \sup \inf\ L(\mathbf{x}^\star, \boldsymbol{\lambda}^\star) \tag{4.27}$$

Both $p^\star$ and $d^\star$ can be related through the following inequalities which can be used to explain their duality properties:

1. Weak duality:

$$p^\star \leq d^\star \tag{4.28}$$
$$\inf \sup\ L(\mathbf{x}^\star, \boldsymbol{\lambda}^\star) \leq \sup \inf\ L(\mathbf{x}^\star, \boldsymbol{\lambda}^\star). \tag{4.29}$$

2. Strong duality:

$$p^\star = d^\star \tag{4.30}$$
$$\inf \sup\ L(\mathbf{x}^\star, \boldsymbol{\lambda}^\star) = \sup \inf\ L(\mathbf{x}^\star, \boldsymbol{\lambda}^\star). \tag{4.31}$$

The saddle point is the most sought after solution in solving the Lagrangian. It is defined by a point which sits between the maximums of a saddle-like curve, representing the best compromise of the upper (sup) and lower (inf) bound. Hence the saddle point is that point which can describe the inequality equation, Eq 4.32.

$$L(\mathbf{x}, \boldsymbol{\lambda}^\star) \geq L(\mathbf{x}^\star, \boldsymbol{\lambda}^\star) \geq L(\mathbf{x}^\star, \boldsymbol{\lambda}). \tag{4.32}$$

4.2 Local Maximum Entropy

In the following sections, the setup of the Local Maximum Entropy approximation is given and their properties are examined and compared to MLS. Here, solving a convex optimisation problem results in a set of shape functions, p_a.

4.2.1 Introduction

The Local Maximum Entropy(LME) forms part of an approximation scheme, based on the work of Arroyo and Ortiz [1], that can be used to produce shape functions needed in solving discretised PDEs. In doing so, a balance is needed between the Delaunay triangulation and the maximum entropy statistical interference scheme where the balance point will yield the basis functions.

Since LME depends on a set of nodes that forms a convex domain, they are termed as "*convex approximation scheme*". As the latter produces shape functions with many essential aspects such as positivity, weak Kronecker delta properties and exact interpolations of affine functions, LME naturally inherits these characteristics.

4.2.2 Global Maximum Entropy

Entropy is commonly defined as a measure of uncertainty for a representative set of events. For example, consider two sets of events with their corresponding probabilities,

$$\underset{\textbf{\textit{Option 1}}}{\begin{bmatrix} A_1 \\ A_2 \end{bmatrix}} = \begin{bmatrix} 0.5 \\ 0.5 \end{bmatrix} \tag{4.33}$$

$$\underset{\textbf{\textit{Option 2}}}{\begin{bmatrix} A_1 \\ A_2 \end{bmatrix}} = \begin{bmatrix} 0.99 \\ 0.01 \end{bmatrix} \tag{4.34}$$

It can be said that ***Option 1*** has a larger entropy than ***Option 2***, since it is uncertain which event is most likely to occur as both carry the same probability. Thus, in this case we will define the set of events, in ***Option 1*** to have a maximum entropy. But in ***Option 2***, one of the events has a higher probability, which means that it is more likely to occur. In that case, this set will produce a lower entropy value.

From the above problem, only two sets of two events are presented with, making it fairly simple to deduce the uncertainty outcome in a non-quantitative way. However, for large sets of multiple events, such a decision making process can be very complex. In that case, Elwood Shannon's information entropy concept [18] is used for measuring and adequately quantifying uncertainty. The equation that the author proposed is:

$$H(\mathbf{A}) = -\sum_{a=1}^{n} p_a \log p_a \tag{4.35}$$

with p_a representing the probability that event $\mathbf{A}$, of set n events, will occur. The solution obtained from such an equation has some advantageous properties which are inherited by an approximation scheme based on this concept. These properties are:

- non-negative
- symmetric
- continuous
- strictly concave

With regards to the limits of $H(\mathbf{A})$,

$H(\mathbf{A}) = 0$: This means that the uncertainty is zero. Such a case only occurs if among the set of events, one of them is certain to occur ($p_a = 1$)

$H(\mathbf{A}) = -\log n$: This represents the most uncertain condition, i.e, the probabilities of all event is $1/n$. Thus adding more events will only add uncertainty.

Having introduced the concept of entropy and information entropy, the latter is used with a convex approximation scheme in order to pass on its properties in the final approximation scheme. Before beginning with the formulation process, the work of Edwin Thompson Jaynes [14] will be briefly reviewed. In his paper, Jaynes bridges the gap between statistical mechanics and information theory by arguing that both concepts mean the same thing and that the former is just a particular instance of the latter.

To have a better understanding of the above, let us apply Jaynes' concept. Identifying the zeroth (Eq 4.39) and first (Eq 4.40) order consistency condition as additional information, they will now be used to constrain a discrete probability distribution $\mathbf{p}(\mathbf{x})$. The solution to this problem can take the shape of multiple probability distributions around the domain. Thus, approximating a function from multiple nodal data u_a is considered a problem of statistical interference only:

$$u^h(\mathbf{x}) = \sum_{a=1}^{n} p_a(\mathbf{x}_a) u_a \tag{4.36}$$

with n being the number of supporting nodes and a, one particular node included from the set of supporting nodes. At this point, Jaynes' approach comes into play by stating the principle of maximum entropy. The author defines the least biased probability distribution as one which is built from all known constraints, assuming no other constraints have been left behind, while maximising the entropy objective function. Hence, the whole problem can be defined as shown

below:

$$\text{maximise} \quad H(\mathbf{p}) = -\sum_{a=1}^{n} p_a \log p_a \tag{4.37}$$

$$\text{subject to} \quad p_a \geq 0, a = 1, ..., N \tag{4.38}$$

$$\sum_{a=1}^{N} p_a = 1 \tag{4.39}$$

$$\sum_{a=1}^{N} p_a \mathbf{x}_a = \mathbf{x}. \tag{4.40}$$

The only unknown which needs to be solved for is p_a, as $\mathbf{x}_a$ represents only a vector of nodal coordinates. In this case, solving p_a will yield shape functions based on the least biased approximation scheme (MaxEnt). Unfortunately, if one makes use of them to approximate a function, significant error is likely to arise. This is because they are derived from a highly non-local support, extending over the whole domain, thus developing a non-interpolating property. At the boundary, MaxEnt shape functions still behave nicely by vanishing completely beyond. However, none of the interior nodes even exhibit unity characteristics (that is having a shape function value of approximately equal to one at their corresponding node). In that case, the "global effect" is encountered which results in interpolants that are therefore called the "*global maximum entropy interpolants*".

The only way of tackling this problem is by making the calculation of the shape function local for each node with the help of a compact support, that is only a portion of the the surrounding or neighbouring nodes will influence the build-up of MaxEnt shape functions functions. If this is successfully achieved, a better interpolating characteristic is expected.

4.2.3 Local Maximum Entropy

In their paper [1], Arroyo and Ortiz proposed an interesting way of forcing the computation of interpolants to take locality into consideration. The authors firstly defined a prior which is a width correlating function as:

$$w[\mathbf{p}_a] = \int_{\Omega} p_a(\mathbf{x}) |\mathbf{x} - \mathbf{x}_a|^2 d\mathbf{x} \tag{4.41}$$

which additionally enabled them to control:

- the width of the shape function
- the decay of the shape functions with distance when moving from the corresponding node.

This is successfully achieved with the help of $|\mathbf{x} - \mathbf{x}_a|^2$ which imposes a weighted value to the basis. The magnitude of the value decreases the further it is from the actual interpolating node (in a similar manner to the MLS weight function). From this, using the above equation, Arroyo and Ortiz built up a new approximation scheme which is termed the "*Local approximation*

scheme" as follows:

$$w[\mathbf{p}_a] = \int_\Omega \sum_{a=1}^{N} p_a(\mathbf{x})|\mathbf{x} - \mathbf{x}_a|^2 d\mathbf{x} \tag{4.42}$$

while being subjected to the same constraints as the global maximum entropy approximation scheme. Here also, the main goal is to minimise the above function in order to solve for p_a. If Eq 4.42 is recast, the local approximation scheme can then be re-defined as follows:

$$\text{For fixed } \mathbf{x} \text{ maximise } U(\mathbf{x}, \mathbf{p}) \equiv \sum_{a=1}^{n} p_a|\mathbf{x} - \mathbf{x}_a|^2 \tag{4.43}$$

$$\text{subject to } \; p_a \geq 0, a = 1, ..., N \tag{4.44}$$

$$\sum_{a=1}^{N} p_a = 1 \tag{4.45}$$

$$\sum_{a=1}^{N} p_a \mathbf{x}_a = \mathbf{x}. \tag{4.46}$$

From the above, the authors observed the followings:

- Absence of derivatives in the objective function, resulting in point-wise minimisation.
- If they take Rajan's work [19] into consideration, it can be proved that for nodes having a general position, the above program yields a unique solution equivalent to the piecewise affine shape function of the Delaunay triangulation. But in the case of a degenerated node set, Delaunay triangulation (also known as the Delaunay approximation scheme) solutions and the above linear program solutions are both no longer unique.

Having now defined the locality scheme, the latter is now incorporated with the least biased approximation scheme, resulting in the Local Maximum Entropy convex approximation scheme.

$$\text{For fixed } \mathbf{x} \text{ maximise } \; f_\beta(\mathbf{x}, \mathbf{p}) \equiv \beta U(\mathbf{x}, \mathbf{p}) - H(\mathbf{p}) \tag{4.47}$$

$$\text{subject to } \; p_a \geq 0, a = 1, ..., N \tag{4.48}$$

$$\sum_{a=1}^{N} p_a = 1 \tag{4.49}$$

$$\sum_{a=1}^{N} p_a \mathbf{x}_a = \mathbf{x}. \tag{4.50}$$

The role of beta is required in determining by how much the locality approximants will affect the least biased approximation scheme. If β is zero, the global MaxEnt shape functions are recovered but when it shifts to $+\infty$, the Delaunay approximation scheme is fully retrieved.
The objective of the new scheme is to find an optimum balance between maximum locality and maximum entropy, that is an equilibrium between both, the least biased approximation scheme and Delaunay approximation scheme. In that case, Arroyo and Ortiz proposed calling the solution the "*pareto of optima solution*". The set of such solutions will therefore be called the *Pareto set*.

4.2.4 Priors

"Priors ", represented by $m(\mathbf{x})$, is the name given to those functions that have the capability of producing the global MaxEnt approximation scheme with some locality properties. In the work of Arroyo and Ortiz [1], only Gaussian priors have been used to develop the local MaxEnt shape function. However, other type of priors can still be used. In this section, a list of possible prior functions that could potentially have been applied alternatively will be introduced:

Uniform prior

$$m(\mathbf{x}) = 1/n. \tag{4.51}$$

This kind of prior gives the "flattest" possible distribution that represents the imposed constraints. In this case, Sukumar and Wright [11] reported that the shape function of LME is almost the same as those from the bilinear finite elements basis function of a square while still being smooth and well bounded. In Fig 4.1 , the LME basis is quite non local, since it can be seen to take over the whole domain. In this case the global maximum entropy program is recovered completely. Such shape functions are very small in magnitude and have poor approximating qualities.

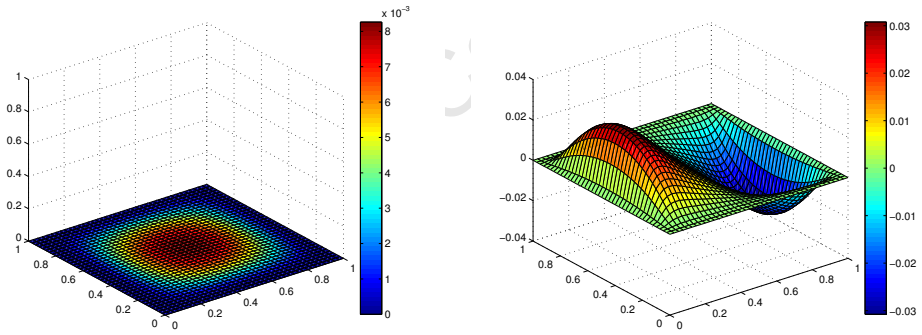

(a) (b)

Figure 4.1: *In 2D, the constant prior-based LME : (a) Shape function (b)first derivative of shape function*

Non-Uniform prior

In non-uniform priors, a bell-shape-like basis function is obtained over $\mathbf{x}$, with the latter always having the highest value. For this reason, they usually have better interpolating capabilities than uniform ones and therefore minimise the overall error. Among these priors, the followings are the ones that have already been implemented in other approximation techniques and are well known:

- The cubic spline (illustrated in Fig 4.2) , which we have already seen in MLS.
- Radial Basis Gaussian (RGB)
  The RGB basis function is the one that is actually been chosen for LME in general.

$$m(x) = \varphi||\mathbf{x} - \mathbf{x}_i|^2 \tag{4.52}$$

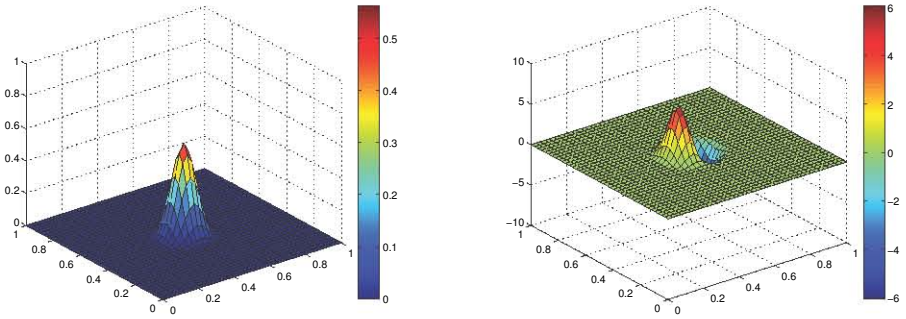

(a) (b)

Figure 4.2: *In 2D, the Cubic spline prior-based LME: (a) Shape function (b) first derivative of shape functions*

The plots of its shape functions and its derivative are shown in Fig 4.3

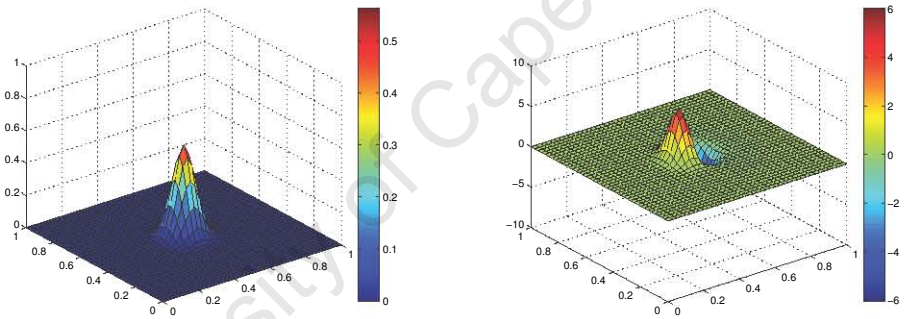

(a) (b)

Figure 4.3: *In 2D, the Gaussian prior-based LME : (a) Shape function (b)first derivative of shape function*

- R functions or implicit functions that are defined on a graph [11]
- Quadratic Spline (shown in Fig 4.4), has also been presented in MLS chapter and is given by Eq 3.7.

A 1D plot, shown in Fig 4.5, can provide a visual difference between the priors that have been considered so far. The Gaussian prior is seen to assign a higher shape function value to the main particle while those from the constant prior are much lower than the others and span over the whole domain. Also note the absence of negative shape functions.

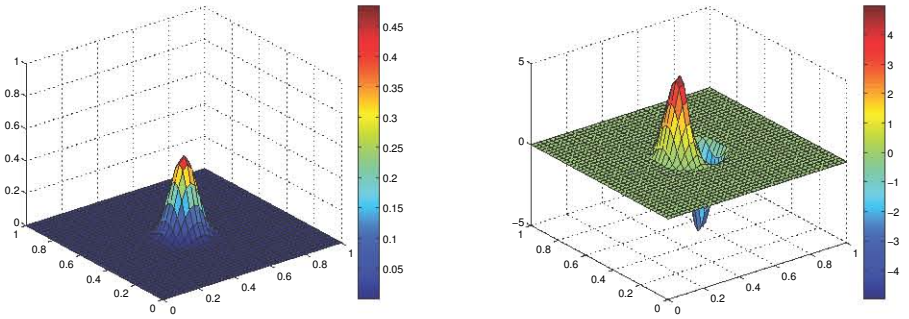

(a) (b)

Figure 4.4: *In 2D, the Quadratic spline prior-based LME : (a) Shape function (b)firstderivative of shape function*

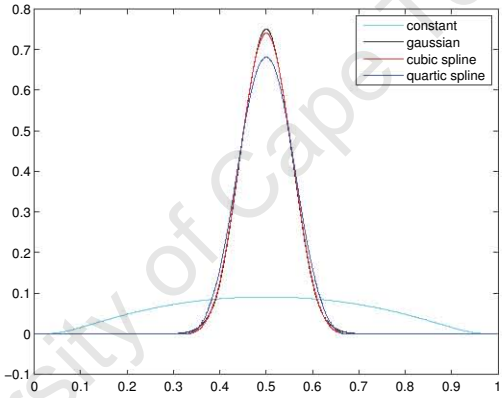

Figure 4.5: *Combined plots of shape functions calculated from different priors*

From all the above priors, some of which have been analysed by Arroyo and Ortiz [1] and others by Sukumar and Wets [20], it has been found that the Gaussian prior is the most suitable one. It provides a flexible compact support, continuity and also Gaussian decay properties which allows only a small number of nodes to participate in the calculation of the shape functions, thus reducing computational resources.

4.2.5 Calculation of Shape functions

In this section, the LME approximation scheme will be manipulated to produce the required shape functions ı. As shown in section 4.1.3.1, the Lagrange multipliers will be used to enforce the constraints from Eq 4.47 and thus producing the Lagrangian:

$$L(\mathbf{p}, \lambda_0, \boldsymbol{\lambda}) = f_\beta(\mathbf{p}) + \lambda_0(\mathbf{1} \cdot \mathbf{p} - 1) + \boldsymbol{\lambda} \cdot \mathbf{Y}\mathbf{p} \tag{4.53}$$

where

- λ_0 and $\boldsymbol{\lambda}$ are the Lagrange multipliers.
- $\mathbf{1}$ is a vector of ones
- $\mathbf{Yp} = \sum_a p_a(\mathbf{x}_a - \mathbf{x})$
- $\mathbf{Y} = N \times d$ matrix representing the shifted nodal coordinates $(\mathbf{x}_a - \mathbf{x})$
- The Lagrangian acts on a $\mathbb{R}^N_+ \times \mathbb{R} \times \mathbb{R}^d$ domain.

From there, λ_0^* and $\boldsymbol{\lambda}^*$ are defined to be the saddle point in order to find the values of the Lagrange Multipliers. Taking the variation of Lagrangian with respect to p_{β_a}, which is the shape function of a coordinate $\mathbf{x}$ for a specific value of β.

$$\frac{\partial\, L(\mathbf{p}, \lambda_0, \boldsymbol{\lambda})}{\partial p_{\beta_a}} \quad = \quad \beta|\mathbf{x} \; - \; \mathbf{x}_a|^2 \; + \; \sum_{a=1}^{N} \log p_{\beta_a} \; + \; 1 \; + \; \lambda_0^\star \; + \; \boldsymbol{\lambda}^\star \; \cdot \; \mathbf{Y}\mathbf{p}_{\beta_a} \quad = \quad 0. \tag{4.54}$$

Making p_{β_a} subject of formula will result in Eq 4.55 which helps us to find the shape functions:

$$p_{\beta_a} = \frac{e^{-\beta|\mathbf{x}-\mathbf{x}_a|^2 + \lambda^\star.(\mathbf{x}-\mathbf{x}_a)}}{e^{1+\lambda_0^\star}}. \tag{4.55}$$

However the saddle point solution is still required to be found. Using the same procedure as in section 4.1.3.1, the Lagrange dual function is found

$$g(\lambda_0, \boldsymbol{\lambda}) = -\lambda_0 - inf\, \{-f_\beta - \lambda_0 \mathbf{p}_{\beta_a} - \boldsymbol{\lambda}.(\mathbf{x}_a - \mathbf{x})\mathbf{p}_{\beta_a}\}. \tag{4.56}$$

Eq 4.56 can be simplified by using the conjugate properties of the LME objective function to remove the *inf* statement. The resulting equation can therefore help in finding a solution for $\lambda_0^\star$.

$$\lambda_0^\star = \arg\max \{-\lambda_0 - e^{-\lambda_0 1 - 1} \sum_{a=1}^{N} e^{-\beta|\mathbf{x}-\mathbf{x}_a|^2 + \boldsymbol{\lambda}.(\mathbf{x}-\mathbf{x}_a)}\}. \tag{4.57}$$

Taking the derivative with respect to λ_0 is used to determine the partition function

$$\frac{\partial}{\partial \lambda_0}\{-\lambda_0 - e^{-\lambda_0 1 - 1} \sum_{n=1}^{N} e^{-\beta|\mathbf{x}-\mathbf{x}_a|^2 + \boldsymbol{\lambda}.(\mathbf{x}-\mathbf{x}_a)}\} = 0 \tag{4.58}$$

$$-1 + e^{-\lambda_0 - 1} \sum_{a=1}^{N} e^{-\beta|\mathbf{x}-\mathbf{x}_a|^2 + \boldsymbol{\lambda}.(\mathbf{x}-\mathbf{x}_a)} = 0 \tag{4.59}$$

$$\sum_{a=1}^{N} e^{-\beta|\mathbf{x}-\mathbf{x}_a|^2 + \boldsymbol{\lambda}\cdot(\mathbf{x}-\mathbf{x}_a)} = \frac{1}{e^{-\lambda_0 - 1}} = e^{\lambda_0 + 1} = Z(\mathbf{x}, \boldsymbol{\lambda}). \tag{4.60}$$

With $\lambda_0^\star = \log Z(\mathbf{x}, \boldsymbol{\lambda}) - 1$, we can now reduce the dual problem into a single unknown, i.e $\boldsymbol{\lambda}$,

$$g(\boldsymbol{\lambda}) = -\{\log Z(\mathbf{x}, \lambda) - 1\} - e^{-\log Z + 1 - 1} Z \tag{4.61}$$

$$= -\log Z(\mathbf{x}, \lambda). \tag{4.62}$$

$$\tag{4.63}$$

Therefore, the solution of $\mathbf{x}$ is,

$$\boldsymbol{\lambda}^\star(\mathbf{x}) = \arg\min \ \log Z(\mathbf{x}, \boldsymbol{\lambda}). \tag{4.64}$$

Finally, to calculate the shape functions, let

$$Z(\mathbf{x}, \boldsymbol{\lambda}^\star(\mathbf{x})) = \sum_{a=1}^{N} e^{\beta|\mathbf{x}-\mathbf{x}_a|^2 + \boldsymbol{\lambda}^\star(\mathbf{x})(\mathbf{x}-\mathbf{x}_a)^2} \tag{4.65}$$

so that p_{β_a} can now be transformed into:

$$p_{\beta_a} = \frac{1}{Z(\mathbf{x}, \boldsymbol{\lambda}^\star(\mathbf{x}))} e^{\beta|\mathbf{x}-\mathbf{x}_a|^2 + \boldsymbol{\lambda}^\star(\mathbf{x})(\mathbf{x}-\mathbf{x}_a)^2}. \tag{4.66}$$

Note, as observed, in Eq 4.64, $\boldsymbol{\lambda}^\star$ is a non-linear equation. In order to solve it, an iterative algorithm need to be employed. In this situation, the authors have used the Newton iteration algorithm with an initial guess of $\lambda = 0$. The steps for each iteration k are calculated as follows

$$\boldsymbol{\lambda}^{k+1} = \boldsymbol{\lambda}^k + \triangle\boldsymbol{\lambda} \tag{4.67}$$

where the step size is calculated as $\triangle\boldsymbol{\lambda} = -\frac{\mathbf{R}}{\mathbf{J}}$ where

$$\mathbf{R} = \partial_{\boldsymbol{\lambda}} \log Z(\mathbf{x}, \boldsymbol{\lambda}) = \sum_{a=1}^{N} p_a(\mathbf{x}, \boldsymbol{\lambda})(\mathbf{x} - \mathbf{x}_a) \tag{4.68}$$

$$\mathbf{J} = \partial_{\boldsymbol{\lambda}}\partial_{\boldsymbol{\lambda}} \log Z(\mathbf{x}, \boldsymbol{\lambda}) = \sum_{a=1}^{N} p_a(\mathbf{x}, \boldsymbol{\lambda})(\mathbf{x} - \mathbf{x}_a) \otimes (\mathbf{x} - \mathbf{x}_a) - \partial_{\boldsymbol{\lambda}} \log Z(\mathbf{x}, \boldsymbol{\lambda}) \otimes \partial_{\boldsymbol{\lambda}} \log Z(\mathbf{x}, \boldsymbol{\lambda}).$$

$$\tag{4.69}$$

4.2.6 Derivative of the Shape function

The smoothness of the LME shape functions can be investigated by looking at its corresponding derivatives. The final expression for computing the derivative of the shape function is given as (Derivation can be found in [1]):

$$\nabla p_a^\star = -p_a^\star (\mathbf{J}^\star)^{-1}(\mathbf{x} - \mathbf{x}_a) + p_a^\star K_a \nabla\beta \tag{4.70}$$

where,

$$K_a = [\sum_b p_b^\star |\mathbf{x} - \mathbf{x}_b|^2 (\mathbf{x} - \mathbf{x}_b)].(\mathbf{J}^\star)^{-1}(\mathbf{x} - \mathbf{x}_a) - |\mathbf{x} - \mathbf{x}_a|^2 + U(\mathbf{x}, p^\star). \tag{4.71}$$

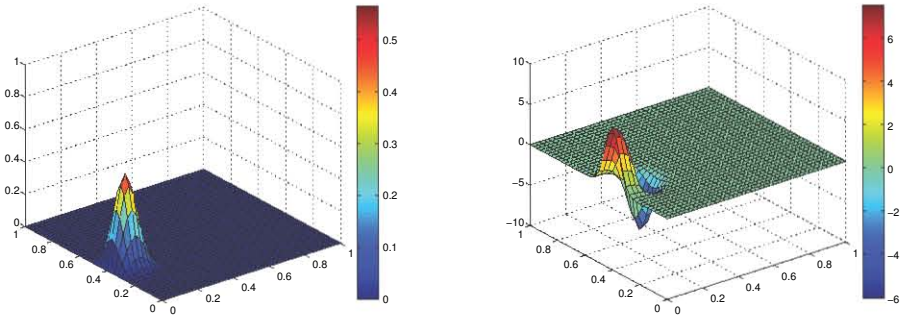

(a) (b)

Figure 4.6: *In 2D, the near-boundary node plot of LME : (a) Shape function and (b) first derivative of shape function in the x-direction*

The first derivative of the shape function is not certain to be smooth since they are by default computed at each point (i.e point-wise). However, in their paper [1], Arroyo and Ortiz showed that the smoothness will mainly depend on the $\boldsymbol{\lambda}(\mathbf{x})$ as its derivative is highly involved in formulating Eq 4.70. One final remark related to β can be made. If the latter is zero, then the calculation of the derivative is greatly simplified as K_a is no longer required.

4.2.7 Characteristics of LME shape functions

The resulting Local Maximum Entropy Method has been found to have the following properties:

- Positive shape functions
- The Shape functions of the interior nodes vanish completely at the boundary (refer to Fig. 4.6).
- Weak Kronecker delta property at the boundary.
- Easily extensible to higher spatial dimension.
- Interpolate affine function exactly.
- Different decay gradient can be obtained.

4.2.8 The unstructured mesh dilemma

In the formulation of the shape function, the only parameter that has not been defined properly is β. According to Arroyo and Ortiz [1], the latter can be defined as

$$\beta = \frac{\gamma}{h^2} \tag{4.72}$$

where

γ : defines the degree of locality of maximum entropy interpolants

h : characteristic nodal spacing

4.2.8.1 Gamma

For a structured mesh, where h is constant, only γ is found to be responsible for assigning locality characteristics to the shape function. Hence, if one varies γ to its extremes, then the interpolants will either gradually inherit global properties as γ tends to zero or recover the Delaunay basis properties as γ goes towards infinity. For values in-between these limits, the followings have been observed:

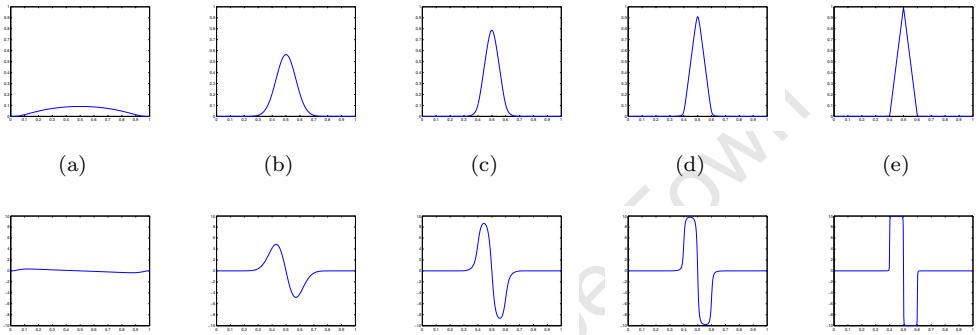

Figure 4.7: *In 1D, the transition of gamma from 0 to 6 : (a)-(e) Shape functions and (f)-(j) first derivative of shape function*

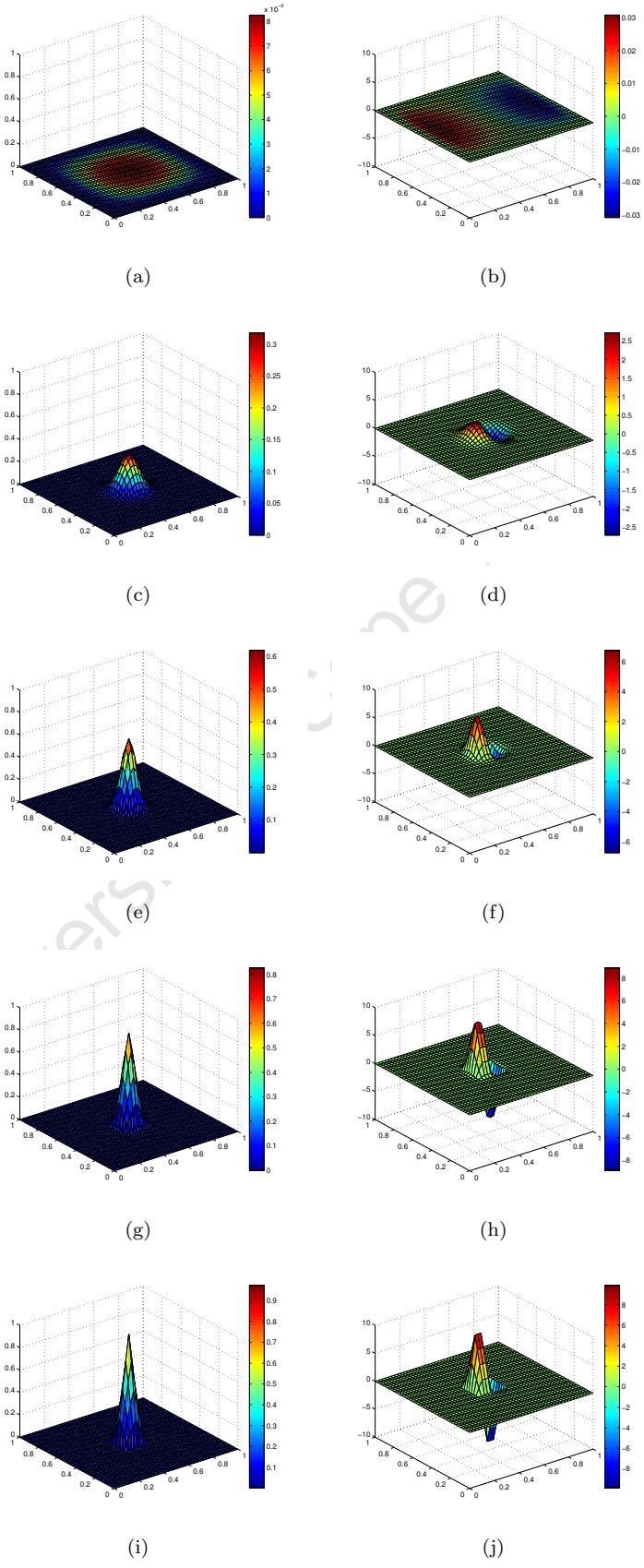

Figure 4.8: *In 2D, the transition of gamma from 0 to 6 : the left column shows the Shape functions while the right column is the first derivative of shape function*

A gradual transition from a well defined to a coarse and non-smooth Gaussian shape-like distribution is obtained in Fig 4.7 and Fig 4.8. The Delaunay basis limit has been found to be reached as from $\gamma = 6$. In 2D, the observations are confirmed as γ ranges from 0 to 6.

In their paper, Arroyo and Ortiz [1] have tried to find an optimum gamma value. They have subjected a cantilever beam problem to multiple values of gamma. The final results showed that a value of 1.8 produces results of higher accuracy at low computational resources. Choosing alternate values of γ yield solution of either low accuracy at low computational requirements or high accuracy with high computational demand. In addition, an overall degradation of the convergence has been noted. In that sense, for all the simulations carried out in this thesis, gamma will be set as a constant at its optimum value.

4.2.8.2 The nodal spacing

The nodal spacings are directly dependent on how the nodes have been scattered over the domain. A structured mesh, where all nodes are equally spaced, will result in a constant β over the entire domain. However, for an unstructured mesh set-up, where nodes have different spacings with respect to their respective neighbours, β is expected to vary. Refraining from doing so, causes the accuracy of the results to decrease drastically and may even lead to calculation failure in certain cases.

One example of finding β, can be found in the work of Arroyo et al. [21], where they have tried to find an adequate way to solve this problem by determining $\beta(x)$ through a variational approach. In this way, the discrete energy function is minimised with respect to β. Unfortunately, by using this method, the portability of LME is greatly reduced as for each constitutive equation, the variation of the strain energy function is recomputed while considering β. Moreover, it also requires that β and the shape functions be computed at each step, adding to the computational expense. Although, the authors acknowledged the disadvantage of their method, they deemed such trade-off reasonable if highly accurate solutions are needed.

In this study, the above method has not been implemented due to its impracticability and an alternative one is proposed where LME will not lose its advantages.

4.2.8.3 Approximating $\beta(x)$

To overcome the unstructured mesh problem, it is decided to use a simple method that will now be elaborated. Consider an unstructured mesh domain as illustrated in Fig 4.9.

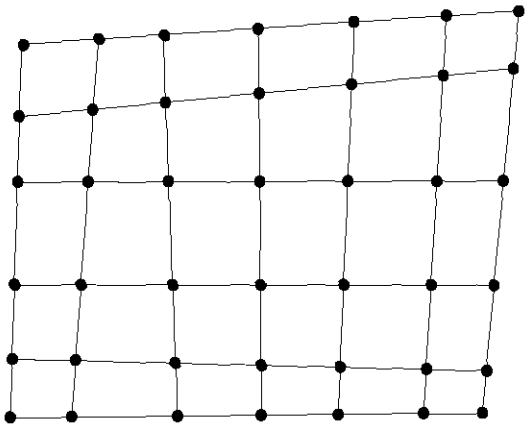

Figure 4.9: *An unstructured-meshed domain*

Zooming-in on a particular node as shown in Fig 4.10, one can, at a glance, note that the central node has different nodal spacings with respect to its neighbours.

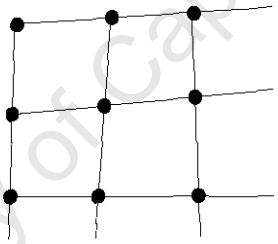

Figure 4.10: *Interior node with connected elements and neighbouring nodes*

Hence, an easy way to chose the nodal spacing is to find the average of the distances:

$$h = \frac{\sum_i^n |\mathbf{x} - \mathbf{x_i}|}{n} \tag{4.73}$$

where, n represents the number of nodes belonging to the same elements as $\mathbf{x}$

In that way, h will correspond to the definition of Arroyo and Ortiz as a "representative nodal spacing". However, as each node in the structured mesh has its own nodal spacing, we need to find a way to approximate h and its spatial gradient ∇h over the whole domain.

As an intermediate solution, it is proposed to approximate $h(\mathbf{x})$ using the MLS scheme (already

available in the code) which provides a smooth approximation of $\beta(\mathbf{x})$ over the whole domain.

$$\beta^h(\mathbf{x}) = \sum_{a=1}^{i} N_a^{MLS}(\mathbf{x})\beta_a \tag{4.74}$$

$$\nabla\beta^h(\mathbf{x}) = \sum_{a=1}^{i} \nabla N_a^{MLS}(\mathbf{x})\beta_a \tag{4.75}$$

where

- β_a : is the exact beta value at node a
- N_a^{MLS} : is the MLS shape function at node a

4.2.9 Implementation of LME

In terms of coding, the implementation of LME is carried out in such a way that only a small change to the existing code will be needed while complying with the normal work flow of SESKA (Appendix A). Apart from coding only the LME algorithm, it is necessary to implement a method that will determine the nodal spacing. The new changes allowed each particle to be assigned a value, which represents the characteristic spacing, h, that is the average distance of the nearest nodes (as shown in section 4.2.8.3 on page 35). In this way, for an unstructured mesh, each particle will have its own value of h. With the existing MLS code, the corresponding basis functions and its derivative are generated. They are then used to approximate the value of beta over the whole domain, including its first derivatives, by making use of h and γ.

Concerning the coding of the LME, a Newton-Rhapson method has to be implemented to solve the non-linear objective function as in [1] and [22]. The method is mostly driven by the Lagrange multipliers values. For each Newton iteration, the partition function, the shape function and the lambda values are computed using the set of neighbouring nodes and the particular node being considered. Based on the resulting values, the gradient (first derivative), $\mathbf{R}$ (Eq 4.68), and the *Hessian* (second derivative or Jacobian) matrix, $\mathbf{J}$ (Eq 4.69), of the objective function is computed. The starting point of the iterations is set to zero to achieve good convergence (within 3 or 4 iterations). The incremental steps of the Newton method are calculated by dividing the transpose of $\mathbf{R}$ with the negative of the Jacobian.

The normalising of $\mathbf{R}$ vector (the size of which depends on the number of dimension) is used to regulate the iteration process. In our case, once it reaches a tolerance value of 1×10^{-8}, the Newton method is stopped. The final value of the Jacobian and shape functions are then used to calculate the derivative of the basis functions in Eq 4.70. The whole process is carried out for each nodes belonging to the domain. Below is the actual algorithm implemented.

Algorithm 1 *Computing LME shape functions (Arroyo [23])*

Set TolLag;
for $p = 0$ **to** num of particles **do**
  Set $\boldsymbol{\lambda} = 0$;
  Extract supporting nodes of particle p;
  while norm($\mathbf{R}$) > TolLag **do**
    $Z(\mathbf{x}, \boldsymbol{\lambda}) = \sum_{a=1}^{N} e^{\frac{\gamma}{h_a}|\mathbf{x}-\mathbf{x}_a|^2 + \boldsymbol{\lambda}(\mathbf{x}-\mathbf{x}_a)^2}$;
    for $a = 0$ **to** num of supporting nodes **do**
      $p_a(\mathbf{x}, \boldsymbol{\lambda}) = \frac{1}{Z(\mathbf{x},\boldsymbol{\lambda})} e^{\frac{\gamma}{h_a}|\mathbf{x}-\mathbf{x}_a|^2 + \boldsymbol{\lambda}(\mathbf{x}-\mathbf{x}_a)^2}$;
    end for
    $g(\boldsymbol{\lambda}) = \log Z(\mathbf{x}, \lambda)$;
    $\mathbf{R} = \sum_{a=1}^{N} p_a(\mathbf{x}, \boldsymbol{\lambda})(\mathbf{x} - \mathbf{x}_a)$;
    $\mathbf{J} = \sum_{a=1}^{N} p_a(\mathbf{x}, \boldsymbol{\lambda})(\mathbf{x} - \mathbf{x}_a) \otimes (\mathbf{x} - \mathbf{x}_a) - \partial_{\boldsymbol{\lambda}} \log Z(\mathbf{x}, \boldsymbol{\lambda}) \otimes \partial_{\boldsymbol{\lambda}} \log Z(\mathbf{x}, \boldsymbol{\lambda})$;
    $\Delta\boldsymbol{\lambda} = \mathbf{J}^{-1}\mathbf{R}^T$;
    $\boldsymbol{\lambda} = \boldsymbol{\lambda} + \Delta\boldsymbol{\lambda}$;
  end while
  for $q = 0$ **to** num of supporting nodes **do**
    $\nabla p_b = -p_b(\mathbf{J})^{-1}(\mathbf{x} - \mathbf{x}_b) + p_b K_b \nabla\beta$;
  end for
end for

Chapter 5

Cardiac Mechanics

5.1 Introduction

In this chapter, the basic functioning of the heart and all its constituents will be presented. The macroscopic and microscopic structural components of the heart cells will be briefly introduced and their behaviour or interactions will be explained. In this work, it is assumed that the cardiac mechanics of a canine's heart is similar to that of a human's heart. For further details, the reader is referred to the textbook: Hurst's the heart [24]

5.1.1 Macroscopic Level

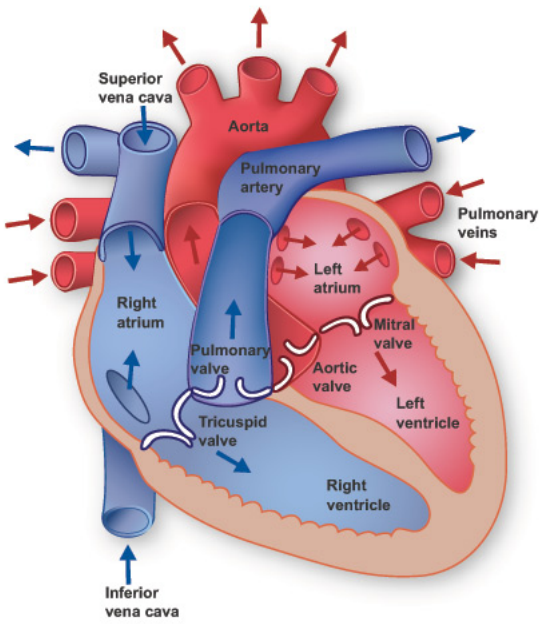

Figure 5.1: *A labelled cross-section of a human heart [4].*

Although it appears complex initially, the heart is, in fact, a well structured organ. Its main purpose is to circulate blood throughout the body in a cyclic manner which is achieved through diastolic filling and systolic contraction. The two ventricles of the heart (left and right ventricles as illustrated in Fig 5.1) fill during the diastolic period and empty during the systolic phase. These rhythmic movements consist of torsional, longitudinal and transversal displacements that are developed by the heart muscles tissue which are referred as the myocardium. The aortic and mitral valves, found at the top of the ventricle, maintain the blood in place for a brief period of time during contraction in order to accumulate enough pressure that will cause an ejection and also displace blood through the blood vessels over the whole body. If the evolution of the ventricular pressure with respect to its volume is plotted for a whole heart-beat's cycle, then the graph in Fig 5.2 is obtained.

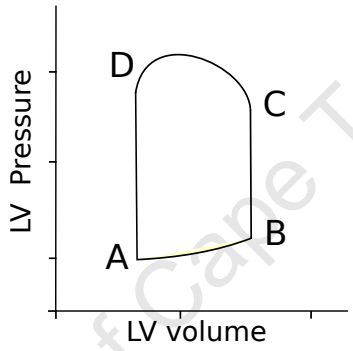

Figure 5.2: *A generalised pressure volume plot of a left ventricle.*

From A to B, the heart relaxes as the ventricles expand during filling. The final filling volume at B is known as the end diastolic volume (EDV). Between B and C, the mitral valves are closed and iso-volumetric contraction takes place, meaning that no change in cavity volume is recorded during this period. Through C to D, the aortic valves are now opened since the pressure inside the ventricle chamber is greater than in the aortic chamber. The muscles continue on contracting till the ventricles are emptied from blood. The end systolic volume (ESV) is obtained at D. From D and back to A, the ventricles relaxes again by dropping the pressure inside but without making any change in their volumes.

In cardiac modelling, the left ventricle is the most used geometry during simulations since it is responsible for pumping oxygenated blood throughout the body.

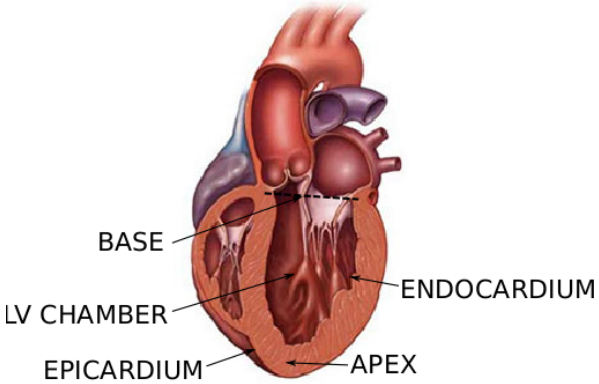

Figure 5.3: *A labelled heart cross-section [5].*

5.1.2 Microscopic Level

At the microscopic level, the molecular mechanism which drives the macroscopic process of the heart's beat can be observed. In order to properly explain the different microscopic processes, the structure of the myocardium will be looked at more closely.

The myocardium consist of fibres, called myocytes, which have a specific local orientation anywhere along or though the ventricle walls. The fibres are grouped to form a bundle of fibres, called myocardium laminas or sheet of fibres, and are separated by a substance called extracellular collagen.

Inside a myocyte, many myofibril chains, composed of a repeated component called sarcomere, are available. Sarcomeres are the contractile element of the myocardium. They are made up of two principal fibrous proteins: myosin (a thick filament) and actin (a thin filament). The myosin filament has been found to be made up of approximately 200 myosin molecules, with each of them having a myosin head. Once the concentration of calcium ions is increased, the latter reacts with these molecules. The behaviour of the globular head of the myosins changes as they now attach and pull on the actin proteins, creating a micro-tensile force, as shown in the Fig 5.4.

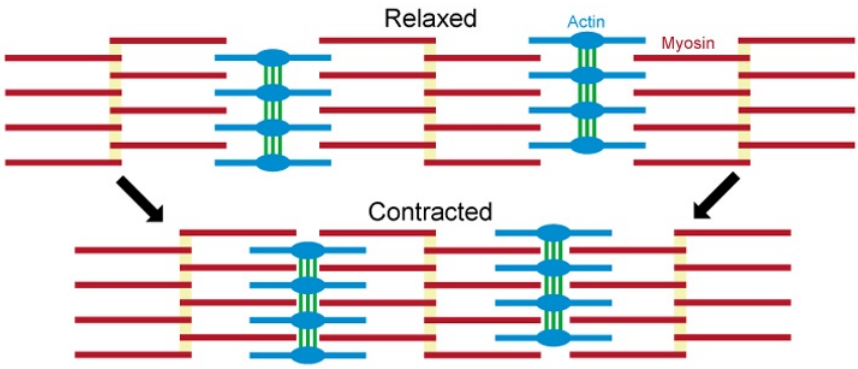

Figure 5.4: *The sarcomere layout at relaxation and during contraction. [6]*

In order to manage the presence of calcium ions at these protein levels, the electrical mechanics of the heart need to be considered. Near the atrial chambers, there exists a special region called the sinoatrial node that generates an electrical wave which first travels to the atrial chambers, where it is held for about 0.1 seconds, and then released through the His bundle (special form of myocardium cells that are dedicated in transmitting electrical signal) which branches to different direction and are connected to the Purkinje fibres. The latter is quite similar to the myordium fibres but contains less fibrils and higher concentration of glycogen. In addition, they are much thicker than regular fibres (30 micrometers). Due to these factors, the Purkinje fibres provide better and faster channel for the electrical wave to move through. The main purpose of the fibres are to redirect the electrical current from the base down to the apex. From there, the electric signal is transferred to the myocardium fibres where the conductivity is lower.

At the myocytes level, the electrical wave triggers an ion current which is responsible in creating a large potential difference between the inside and outside of the negatively charged cell membranes of the myocytes. This therefore induces the opening of cell membrane's gates which allow certain ions to move inside, to restore the potential equilibrium. These ions, which consist partly of calcium ions, start to then react with the globular heads of the myosins.

5.1.3 Myocardial Infarction

Myocardial infarction, more commonly known as heart attack, is a major blockage of the coronary artery that provides oxygenated blood to a portion of the heart muscles, which is caused by fats deposits or blood clotting that occupies the whole cross section of the blood vessel. In that particular situation, the myocardium cells do not receive adequate oxygen as well as nutrients supply and subsequently die, forming a scar of dead cells which hampers the heart function.

To restore the blood supply, the heart now needs to make more efforts during the pumping process as the work load of the infarct region is redistributed to the remaining healthy part of

the heart. Observations showed that this stage usually causes the followings:

1. Decrease in the overall blood volume supplied
2. A higher stress measurement in the infarction region, causing a rupture of the ventricle wall in certain conditions.
3. Increase in heart rate
4. Remodelling of the ventricles wall during the healing process to account for the heart handicap.
5. Bulging may occur at the infarct region, increasing drastically the stress along the thinner wall cross-sectional area.

Because the scar of the myocardial infarction changes with time, the associated physiological and mechanical properties of each stage will be elaborated, by making use of Holmes et al's [25] work.

5.1.3.1 Acute Ischemia

The acute ischemia stage is an early phase of the infarct process that lasts for a few hours. The scar starts its formation and any loading condition influences its final shape. The wall at this region undergoes 10% thinning and stretching during the heart's beats and does no longer participate in the contraction. Thus, it now behaves only as a passive non-linear viscoelastic material (quite similar to the normal passive behaviour of normal heart tissue) with higher stresses. At the end of the process, the scar is much stiffer than a healthy tissue.

5.1.3.2 Necrotic

The stage between the first few hours and the first few days is called the necrotic stage. In that period, the infarct starts to heal. Fibroblast and collagen are deposited in this area to support the growth of healthy tissue. Unfortunately, the necrotic stage represents the most critical phase of an infarct since most wall ruptures occur during that period. A mild thinning still takes place as the dead cells start to leave the region resulting in a small increase in wall stress. In this study, the infarct is considered to be in this phase since any treatment given will positively impact on the next phase.

5.1.3.3 Fibrotic

The start and ending of the fibrotic period varies depending on the mechanism taking place in the infarct region. The fibrotic stage is said to begin as soon as the deposits of fibroblast and collagen increase rapidly. Once the latter dominates the mechanical properties of the infarct region, the end of the fibrotic stage has been reached. This whole process can take up to a few weeks or even months. During this time, the infarct region is very stiff. It limits the stretching of the surrounding healthy myocardium during the diastolic phase. Shortening of the fibres parallel to the infarct area and radial expansion are expected to be affected during systolic activities.

5.1.3.4 Remodelling

The remodelling is an on-going process of the healing mechanism. The amount of collagen continues on increasing while the stiffness of the infarct starts to decrease to a magnitude that is still higher than the healthy or acute ischemic myocardium. The scar volume reduces gradually over time and a partly working left ventricle system is recovered.

5.1.4 Hydrogel Injection Therapy

Several medical treatments to limit the effects of myocardial infarction can be found in literature and have been used with relative success [26]. However, a novel technique called hydrogel injection therapy will be focused on. In this method, a hydrogel material is injected into the heart. The injectate is actually a 99% water-based fluid which solidifies to a porous semi-solid material, stiffer than a scar infarct or healthy tissue, once its temperature increases to the normal body temperature. The principles behind the use of hydrogel are to:

- Reinforce the infarct,
- Maintain the wall thickness,
- Limit expansion of the border-zone,
- Prevent left ventricular dilatation,
- Reduce adverse effects of remodelling,
- Normalised the stress distribution in the ventricular wall, and
- Improve the global function of the heart

Several recent studies ([27], [26] and [28]) have been carried out to understand the mechanics of the hydrogel as well as its behaviour. Up to now, it has been found that the gel penetrates in-between the muscles fibres and interacts with the myocardium extracellular matrix (ECM) structures, thus forming a composite material which alters the mechanical behaviour of the infarct at these places. To optimise the positive effect of the hydrogel, the material properties has to be tailor-made. The aim is therefore to have a final product that can:

- Provide a fluid that has good penetration properties. I.e, the fluid needs to have a low viscosity value and also a longer gelation time
- Have an acceptable degradation time so that the hydrogel remains in the infarct for the healing period but not indefinitely.

5.2 Passive Mechanics Behaviour

During the filling, the myocardium is deforming in a passive fashion. Numerous different models have since the last 30 years been used in literature but most of them are quite closely linked together. In total, 3 major categories of passive mechanics strain energy can be differentiated.

The description of the categories, given in the paragraph below, is summarised from Usyk et al. [2]

Isotropic constitutive model The first model [29] that was previously used, was based on the isotropic constitutive equation which is based on a simple Mooney-Rivlin strain energy function. The equation was found to be ideal in predicting large deformation as encountered in cardiac simulations. However, to have one which is more suited to predict stress and strains in heart tissue, an exponential term, which includes in the first principal invariant of the right Cauchy-green deformation tensor, was added to the potential energy function which also includes a stress scaling factor, C. In order to cater for the assumption that the myocardium muscles are incompressible, a Lagrange multiplier, p, was incorporated. The final form of the strain energy function is as follows:

$$W = C\left(e^{b(I_1-3)} - 1\right) + \frac{p}{2}(I_3 - 1) \tag{5.1}$$

Transverse Isotropic constitutive model With the isotropic material behaviour, the approximation is very poor because it does not consider the myocardium preferred direction. Using a transversal isotropic strain energy function, the new passive constitutive law is now defined by three material constants which are determined from the biaxial test. By also including the compressibility term, the resulting equation obtained from Usyk et al. [2] is:

$$W = C\frac{\left(e^{Q} - 1\right)}{2} + C_{compr}(I_3 \cdot ln\, I_3 - I_3 + 1) \tag{5.2}$$

with

$$Q = b_{ff}E_{ff}^2 + b_{xx}(E_{cc}^2 + E_{ss}^2 + E_{cs}^2 + E_{sc}^2) + b_{fx}(E_{fc}^2 + E_{cf}^2 + E_{fs}^2 + E_{sf}^2)$$

where both the material constant b_{ij} and the *Green strain* tensor E_{ij} is direction dependent. i and j refer to either the fibre axis, f or sheet axis s or the sheet-normal axis c. The values of the compressibility term is used to enforce nearly incompressible behaviour. Regarding the parameters, different sets of values are needed if a canine, rat or human heart is to be considered as each one behaves differently. This therefore gives a higher accuracy in relating stress and strain within each model and also results in a better approximation with respect to experimental data.

Orthotropic constitutive model The orthotropic material constitutive law (Eq 5.3) is a generalisation of the transversely isotropic material. In this case, all 3 material directions of the fibre sheets can be considered. In this way, the effect of inter-laminar tensile and shear stiffness can be easily regulated to increase the accuracy of the material behaviour. On the other hand, it also leads to another increase in the number of material constants which is difficult to determine through experiments. The following equation given in Usyk et al. [2] describe an othotropic material:

$$W = C\frac{\left(e^{Q} - 1\right)}{2} + C_{compr}(J \cdot ln\, J - J + 1) \tag{5.3}$$

with

$$Q = b_{ff}E_{ff}^2 + b_{cc}E_{cc}^2 + b_{ss}E_{ss}^2 + b_{cs}(E_{cs}^2 + E_{sc}^2) + b_{fs}(E_{fs}^2 + E_{sf}^2) + b_{fc}(E_{fc}^2 + E_{cf}^2).$$

In this study, a modified orthotropic constitutive equation is used with transverse isotropic material parameters. In that way, the actual model behave according to a modified transversely isotropic equation. The slight modification is implemented into by changing the way in the equation Q is defined with respect to the *Green strain* tensors. Q is now defined by:

$$\begin{aligned} \mathrm{Q} =& a_1E_{ff}^2 + a_2E_{cc}^2 + a_3E_{ss}^2 + a_4(E_{ff}^2 + E_{fc}^2 + E_{fs}^2) && (5.4)\\ &+ a_5(E_{cf}^2 + E_{cc}^2 + E_{cs}^2) + a_6E_{sf}^2 + E_{sc}^2 + E_{ss}^2) && (5.5)\end{aligned}$$

where $a_k, k = 1...6$ are the new coefficients that regulate the *Green strain* tensors. A transformation matrix is then identified to help the conversion of the othotropic materials into the modified one. This approach relates b_{ij} with a_k, through the following system of equation :

$$\begin{bmatrix} 1 & 0 & 0 & 1 & 0 & 0 \\ 0 & 1 & 0 & 0 & 1 & 0 \\ 0 & 0 & 1 & 0 & 0 & 1 \\ 0 & 0 & 0 & 1 & 1 & 0 \\ 0 & 0 & 0 & 1 & 0 & 1 \\ 0 & 0 & 0 & 0 & 1 & 1 \end{bmatrix} \begin{bmatrix} a_1 \\ a_2 \\ a_3 \\ a_4 \\ a_5 \\ a_6 \end{bmatrix} = \begin{bmatrix} b_{ff} \\ b_{cc} \\ b_{ss} \\ 2b_{fc} \\ 2b_{fs} \\ 2b_{cs} \end{bmatrix}. \tag{5.6}$$

The set of values taken for this project are obtained from Usyk et al [15] (calibrated with experimental data) and represent a canine left ventricle. The values are summarised in table 5.1(a). From there, the transformation matrix us applied and the new values are obtained (see table 5.1(b))

(a) Usyk Values

Parameters	Coefficients
C(kPa)	0.88
C_{compr}	3.0
b_{ff}	6.0
b_{cc}	5.0
b_{ss}	5.0
b_{cs}	6.0
b_{fs}	6.0
b_{fc}	6.0

(b) Modified Values.

Parameters	Coefficients
C(kPa)	0.88
C_{compr}	3.0
a_1	0.0
a_2	-1.0
a_3	-1.0
a_4	6.0
a_5	6.0
a_6	6.0

Table 5.1: Parameters for the Passive Stress equation representing a canine LV

5.3 Homogenisation Approach

An infarct is most of the time accompanied by a loss in collagen and dead myocytes. To simulate this effect, a homogenisation approach is used to define any point in the geometry to be made up of an infarcted myocardium volume fraction and a dummy material with negligible stiffness (where the latter represent a loss in material). Similar methods have been implemented in the case of Elasticity [30] and Elasto-plasticity [31].

$$\Psi_{\text{Total}} = \sum_{I=1}^{M} \eta_I \Psi_I, \text{ with } I = 1, .., M \tag{5.7}$$

$$\tag{5.8}$$

where M, is the number of superimposed material phases with their corresponding volume fractions associated with the stored energy function, Ψ_I. It is ensured that $\sum_{I=1}^{M} \eta_I$ holds so as to have the appropriate physical response. The second *Piola kirchhoff* stress, $\mathbf{S}$, can also be determined from the previous equation by taking the derivative of the strain energy function with respect to the *Green strain* tensor:

$$\mathbf{S} = \frac{\partial \Psi}{\partial \mathbf{E}} = \sum_{I=1}^{M} \eta_I \frac{\partial \Psi_I}{\partial \mathbf{E}}. \tag{5.9}$$

In that sense, the healthy myocardium consists of only a single active anisotropic phase while the infarct region is made up of an anisotropic and an isotropic phase, where the latter refers to the dummy material.

The isotropic behaviour is hereby described by the Neo-Hookean strain energy function (Eq 5.10). The reason for choosing this material property is mainly to predict the behaviour of a hydrogel injectate that will be used in future research by either simply increasing the stiffness of the material properties or having specific material constant for μ and λ.

$$\Psi_{\text{dummy}} = \frac{\mu}{2}(\mathbf{C} : \mathbf{1} - \mathbf{3}) - \mu \ln J + \frac{\lambda}{2}(\ln J)^2. \tag{5.10}$$

Preliminary experiments carried out, based on the indentation test, have yielded values for μ and λ as listed in table 5.2. However for the dummy material, the stiffness of the hygrogel is reduced to 1%.

	Hydrogel stiffness	
Coefficient	100%	1%
μ	24.6	0.246
λ	983.6	9.836

Table 5.2: *Hydrogel and Dummy material*

5.4 Active Contraction

The active stress is used to simulation of the heart contraction after the diastole. In that phase, the heart usually contracts and twist about its own axis to expel the blood out of the ventricles.

During a cardiac contraction, the myocardium fibres create a tensile force due to an electrical excitation caused when a gradient in concentration of electric charged ions is built-up across the cells. This electric signal occurs in a cyclic pattern, synchronised to the lapse of time of a heart beat, and propagates through the heat muscles in a wave-like manner. Fig 5.5 shows the variation of the electric current flow over time in one particular myocytes:

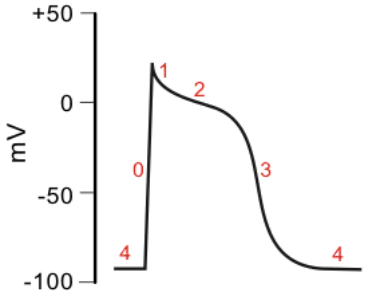

Figure 5.5: *Action potential of a ventricular myocytes*

The following stages explain in more detail the interactions at the cellular level:

- If the membrane potential of the cells are at their lowest (i.e -85mV), all the rapid Na^+ channels open-up allowing a very rapid influx of Na^+ ions resulting in the potential to rise up to +52mV.
- A minor drop in the electrical gradient is registered as Cl^- and K^+ are driven out by specific channels.
- Using the depolarisation activated Ca^{2+} channel, Ca^{2+} ions are introduced inside the cell as a current. But since there is also an outward movement of positive ions (K^+), the resulting charge of the cell remains constant.
- At the same time, free intra-cellular Ca^{2+} is released by the same cell-sarcoplasmic reticulum causing an electrical gradient across the membrane, where each cell can now be considered as a battery. This process is called the calcium-induced calcium release process.
- The free intra-cellular Ca^{2+} then migrates on the myo-filaments protein troponin which allows binding of actin to myosin, starting the contraction process.
- In order to have relaxation, the concentration of $[Ca^{2+}]_i$ must decrease below a required level through the transport system that is made up of SR Ca^{2+} ATPase, sarcolemma

Na^+/Ca^{2+} exchange, sarcolemma Ca^{2+} ATPase or mitochondrial. This causes the cells to be re-polarised to the resting state.

- Meanwhile, the potassium and chlorine ions are still being moved out, causing a gradual decrease in the cell-charge down to a stabilisation point where no net inflow of ions is recorded.

5.4.1 Active stress model

In this project, the work of Guccione et al [3] is used to model the active contraction. They formulated the constitutive equation, incorporating the characteristics of the heart muscles, fibre orientation and activation sequence, to obtain the stresses and strains. This constitutive equation has been derived from experimental data plots and literature. The authors took into account the main mechanisms of contraction at the cellular level. To do so, he defined the right Cauchy stress tensor, $\mathbf{T}$, as a summation of the active and passive stress tensor:

$$\mathbf{T} = \mathbf{T}^{(p)} + \mathbf{T}^{(a)} \tag{5.11}$$

where

- $\mathbf{T}^{(p)}$: Passive stress tensor
- $\mathbf{T}^{(a)}$: the fibre oriented active stress tensor

$\mathbf{T}^{(a)}$ is then derived as follows:

$$\mathbf{T}^{(a)} = T_0 \, \mathbf{q} \otimes \mathbf{q} \tag{5.12}$$

where,

- $\mathbf{q}$ is the fibre direction
- T_0 is active tension developed by myocytes.

Guccione et al [3] considered three different approaches to find T_0. In the first model, they used different sarcomere lengths, along with their corresponding shortening velocities, that dictate the magnitude of the contraction force. In a second one, they relied on the Hill model, which is based on the chemical equilibrium of the tension inducer ion, Ca^{2+}. Finally, they also considered the elastance model which is built on a modified Hill model. The authors still calculated the tension force by looking at the actual fraction of Ca^{2+} ions, at a specific time, out of the overall maximum concentration. Based on that ratio, a relative tensile force is computed using the following equation

$$T_0 = T_{max} \frac{Ca_0^2}{Ca_0^2 + ECa_{50}^2} C_t \tag{5.13}$$

where T_{max} is the maximum amount of tension developed by the sarcomere. Ca_0 is the calcium ion concentration. ECa_{50}^2 is the length-dependent calcium sensitivity and depends on the sarcomere length and the maximum Ca^{2+} ion concentration.

$$ECa_{50} = \frac{(Ca_0)_{\max}}{\sqrt{exp[B(l - l_0)] - 1}}. \tag{5.14}$$

B is a constant. The length of the sarcomere can also be computed if it is assumed change in the transversal direction of the heart, i.e, the thickness of the wall. This can be shown in the equation below:

$$l = l_R\sqrt{\mathbf{C} : (\mathbf{q} \otimes \mathbf{q})} \tag{5.15}$$

where l_R is the sarcomere length at the relaxed stage with no stresses and $\bar{E}_{FF}$ is the strain tensor along the principle fibre-axis direction. Regarding the unknown, C_t in Eq 5.13, which is dependent of the actual time of the model calculation, Guccione et al defined it as a cosine function.

$$C_t = \frac{1}{2}(1 - cos\ \omega). \tag{5.16}$$

ω is then defined in three phases.

$$\omega \begin{cases} \pi\frac{t}{t_0} & 0 \leq t \leq t_0 \\ \pi\frac{t-t_0-t_r}{t_r} & t_0 \leq t \leq t_0 + t_r \\ 0 & t_0 + t_r \leq t \end{cases} \tag{5.17}$$

where t is the actual time, t_0 is the time at which peak-contraction occurs, and t_r represents the relaxation period. When the sarcomere length is known, t_r can be computed for the simple linear equation where m and b are constants.

$$t_r = ml + b. \tag{5.18}$$

In this study, the values of the constants and variable introduced above are obtained from Guccione et al. [32] and used to carry out the systolic calculation. The values are:

Parameters	Values
$T_{\max}$ [kPa]	56.7
Ca_0 [μM]	4.35
$(Ca_0)_{\max}$ [μM]	4.35
m [μm^{-1}]	1.05
b [s]	-1.43
B [μm^{-1}]	4.75
l_0 [μM]	1.58
l_R [μM]	1.78 - 1.91
T_0 [s]	0.25

Table 5.3: Active stress parameters used during the systolic simulation

Going back to Eq 5.11 , $\mathbf{T}^{(p)}$ is the passive stress that is calculated during diastolic phase. While it describes the stress state of ventricular expansion from the passive stress constitutive laws, $\mathbf{T}^{(a)}$ will cause a subsequent contraction which needs to work against $\mathbf{T}^{(p)}$. Since, both stress tensors are added to produce the resulting stress tensor, $\mathbf{T}^{(a)}$ needs to be greater than $\mathbf{T}^{(p)}$ for an actual active contraction displacement to take place.

5.4.2 Iso-volumetric Contraction

During the first stage of the systolic contraction, the myocardium contracts, pressuring the blood inside the ventricle since the mitral and aortic valves are closed. In this case, a computational algorithm that is able to mimic this behaviour has been implemented. Based on the current time loading step and the sarcomere length, the corresponding active contraction forces are computed to counteract the build-up in cavity pressure. The following algorithm has been implemented to do so:

- Consider residual discrete equation system (based from Eq) for each time step n and iteration step i where the required volume change $\Delta V = 0$,

$$\Psi_n^i(\mathbf{u}_n^i) + \Delta\lambda_n^i \mathbf{f}_{ext,0} = \mathbf{K}_n^i \Delta\mathbf{u}_n^i = 0 \tag{5.19}$$

  where,

  - λ_n^i is a current loading factor.
  - $\Psi = \lambda_n^i \mathbf{f}_{ext,0} - \mathbf{f}_{int}$

- Making the unknown displacement field increment subject of formula

$$\Delta\mathbf{u}_n^i = (\mathbf{K}_n^i)^{-1}\Psi_n^i(\mathbf{u}_n^i) + \Delta\lambda_n^i(\mathbf{K}_n^i)^{-1}\mathbf{f}_{ext,0} \tag{5.20}$$

- Two equation system is now needed to be solved for,

$$\mathbf{K}_n^i \Delta\mathbf{u}_{\Psi,n}^i = \mathbf{u}_n^i \tag{5.21}$$

$$\mathbf{K}_n^i \mathbf{u}_{ext,n}^i = \mathbf{f}_{ext,0} \tag{5.22}$$

  with the reference external loading vector $\mathbf{f}_{ext}$ due to a given end pressure p_0

- Eq 5.20 can now be re-written by considering Eq 5.21 and Eq 5.22

$$\Delta\mathbf{u}_n^i = \Delta\mathbf{u}_{\Psi,n}^i + \Delta\lambda_n^i \mathbf{u}_{ext,n}^i \tag{5.23}$$

- At each time loading step n, $\mathbf{u}_{ext,n}^0$ is readjusted using an initial loading correction factor $\Delta\lambda_n^0$ to have the external loading vector close to the current loading as it is deformation dependent.

$$\mathbf{f}_{ext,0}^\star = \lambda_{ref}\mathbf{f}_{ext}(p_0) \qquad \text{with} \qquad \lambda_{ref} = \Delta\lambda_n^0 \tag{5.24}$$

- Hence, Eq 5.20 can be expressed as

$$\Delta\mathbf{u}_n^i = (\mathbf{K}_n^i)^{-1}\Psi_n^i(\mathbf{u}_n^i) + \lambda_{ref}^{-1}(\Delta\lambda_n^i(\mathbf{K}_n^i)^{-1}\mathbf{f}_{ext,0}^\star) \tag{5.25}$$

$$= \Delta\mathbf{u}_{\Psi,n}^i + \lambda_{ref}^{-1}(\Delta\lambda_n^i \mathbf{u}_{ext,n}^i) \tag{5.26}$$

- $\Delta\lambda_n^i$ can be determined by looking at a single calculation step for a give ΔV_0

$$\Delta V_0 = \sum_{k=0}^{i-1}[\Delta V_n^k(\Delta \mathbf{u}_n^k)] + \Delta V_n^i(\Delta \mathbf{u}_n^i \tag{5.27}$$

$$= \sum_{k=0}^{i-1}[\Delta V_n^k(\Delta \mathbf{u}_n^k)] + \lambda_{ref}^{-1}\Delta\lambda_n^i \Delta V_{n,ext}^i(\mathbf{u}_{ext,n}^i) + \Delta V_n^i(\Delta \mathbf{u}_{\Psi,n}^i) \tag{5.28}$$

  where $\sum_{k=0}^{i-1}[\Delta V_n^k(\Delta \mathbf{u}_n^k)]$ is the accumulated volume change during the current time step n, $\Delta V_{n,ext}^i(\mathbf{u}_{ext,n}^i)$ the volume change due to the reference external loading p_0 multiply by a loading correction factor $\Delta\lambda_n^i$ and finally, $\Delta V_n^i(\Delta \mathbf{u}_{\Psi,n}^i)$, the change due to preliminary displacement correction $\Delta \mathbf{u}_n^k$.

- $\Delta\lambda_n^i$ can be calculated as:

$$\Delta\lambda_n^i = \lambda_{ref}\frac{\Delta V_n - \sum_{k=0}^{i-1}[\Delta V_n^k(\Delta \mathbf{u}_n^k)] - \Delta V_n^i(\Delta \mathbf{u}_{\Psi,n}^i)}{\Delta V_{n,ext}^i \mathbf{u}_{ext,n}} \tag{5.29}$$

  with $\Delta V_n = 0$

- The loading factor is then updated

$$\lambda_n^i = \lambda_n^{i-1} + \Delta\lambda_n^i \tag{5.30}$$

- and the displacement can be computed as follows:

$$\Delta \mathbf{u}_n^i = \Delta \mathbf{u}_{\Psi,n}^i + \lambda_{ref}^{-1}\Delta\lambda_n^i \mathbf{u}_{ext,n} \tag{5.31}$$

5.5 The LV ellipsoidal model

In this study, we focus on an ellipsoidal model since it represents a better approximation of the LV. Several studies [15, 33, 34, 35] have used such model and reliable results were obtained.

5.5.1 Spheroid Prolate Coordinates

In order to generate our LV model, the prolate spheroidal coordinate has been used. Basically, it allows the construction of a 3D ellipsoidal model by rotating an ellipse around its own axis in the Cartesian coordinate system using the followings equations:

$$\begin{aligned} x &= a\ \sinh\eta\ \sin\theta\ \cos\phi \\ y &= a\ \sinh\eta\ \sin\theta\ \sin\phi \\ z &= a\ \cosh\eta\ \cos\theta \end{aligned} \tag{5.32}$$

where,

- a is the focal distance between the major and minor axes measured from the origin

- η, θ and ϕ are constants that define the prolate coordinates

Based on the variations of the constants, geometries can be formed from the above equations. For example, if we consider $\phi = 0$, that is we are working only in the $x - z$ plane (Fig 5.6(b)) since $\sin\phi$ will set $y = 0$, then the following relationships can be derived:

- For η is fixed, $\sin\theta$ and $\cos\theta$ can take the form of

$$\sin\theta = \frac{x}{a\ \sinh\eta}\ ,\ \sin\theta = \frac{z}{a\ \sinh\eta} \tag{5.33}$$

  If the trigonometry identity, $\sin^2\theta + cos^2\theta = 1$, is used, then the equation of an ellipse is formed:

$$\frac{x^2}{(a\ \sinh\eta)^2} + \frac{z^2}{(a\ \sinh\eta)^2} = 1 \tag{5.34}$$

- For θ is fixed, $\sinh\eta$ and $\cosh\eta$ can take the form of

$$\sinh\eta = \frac{x}{a\ \sin\theta}\ ,\ \cosh\eta = \frac{z}{a\ \cos\theta} \tag{5.35}$$

  Applying $\cosh^2\eta - \sinh^2\eta = 1$ therefore results in a hyperbolic equation:

$$\frac{z^2}{(a\ \cos\theta)^2} - \frac{x^2}{(a\ \sin\theta)^2} = 1 \tag{5.36}$$

If now ϕ is to be varied, then each of the above shapes will form a 3D body by being rotated around the z-axis as shown in Fig 5.6(a), where each point represent the intersection of an ellipsoid, hyperboloid and a plane.

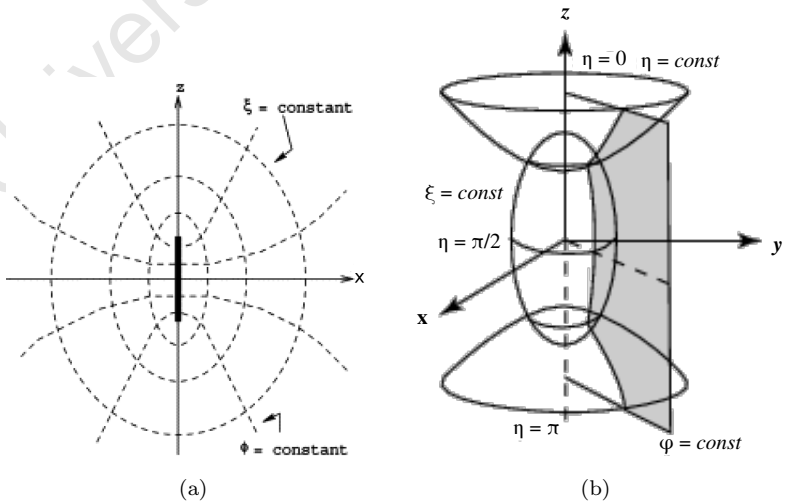

(a) (b)

Figure 5.6: *(a) A 2D representation of the Prolate Spheroidal coordinate system. Note, in this diagram $\xi = \eta$, $\phi = \theta$ and $\theta = \phi$ [7] (b) A 3D representation of the ellipse, hyperbola and plane intersecting each other ($\xi = \eta$ and $\eta = \theta$) [8]*

The full step-by-step procedure on how the ellipsoid has be constructed from the spheroidal coordinate system equations is given in Appendix B

Chapter 6

Benchmarking

6.1 Introduction

In order to validate the LME implementation, several tests are carried out. The approximation and convergence of LME basis are the most important properties which is monitored. With regards to the cardiac mechanic aspects, a special beam, composed of several myocardial materials, is defined to test the involved constitutive laws. Thus, overall, three benchmark tests are devised as follows:

1. Cantilever beam
2. Cooks membrane
3. Composite beam under tension

Note: In this chapter and in the upcoming ones, the term *mesh* is defined as a distribution of nodes over a domain.

6.2 Cantilever Beam Problem

In this example, a simple cantilever beam model with a square cross-section, depicted in Fig 6.1(a), is looked at to find out the approximation accuracy of LME compared to MLS. Two cases are studied: one with a structured mesh while the other with an unstructured mesh. The *St Venant-kirchhoff* material constitutive law is assumed. In terms of boundary conditions, the left-end side of the beam is fixed while the Neumann boundary condition is assigned on the right-end side with a surface traction of 1 $\mathrm{N/m^2}$ along the cross-section face, acting in the downward direction. The structured beam model is discretized by 52 to 416 hexahedral elements. The solution of the tip deflection computed with $\delta = \frac{Pl^3}{3EI}$, is found to be 0.4 m.

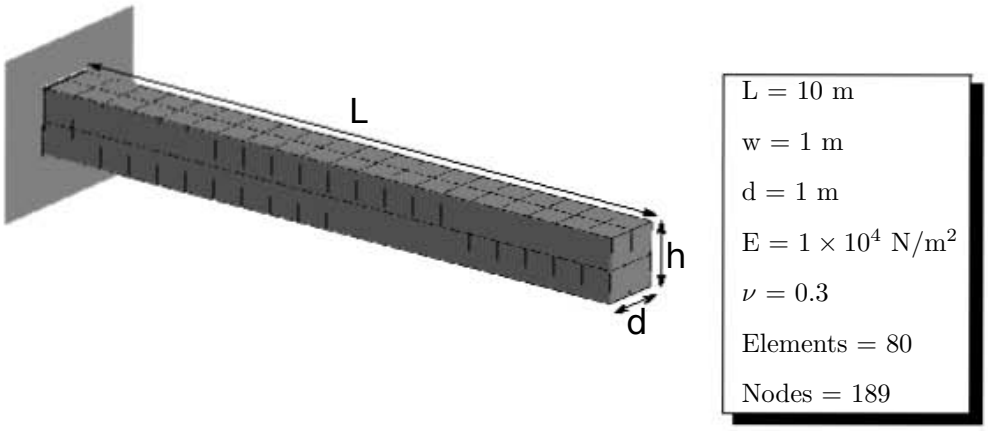

Figure 6.1: *Definition of the cantilever beam problem*

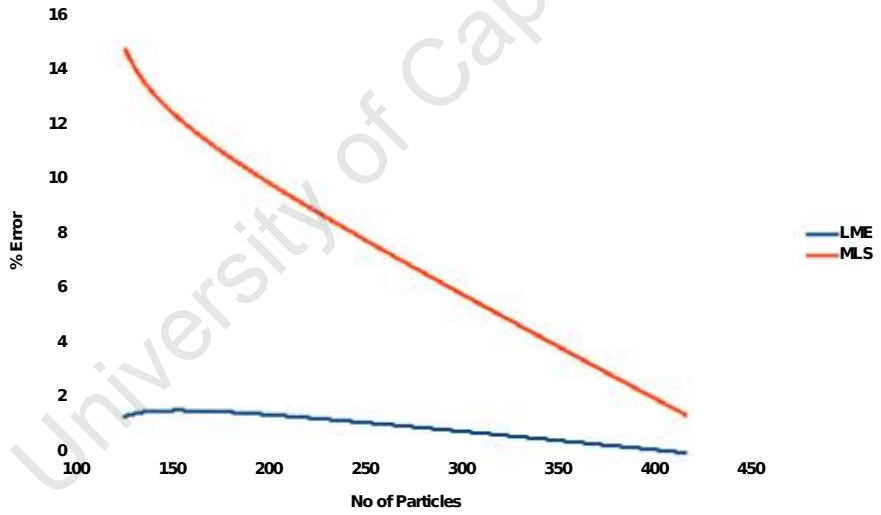

Figure 6.2: *Convergence of plot of LME and MLS by using the structured discretised cantilever beam*

After the calculation process, the final tip displacements are recorded. Their corresponding errors are calculated and plotted against the number of nodes for each model. The graph in Fig 6.2 shows that LME is able to accurately approximate displacements. In the case of structured mesh, the solution of LME is very close to the exact solution with an error margin of less than

2%.

In regards to the unstructured model, the beam is discretised with tetrahedral elements in order to have better random distribution of the nodes. This leads in having models with different densities of nodes ranging from 228 to 911 nodes. All the other properties are kept the same as in the hexahedral discretised model.

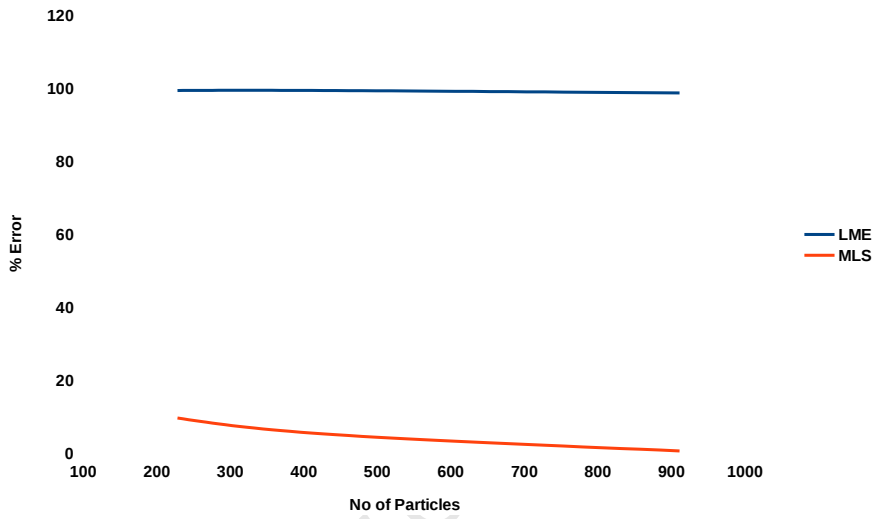

Figure 6.3: *Convergence of plot of LME and MLS by using the unstructured discretised cantilever beam*

The results, presented in Fig 6.3, shows that the solutions of MLS in the unstructured case are almost on par with those in the structured case. However for LME, the approximation induced large errors, about 100% higher than the exact solution. The reason is due to the variable β which depends on the nodal spacing, thus increasing the sensitivity of the approximation method with respect to the mesh configuration.

6.3 Cooks membrane problem

The next problem is a Cook's membrane model shown in Fig 6.4. Five discretisation levels with hexahedral elements ranging from 18 - 240 nodes are considered. The model has also been treated as a *St Venant-kirchhoff* problem in this case also. On the free right end, a surface traction acting in the upward direction is applied while the left-end side is fixed. In this case, the exact solution [36] of the model is 23.91.

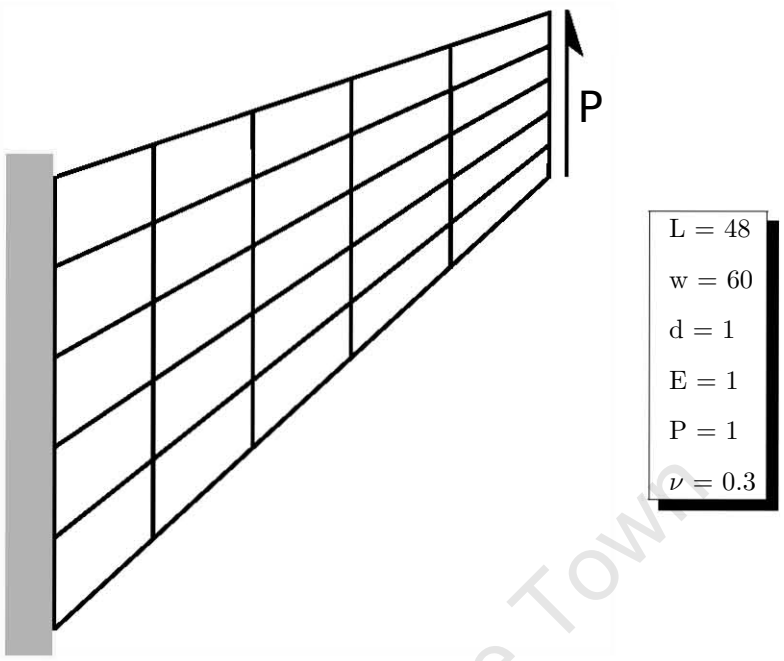

Figure 6.4: *Definition of Cook's Membrane problem*

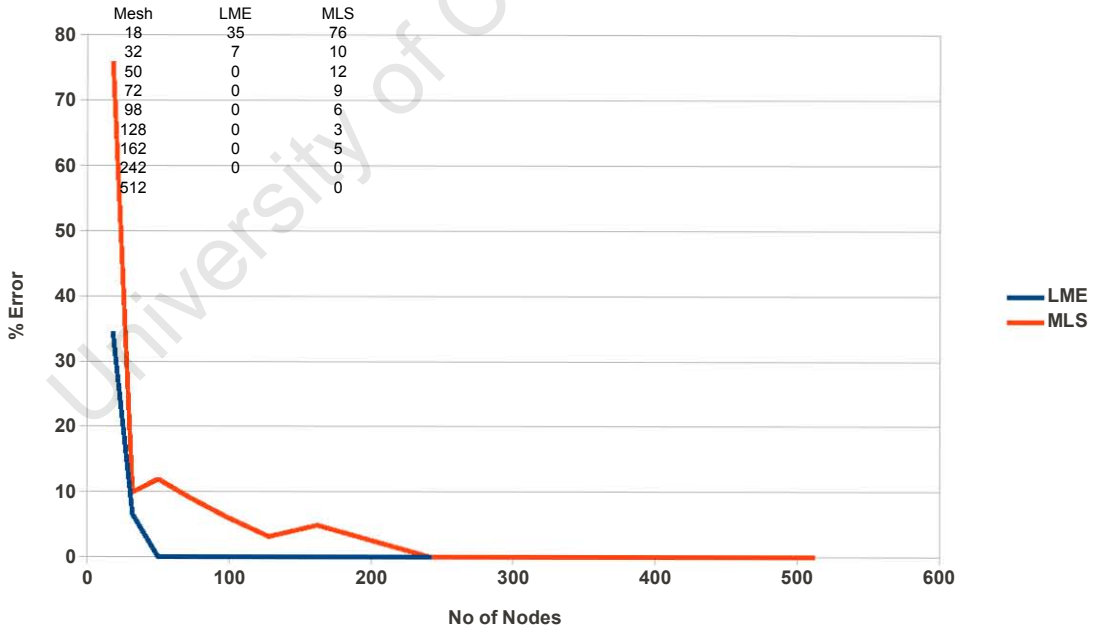

Figure 6.5: *Convergence plot of LME and MLS by using the Cooks's membrane problem*

In this benchmark test, the graph, in Fig 6.5, shows that LME converges more rapidly to the exact solution than MLS, which requires more elements. This indicates that LME requires a less refined mesh to produce an acceptable solution. Moreover, the results are also in line with the statement of Arroyo and Ortiz [1] that LME facilitates reduced integration schemes.

6.4 Composite beam under tension

In order to validate the different constitutive laws that have been implemented in Seska to model the mechanic behaviour of the heart, a simple square cross-section problem is devised to test active contraction and passive deformation of a structure composed of materials found in the healthy and infarcted heart illustrated in Fig 6.6. In this particular situation, only one fibre direction, which is parallel to the beam's longitudinal axis, has been considered. The beam is subjected to two surface tractions of 1 kN/m^2, acting in opposites. At the mid-plane of the beam, the following essential boundary conditions are imposed as shown in Fig 6.7.

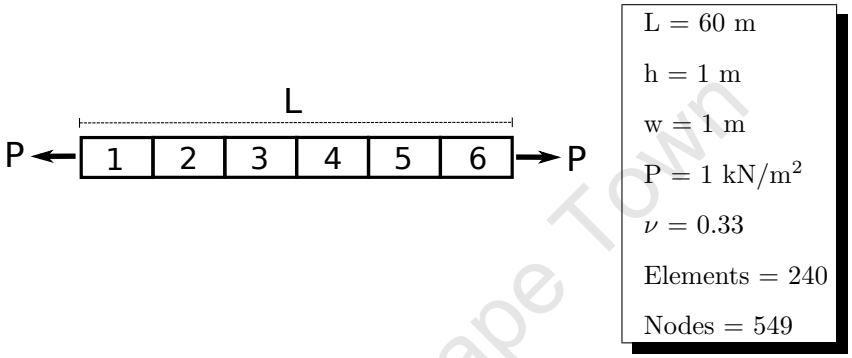

Figure 6.6: *Problem definition of a beam with different materials*

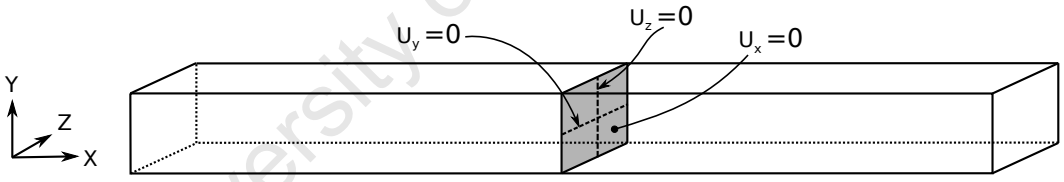

Figure 6.7: *Dirichlet boundary condition applied to composite beam*

Parameters	C(kPa)	C_{compr}	a_1	a_2	a_3	a_4	a_5	a_6
Coefficients	0.40	3.0	-6.0	-5.0	9.0	1.2	1.2	-6.0

Table 6.1: *Parameters used with the Passive Stress constitutive equation*

These conditions are applied to prevent movement of the whole geometry and also to have a centre of contraction as in the case of an actual heart model. Regarding the material properties, the beam is splitted into 6 parts (as shown in Fig 6.6) to account for their different combinations. One of the combinations will include a hydrogel treated infarct model in order to validate the homogenisation approach. The cases considered are:

1. Model: **Healthy**
   The whole beam consists of an active myocardium (healthy tissue) as shown in Fig 6.8

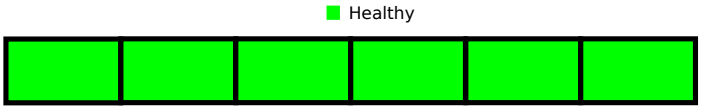

Figure 6.8: *Composite beam made up of healthy tissue only*

2. Model: **Infarct-90**
   An infarct region with 10% dummy material and same stiffness as a healthy tissue is defined(Fig 6.9)

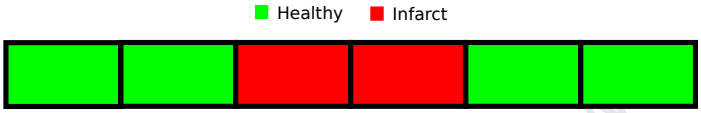

Figure 6.9: *Composite beam made up of healthy and infarct tissue with different dummy fractions*

3. Model: **Infarct-50**
   The fraction of dummy material in the Infarct-90 model is increased to 50% in the infarct.
4. Model: **Infarct-x2 stiff**
   In this case, the stiffness of the infarct region in the Infarct-90 model is doubled.
5. Model: **Infarct+HG**
   A hydro-gel with 15% of its original stiffness is injected in the infarct region of the Infarct-90 model and it is considered to spread out the region and move into the healthy tissue (Fig 6.10). No dummy material is present in the infarct as its volume fraction is replaced by the hydrogel.

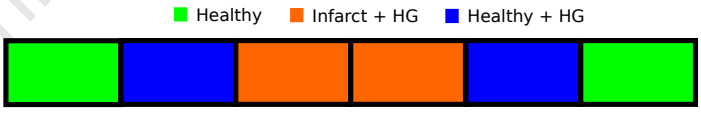

Figure 6.10: *Composite beam made up of healthy and infarct tissue with different hydrogel fractions*

6. Model: **Infarct+HG-x2 stiff**
   The stiffness of the hydrogel in the Infarct+HG model is increased to 30%.

The properties for the passive material response is given in table 6.1 while the active contraction material parameters are listed in table 5.3. Several output parameters are monitored, including axial displacement, stress, strain and active tension are monitored at the tip and mid cross-section of the beam. The analysis consider two stages: (1) passive stretching emulating the diastolic elongation of the heart and active contraction, emulating systolic contraction.

6.4.1 Displacements

The central node, coinciding with the neutral axis, at the end tip of the beam is monitored for any longitudinal movements.

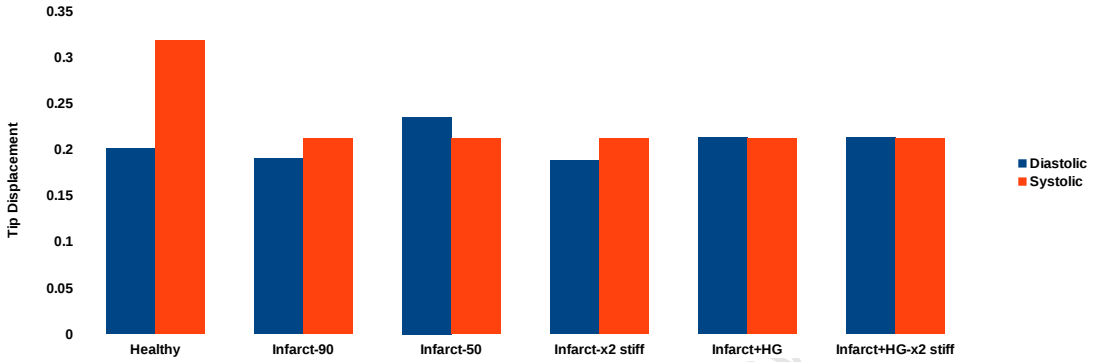

Figure 6.11: *Bar chart showing the different displacement results during the systolic and diastolic*

Once the beam is subjected to an infarct (region 3 and 4), the elongation in the diastolic phase is increased by 3.7% while those in the systolic contraction is lowered by 33% as it can be noted in Fig 6.11. The reason for such a difference in the first case might be due to the infarct region being more extensible during the expansion process as it is composed of a dummy material with very low stiffness. While in the second phase, since the infarct does not participate in the contraction process anymore, the overall active contraction force in the beam is reduced. These observations are confirmed by the fact that increasing the dummy volume fraction increases the displacement by 23% and doubling infarct stiffness of the infarct-50 model affects only the diastolic elongations with a decreased of 20%. If a 15% stiffness hydrogel is injected into the infarct, a minor decrease of 0.11% in displacement is obtained. This effect is as expected since the hydrogel increases the stiffness of the infarct, enabling the latter to better resist deformation. Increasing its stiffness to 30% will only induce a further reduction in displacement of 0.11%. During the systolic, there is no significant changes in displacement when compared with the Infarct-90 model since the volume of non-contractile material remained the same in all models expect the heatlhy one.

6.4.2 Stress

In this case, the stress is only studied as occurring in the mid-cross section.

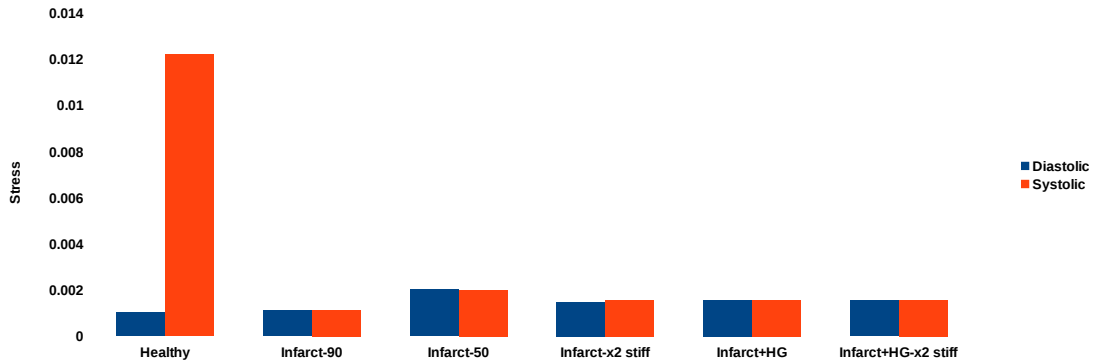

Figure 6.12: *Bar chart showing the different stress results during the systolic and diastolic*

The impact of an infarct results in an increase of 11% in fibre stress for the diastolic and a decrease of 91% for the systolic phase as shown in Fig 6.12. This increase is again attributed to the wall material loss due to dying myocytes and collagen degradation leading to a reduction of the material mixture and consequently larger strains, resulting in higher fibre stress. Increasing the dummy material fraction also translates into a 78.6% increase in fibre stress with respect to the Infarct-90 model. Doubling the infarct stiffness of the Infarct-50 model does not have a real impact on the stress as the material loss is the same in both models. However, if hydrogel is injected, the fibre stress decreases slightly by 0.5-1%. This can be explained by the fact that the hydrogel having replaced the material loss can now take some of the longitudinal loads. Using a hydrogel with double stiffness also brings an approximately 1% reduction in stress while incorporating an overlap region only slightly decreases the overall fibre stresses by 0.6%.

6.4.3 Strain

The strain along the MI beam is also investigated. The mid-node is chosen to monitor the variations among the models. A 90% infarct is found to cause an average increase of 55% in strain during the diastolic while a 100% decrease in strain in the systolic period. Having a twice stiffer infarct will lead to a drop in strain by 48% while increasing the volume fraction also increase the strain by about 79%. Adding hydrogel of either 15% or 30% stiffness only slightly reduces the strain by 0.27%.

Chapter 7

Application to Heart Modelling

7.1 Introduction

In the following, an idealised canine left ventricle (LV) in its healthy and infarcted stage are investigated. The analysis will focus on the elastic compliance during filling and the evolution of the fibre stress/strain during the diastole and systole. The results will highlight the differences in deformation behaviour, of the healthy case, caused by the infarct. All simulations will be carried out using both LME and MLS, where the latter will serve as a basis of reference. The end result will therefore give an indication if LME can be used to predict the response of 3D non-linear anisotropic material.

7.2 Problem definition

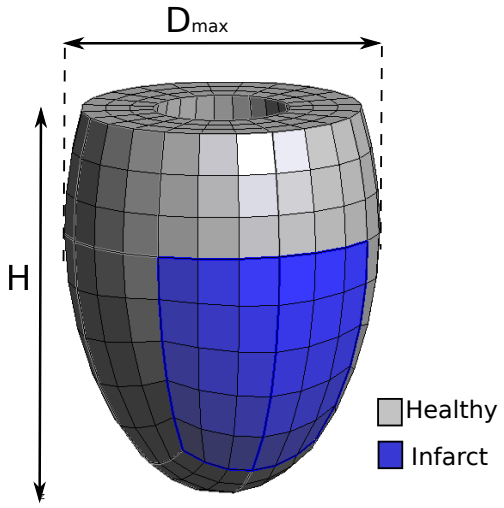

H = 78.1 cm
D_{max} = 44.62 cm
η_{epi} = 0.68
η_{endo} = 0.37
Cavity volume = 40000 mL
Infarct fraction = 14%
Elements = 684
Nodes = 549

Figure 7.1: *Problem definition using the left ventricle ellipsoid*

Two canine models have been defined (as described in Appendix B) with the same dimensions and mesh configuration as shown in Fig 7.1. The first problem is a healthy model, where the ventricle can undergo passive expansion and active contraction. The material properties is listed in table 5.1(b) on page 46 for the passive behaviour and table 5.3 on page 50 for the active one. In the second model, part of the ellipsoid has lost its contractibility due to an infarction marked in blue as shown in Fig 7.1. As mentioned before in section 5.1.3.2, a necrotic stage of the infarction is investigated and the infarct tissue is twice as stiff as a typical tissue (Gupta et al. [37]), where the stress scaling factor takes $C_{\text{inf}} = 1.76$. The infarct region is also defined to consist of 90% infarct volume fraction and 10% of a dummy material with very low stiffness, using the Neo-Hookean material law with $\mu = 0.246$ and $\lambda = 9.836$, to simulate the loss in material.

Regarding the boundary conditions, they have been applied in such a way as to imitate the deformation of the LV in a real heart. Thus, the Dirichlet boundary constraints are imposed only at the base (Fig 7.2(a)) in order to allow free movement of the apex. On the other end, the Neumann boundary conditions are represented by a uniform pressure of 1 kN/m^2 is applied to the endocardium as shown in Fig 7.2(b).

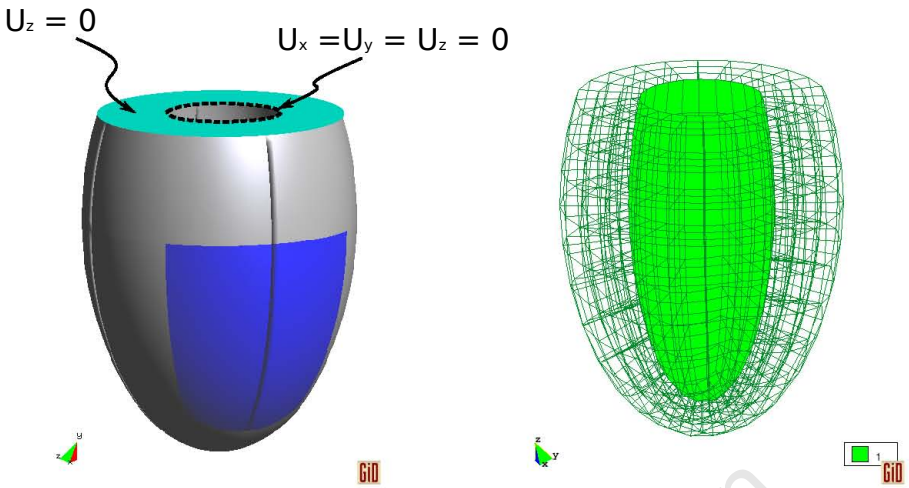

(a) (b)

Figure 7.2: *Applied boundary conditions : (a) Dirichlet BC (b) Pressure BC*

7.3 Results

The following simulated results using LME are presented and afterwards, the difference between MLS and LME is looked at using the calculation times and the results of the LV.

7.3.1 Cavity Pressure-Volume Relationship

At first we looked at the cavity volume with respect to its inner pressure. The graph shown in Fig 7.3 illustrates the diastolic phase.

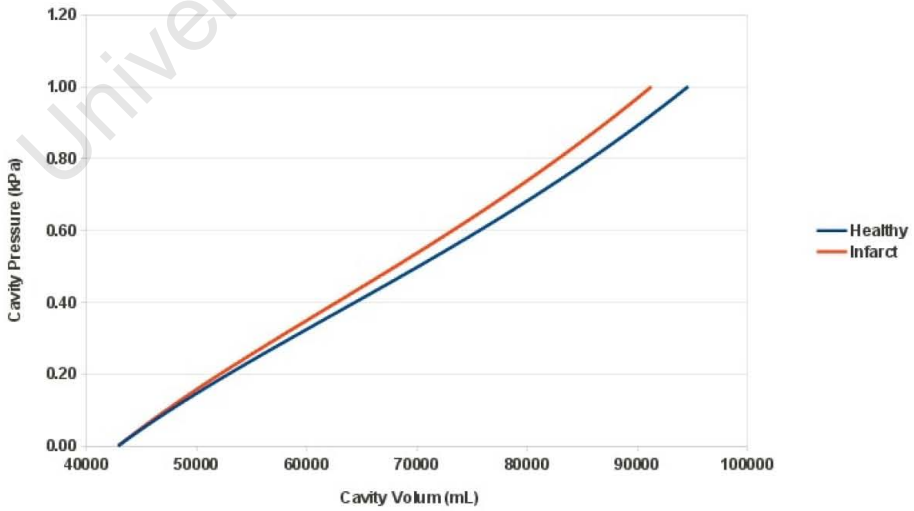

Figure 7.3: *Pressure-Volume plot of a healthy and infarcted left ventricle in the diastolic phase*

The end-diastolic volume (EDV) recorded from the healthy model is 94624 mL, which represent a 120% increase of its original volume. If the infarcted ventricle is now subjected to

the same pressure, the final volume will be lower, with 91306 mL, suffering a 3.5% decrease compared to the healthy case. In terms of the heart mechanics, this means that the Lv is impaired. The reason that may cause the change in volume can be attributed to the fact that the stiffness of the infarct, being much higher, limits stretching in the infarct tissue.

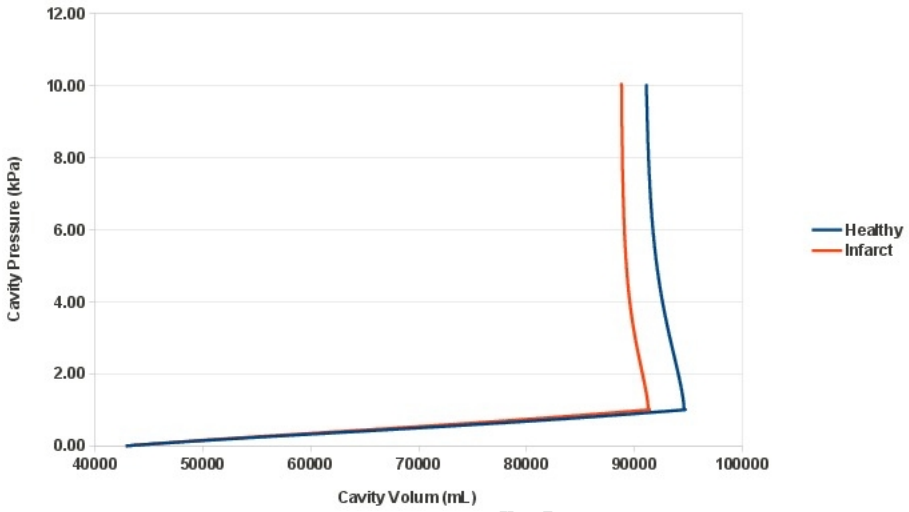

Figure 7.4: *Pressure-Volume plot of a healthy and infarcted left ventricle in the diastolic and systolic phase*

During the systolic stage, the difference in cavity volume, built-up at the EDV, has remained the same even though the pressure is increased to 10 kPa (shown in Fig 7.4). The ESV of the healthy and infarcted ventricle are 91125 ml and 88817 ml respectively.

7.3.2 Deformation and Fibre strains

The final deformation of the idealised left ventricle is shown in Fig 7.5 for both the healthy and infarct model during the diastole (Fig 7.6(a) and Fig 7.6(b)) and systolic phase (Fig 7.7(a) and Fig 7.7(b)). In order to clearly clearly see the difference in the final geometry with respect to the initial/reference configuration of the LV, Fig 7.5 is presented.

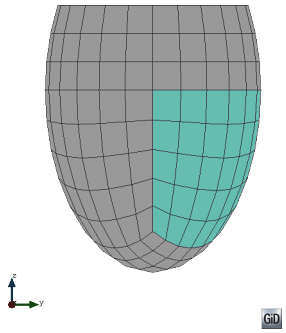

Figure 7.5: *The reference and undeformed configuration*

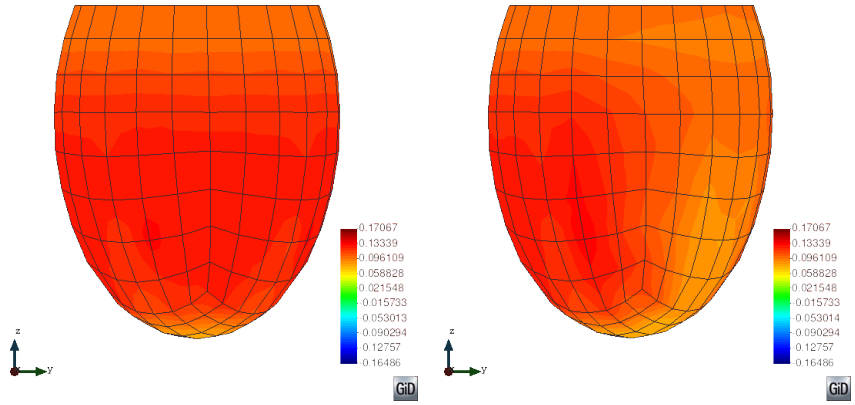

(a) (b)

Figure 7.6: *The fibre strain contour plot of the deformed LV in the diastolic phase with the healthy on the right and infarcted LV on the left*

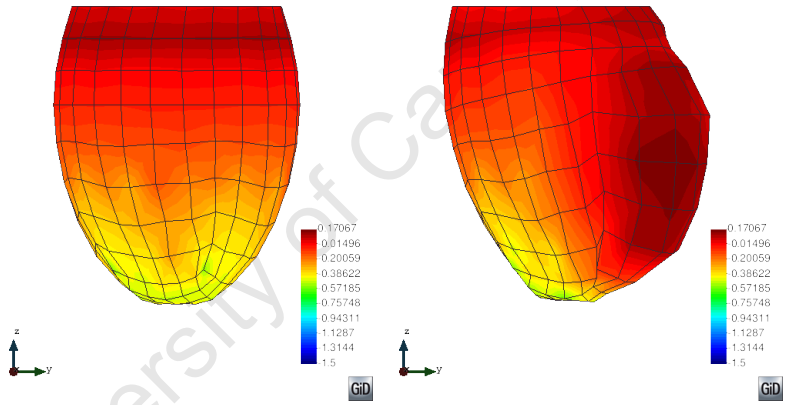

(a) (b)

Figure 7.7: *The fibre strain contour plot of the deformed LV in the systolic phase with the healthy on the right and infarcted LV on the left*

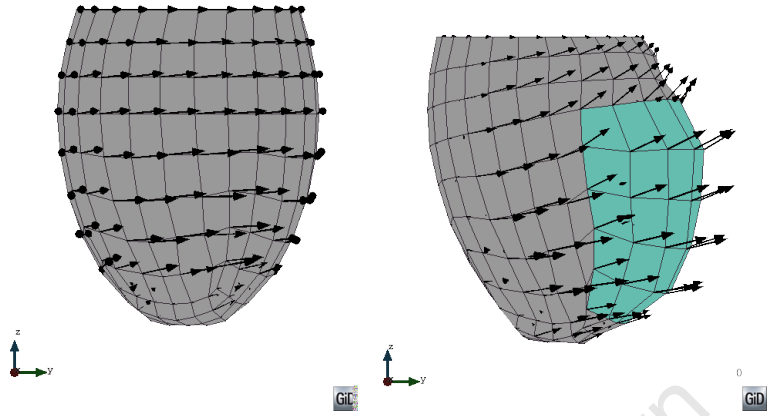

(a) (b)

Figure 7.8: *The displacement vector of the deformed LV in the systolic phase with the healthy on the right and infarcted LV on the left*

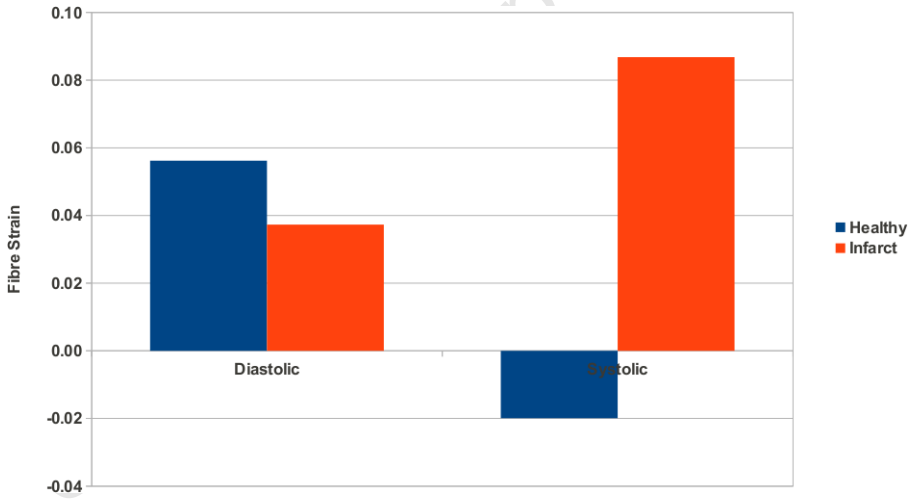

Figure 7.9: *Bar chart showing the fibre strain during the diastolic and systolic phases*

During the diastolic stage, the healthy LV undergoes filling which results in an expansion. Moreover, a rotatory movement can be observed due the anisotropically defined passive strain energy function. As these two effects occur simultaneously, the geometry seems to unfold itself as shown in Fig 7.6. However, in the infarcted LV, the deformation is not rotational symmetric. The high stiffness infarct region hampers the movements. Hence, the strain, at this region, is 33% lower than in the healthy case as illustrated in Fig 7.9.

In the systolic phase, isovolumetric contraction takes place. Since the cavity volume does not change, the tension developed by the sarcomere causes the healthy myocardium to be compressed. Being affected by the transversely isotropic properties of the material, a twisting effect is also observed with the displacement vector being almost parallel to the epicardium (as shown

in Fig 7.8). In the presence of an infarct, the deformation of the ventricle is seriously altered. Because the infarct tissue does not participate in the contraction process, the high pressure build-up inside the cavity pushes the infarct region out of the ventricular wall's plane. Hence, the left ventricle shown on Fig 7.7 is shifted towards the infarct direction while causing the bulging deformation. With large stretching of the infarct tissue occurring, the strain recorded is 5 times higher than in the healthy LV model.

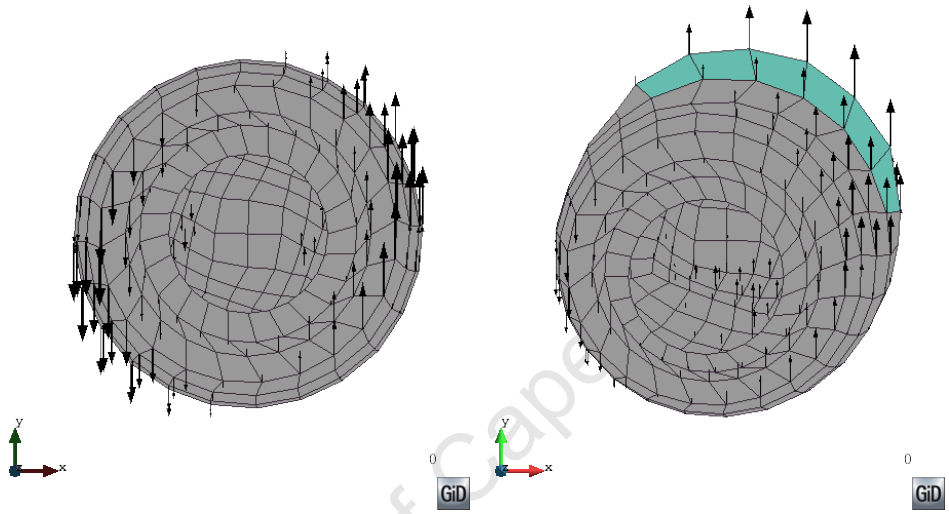

(a) (b)

Figure 7.10: *The displacement vector along the y-direction of the deformed LV in the systolic phase with the healthy on the right and infarcted LV on the left*

One additional observation that is worth mentioning regards the rotation effect. It has been found that the infarct bulging, prevent the proper twisting movement of the LV. On Fig 7.10, it can be seen that the healthy myocardium pushes the infarct region on the left-end side while pulling on the right-end side. Hence, the rotational movement is slightly affected by the whole bulging effect.

7.3.3 Fibre stress

The fibre stress have been recorded at multiple points in the infarct region. They have been averaged and displayed in Fig 7.11.

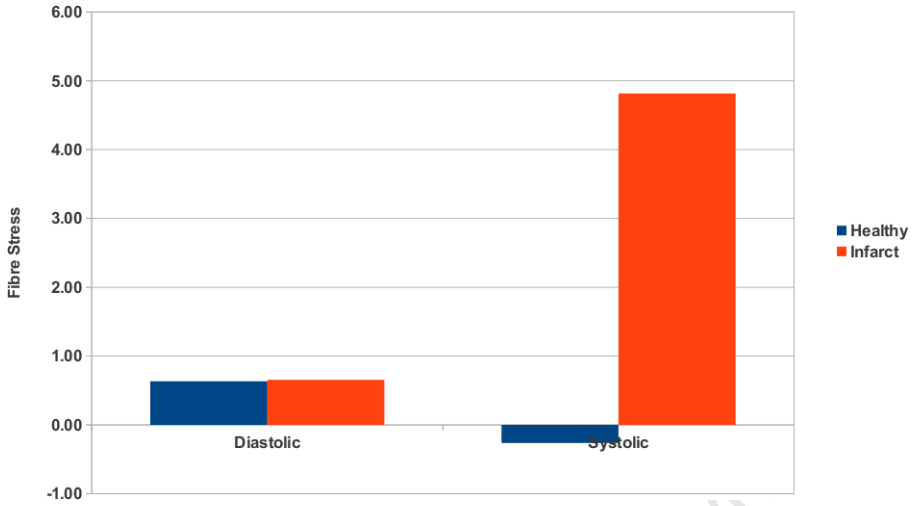

Figure 7.11: *Bar chart showing the fibre stress during the diastolic and systolic*

During the diastolic stage, the fibre stress in the infarct increases very slightly, by 3% only, compared to the healthy tissue. Such an increase is expected due to the material loss effect. But in the systolic stage, the stresses have undergone dramatic changes as displayed in Fig 7.11. The difference from contraction to expansion shows that the fibre stresses jump by more than 19 times. Such large increase is attributed to the bulging effect. With large stretching taking place in the infarct region and the high end systolic pressure, the stresses are more likely to increase as the wall thickness decreases.

7.3.4 Comparison of LME with MLS

In the followings, the results of LME are compared with those computed using MLS but focusing on the calculation time and the difference in stress and strain results from the LV.

7.3.4.1 Calculation Time

The calculation time of both methods have also been compared since Arroyo and Ortiz [1] reported a reduction in the calculation time when using LME basis with their benchmark problems. In this project, the overall calculation time, including the duration of a calculation step and the equations solving time, are analysed and illustrated in the following charts.

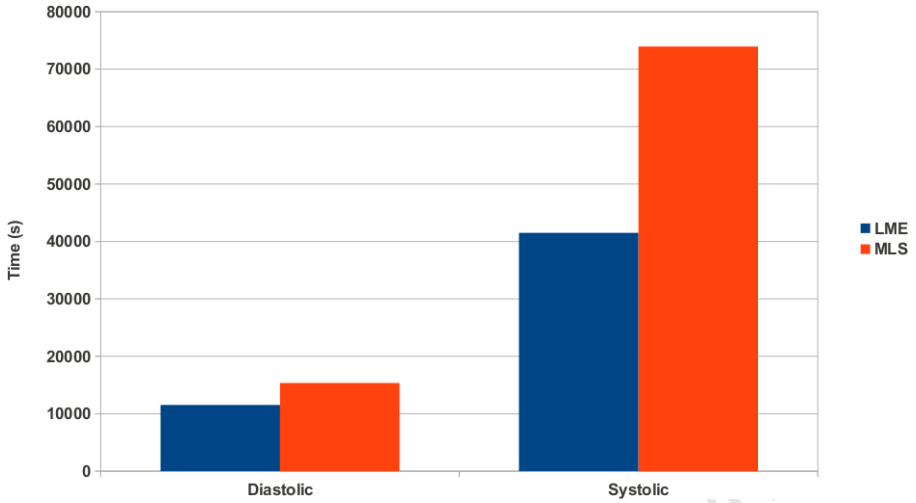

Figure 7.12: *Bar Chart showing the time taken to carry out the whole calculation when using LME and MLS in the diastolic and systolic stage*

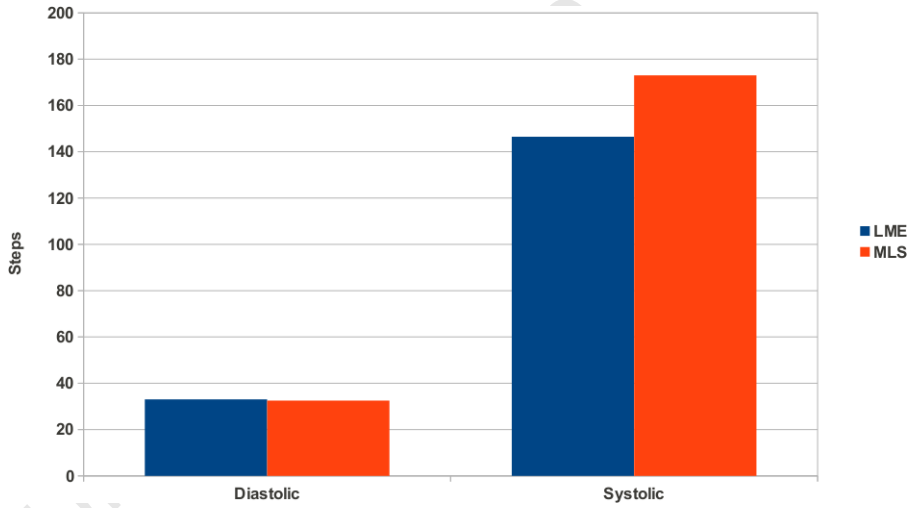

Figure 7.13: *Bar Chart showing the difference in loading steps for LME and MLS at each calculation stage*

The duration of most calculations, shown in Fig 7.12, are much shorter for LME compared to MLS. For example, LME is 25% and 43% quicker in the diastolic and systolic stage respectively. This corresponds to a decrease in 40% of the whole calculation time. One cause of such short processing time is due to the fact that LME required, on average, less than 15% of calculation steps compared to MLS in the systolic phase as presented in Fig 7.13. But in the diastole, even though the total steps are the same, MLS is still slower. In that case, the explanation can be found in looking at the running time of each single steps. Although LME required 10% more time when solving the equation system, its discrete equation assembly is done in 34% less time. In that case, each calculation step is carried out within a 24% lower calculation time.

7.3.4.2 Results Difference

The different results produced by LME and MLS are compared. They consist of the Pressure-Volume relationship, the fibre stress/strain and the displacement.

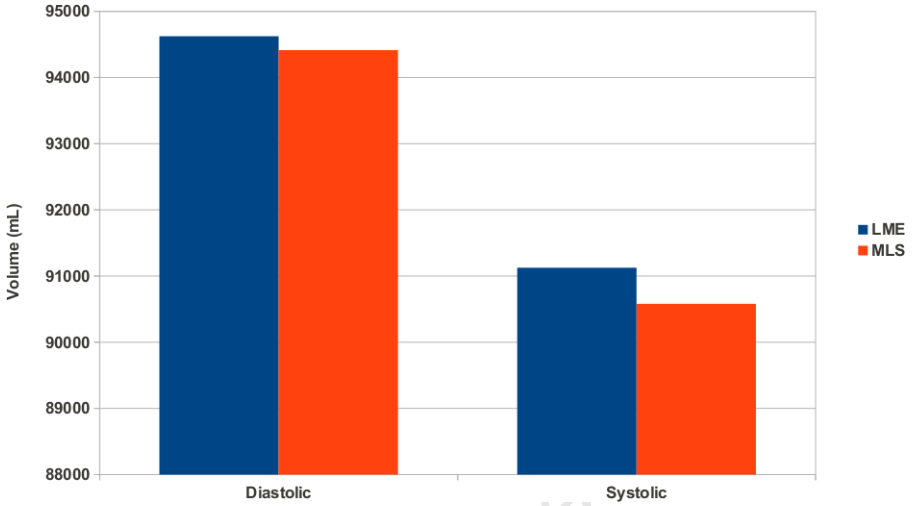

Figure 7.14: *Plot of End-Diastolic and End-Systolic volume for LME and MLS*

As experimental data shows varying values in the EDV and ESV, the focus is shifted to looking at the behaviour of the approximation methods with respect to each other. Based on the results in Fig 7.14, the EDV and ESV of LME are found to be higher than MLS. These results are expected, as in the benchmarking test, LME shape functions produce a less rigid stiffness matrix compared to MLS and therefore allow for more deformations.
Overall, LME's stresses and strains are lower. For example in the diastolic stage, the average stress has decreased by 10% and the strains by 4%. In the systolic stage, these differences are larger as the stresses decrease by 14% and its corresponding strains by 51%.

7.3.5 Unstructured Mesh

Before using the actual mesh configuration, the use of a more realistic geometry which require an unstructured mesh, where the nodes were randomly scattered and the nodal spacings varied, was initially attempted. A model using tetrahedral elements comprising of 2160 nodes and 8958 elements was defined and the full diastolic calculation was first carried out on a healthy model. The results obtained were then analysed as follows:

1. The deformation of the healthy model is expected to be uniform with a rotational symmetric expansion of the LV. But that is not the case for LME, as compared to MLS. Several regions with highly non-smooth and non-continuous solution are scattered over the ellipsoid in the LME case. Some dented surface can be seen in the upper right corners of Fig. 7.15(a) as well as in the surrounding region of the apex.

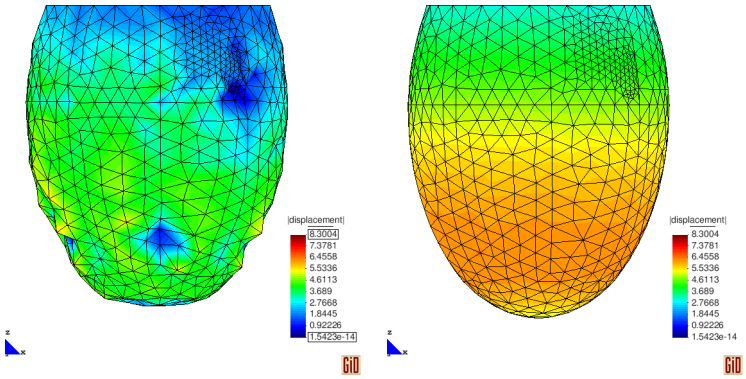

(a) (b)

Figure 7.15: *Displacement plot in the deformed configuration using (a) LME and (b) MLS*

2. The stress is also directly affected as indicated in Fig 7.16 . They are mostly of lower magnitude over the geometry, specially in regions where the surface is badly deformed.

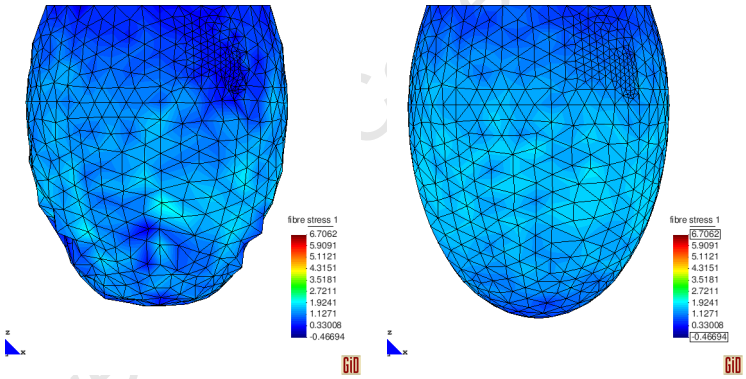

(a) (b)

Figure 7.16: *Stress contour plot in the deformed configuration using (a) LME and (b) MLS*

3. The strains obtained is also quite similar to the stress results (Shown in 7.17).

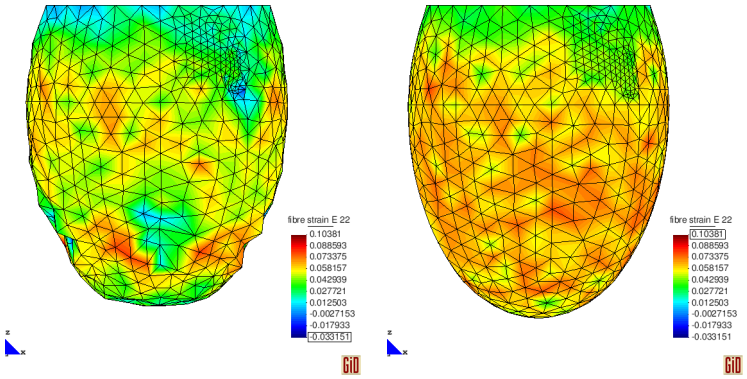

(a) (b)

Figure 7.17: *Strain contour plot in the deformed configuration using (a) LME and (b) MLS*

From the above set of diastolic results, the next calculation stage, which represent the systolic phase, is carried out. But due to the non-uniform deformation of the geometry in the LME calculated models, some numerical difficulties are encountered during the process which does not allow the calculation to proceed. Consequently, the use of the geometry has been discarded.

An alternative option has also been looked at, where the infarct region is more properly defined along with an overlap-zone (black region), as illustrated in Fig 7.18. In this case, the model is discretized with tetrahedral elements consisting of 731 nodes and 2731 elements. The size of the elements is smaller around the infarct region and border-zone but coarser in the rest of the LV so as to capture a maximum details of the solution at the point of interest. The simulation is then run through for a healthy LV in the diastolic stage and the deformation, shown in Fig 7.19, is obtained.

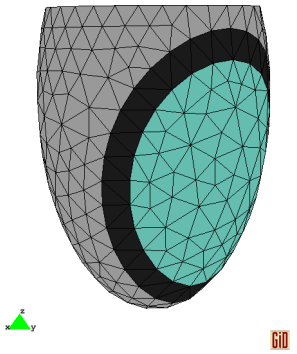

Figure 7.18: *Problem definition of unstructured LV with a redefined infarct region*

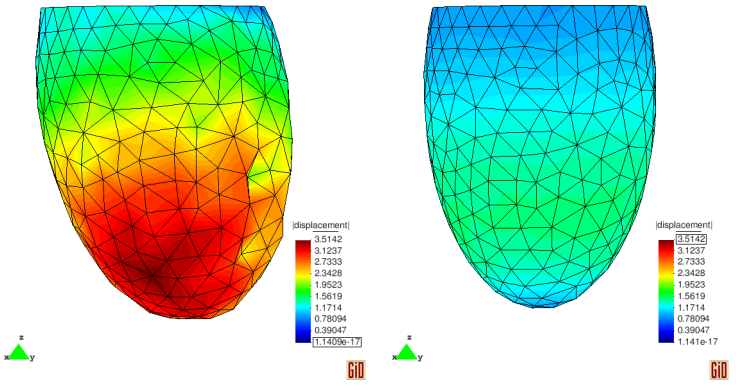

(a) (b)

Figure 7.19: *Displacement plot in the deformed configuration using (a) LME and (b) MLS*

With the distribution of the different mesh sizes being non-uniform and the nodes configuration being unstructured, the deformation can be considered to be worse than the one obtained in the previous unstructured LV ellipsoid model. Here in Fig 7.19(a) , the LV partly shifts on the right for no particular reason with a few dented results. The fibre stress and fibre strains are also affected. This can be seen particularly at the top right of Fig 7.20 and Fig 7.21

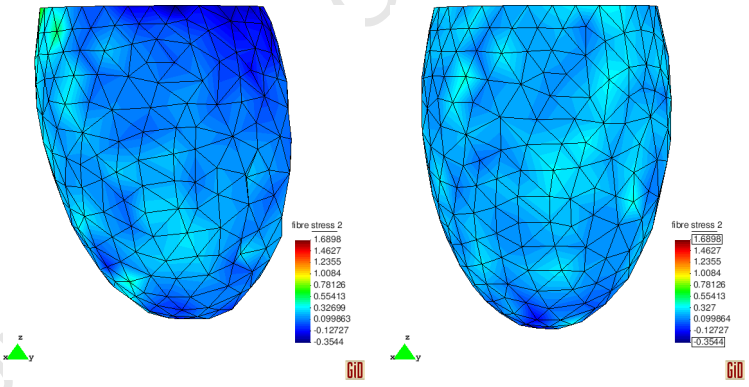

(a) (b)

Figure 7.20: *Stress contour plot in the deformed configuration using (a) LME and (b) MLS*

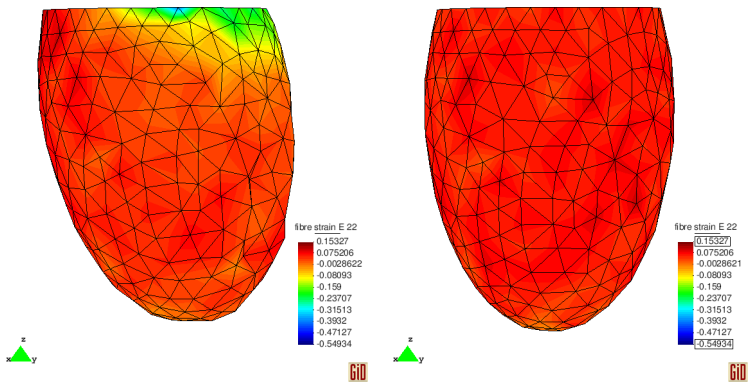

(a) (b)

Figure 7.21: *Strain contour plot in the deformed configuration using (a) LME and (b) MLS*

As can be seen in the two examples, the approximation of LME is badly affected when the nodal spacing is no longer constant. Such results have also been encountered in the unstructured cantilever beam problem (Section 6.2 on page 55) where a degradation in accuracy is noted. Thus, these results confirm the high sensitivity of LME with respect to the mesh configuration. This effect mostly arises due to the term β which is used in defining the LME scheme. With β being dependent on the nodal spacing, choosing its adequate value over an unstructured domain is challenging and may therefore require a more specific method as described in [21].

Chapter 8

Conclusion

The conclusion of this project can be broken down into two parts. That is, comparing LME with MLS and looking at the ability of LME to model a complex and non-linear problem.

8.1 Approximation

LME performed better than MLS in most tests. For example, the approximation power of LME is higher in the cantilever beam problem as it achieved a satisfactory level of accuracy. In the Cook's membrane problem, LME converges quicker to the right solution with a relatively coarse mesh discretisation, thus eliminating the need for large computational resources. In the analysis of the left ventricle, the convergence properties of LME is shown to be even more beneficial as it almost halved the calculation time. This feat is possible as its convergence rate is much faster and more stable. Additionally, this performance can also be attributed to the positive shape functions since processing these values can be carried out more efficiently by the computer, as opposed to having negative ones.

Even though LME shows some potential advantages over MLS, it needs to be carefully dealt with. Its sensitivity to nodal spacing seems to be its weakest point. An unstructured mesh, which is non-problematic for MLS, can be catastrophic for LME. This is mainly because the locality parameter, β, is defined to be indirectly proportional to the square of the distance between two nodes causing any variation to be magnified by the power coefficient. If $\beta(x)$ and its gradients are suitably approximated, the computation of LME is rendered more stable and the basis, more accurate with respect to a non-approximated beta. Therefore, it can be suggested that if the node discretisation problem is solved or at least stabilised, then the fast convergence rate, short calculation time and high approximation accuracy can make LME a more viable alternative to MLS.

8.2 Cardiac Mechanics behaviour of LV

The presence of a myocardial infarction has been demonstrated to cause an overall negative impact on the LV. From the obtained results, it has been shown that during the diastolic stage, the stress in the infarcted left ventricle is at an elevated level, which in extreme cases can cause a rupture, due to the presence of a dummy material. But with the infarct being stiffer, the strain and the cavity volume are highly reduced, leading to a lower end-diastolic volume.

In the systolic stage, the contraction of the LV is impaired. During the isovolumetric contraction phase, the increase in the cavity pressure caused the infarct region to move out of the left ventricle wall plane, forming a bulge. This demonstrated the compliance of the infarcted tissue to counteract the compliance of the healthy tissue. Meanwhile, the stress recorded in the infarct region is very high. The strain also followed similar pattern due to the large stretches induced by the bulging deformation. However, the change in volume between the healthy and infarcted LV are the same as at the end of the diastolic filling.

From these observations, it can be concluded that the high stress build up, due to tissue loss, is the most problematic factor that would affect the left ventricle and cause a wall rupture. If the impact of this effect can be reduced during the necrotic phase, then the healing process of the heart will improve as will also prevent adverse effects due to remodelling. Hence, any treatment, that may recover the loss in collagen and healthy tissue, will be able to bring some positive effects to the LV.

Chapter 9

Future Work

Even though most problems were investigated for this study, a few still remain and have not been considered due to the limited time frame. Hence, they have been listed below along with a few ideas that have emerged during the study.

- **Increasing the order of approximation**
  The approximation of LME has been based only on the zeroth and first order approximation. However, increasing the order of the shape functions, by directly imposing it as a constraint during the formulation of the Lagrangian equation is not straight forward. Doing so naively results in an empty set of solutions, as demonstrated by Arroyo and Ortiz in [1], where the positivity of the shape functions and the zeroth order condition can no longer hold. A first solution to this problem was proposed by Cyron et al. [10] through the relaxation of the quadratic constraint. They introduced a gap function that is similar to the one used in quadratic B-spline approximation but which can only manage to produce second order shape functions. A different method investigated by Bompadre et al [38] modified the locality scheme in the LME formulation by introducing a non-negative width function and eliminating the non-negativity constraints. Even though they successfully developed shape functions of different orders, the latter produced negative basis near the end of the influence zone (similar to MLS) and could no longer satisfied the Kronecker delta properties, making the imposition of the boundary conditions difficult. Another paper by Gonzalez et al [39], developed a method that make use of the De Boor's algorithm for B-spline surfaces, by coupling shape functions of different nodes at a specific point. The advantage of this method is that any order approximation can be achieved without any loss in LME's advantageous properties. Hence, this method can be regarded as an adequate solution of higher order approximation for LME basis.

- **Redefining β**
  One major drawback of LME is that its approximation accuracy is affected negatively once the mesh changes from a structured to an unstructured one. The reason that may cause this problem is that LME formulation depends on the term β which is inversely dependent on the spacing between the nodes. Even though Arroyo et al [1] defined a method that produces β of varying magnitude over a domain of randomly scattered particles, it was

too computationally expensive to be considered feasibly for large problems. Hence, two ways that may help in curbing the effect of β would be to either redefine it in such a way that it would no longer depend on the mesh size or investigate in the use of a different locality scheme that does not employ β.

- **Manipulating the Locality Scheme**
  The actual implemented Gaussian prior is quite flexible in changing the properties of the shape functions to accommodate for one's need without losing the essential characteristic properties of LME basis. One interesting idea that has been put forward is to produce anisotropic shape functions. This can be done by reformulating the Gaussian prior to include a constant metric tensor that will give a certain direction to the Gaussian decay profile. As in the case of the left ventricle which is a highly anisotropic problem, these shape function can be beneficial if a way is found to fill the G matrix with the 'b_{ij}' from the passive strain energy function.

- **Using a real heart geometry**
  Using a real heart geometry, whose coordinates has been extracted from MRI data, is possible. Obtained geometries would be much closer to those in a real healthy or infarcted heart. However, these kind of problems could be very challenging for LME since the nodes would obviously be arranged in a non-structural way unless mesh generators that can produce high quality elements are used.

- **Treatment simulations**
  With a working healthy and infarcted model in hand, the next stage of the simulation can now include the treatment process. Several therapies have been developed by medical doctors and researchers worldwide. Even though much of them stay uninvestigated due to lack of specimen to carry out experiment, these models can eventually be used as an alternative method.

Bibliography

[1] M. Arroyo and M. Ortiz, "Local maximum entropy approximation schemes: as seamless bridge between finite elements and meshfree methods," *International Journal for Numerical Methods in Engineering*, vol. 65, pp. 2167–2202, 2006.

[2] T. Usyk and A. McCulloch. (2002, April) Computational methods for soft tissue biomechanics. Portable Document Format. University of California. San Diego. [Online]. Available: http://cmrg.ucsd.edu/Continuity/Documentation/Theory?action=AttachFile&do=get&target=Usyk2003.pdf

[3] J. M. Guccione and A. D. McCulloch, "Mechanics of active contraction in cardiac muscle: Part i–constitutive relations for fiber stress that describe deactivation," *J Biomech Eng*, vol. 115, no. 1, pp. 72–81, Feb 1993.

[4] Human Heart Pictures. (2012, September) Learn basic anatomy with human heart pictures. Website. [Online]. Available: www.humanheartpictures.net

[5] Mayo Clinic. (1998-2012) Hypertrophic cardiomyopathy. Website. Mayo Foundation for Medical Education and Research (MFMER). [Online]. Available: http://www.mayoclinic.com/health/medical/IM00586

[6] L. Robertson, "The adult figure skater's guide to all things muscular," April 2012. [Online]. Available: www.wikipedia.com

[7] J. Reiner, R.C, R. Djellouli, and I. Harari, "The performance of local absorbing boundary conditions for acoustic scattering from elliptical shapes," *Comput. Methods Appl. Mech. Engrg.*, vol. 195, pp. 3622–3665, 2006.

[8] E. W. Weisstein. (2012) Prolate spheroidal coordinates. Digital. MathWorld - A Wolfram Web Resource. [Online]. Available: http://mathworld.wolfram.com/ProlateSpheroidalCoordinates.html

[9] P. Lancaster and K. Salkauskas, "Surfaces generated by moving least squares methods," *Mathematics of Computation*, vol. 37(155), pp. 141–158, 1981.

[10] C. Cyron, M. Arroyo, and M. Ortiz, "Smooth, second order, non-negative meshfree approximants selected by maximum entropy," *International Journal for Numerical Methods in Engineering*, vol. 00, pp. 1–6, 2009.

[11] N. Sukumar and R. Wright, "Overview and construction of meshfree basis functions: From moving least squares to entropy approximants," *International Journal for Numerical Methods in Engineering*, vol. 70, pp. 181–205, 2007.

[12] S. De and K. Bathe, "The method of finite spheres," *International Journal for Numerical Methods in Engineering*, vol. 51, pp. 275–292, 2001.

[13] C. Duarte and J. Oden, "Hp clouds - a hp meshless method," *Numerical Methods for Partical Differential Equations*, vol. 12, pp. 673–705, 1996.

[14] E. Jaynes, "Information theory and statistical mechanics," *Physicla Review*, vol. 106(4), pp. 620–630, 1957.

[15] T. Usyk, R. Mazhari, and A. McCulloch, "Effect of laminar orthotropic myofiber architecture on regional stress and strain in the canine left ventricle," *Journal of Elasticity*, vol. 61, pp. 143–164, 2000, 10.1023/A:1010883920374. [Online]. Available: http://dx.doi.org/10.1023/A:1010883920374

[16] G. Mase, R. Smelser, and G. Mase, *Continuum Mechanics for Engineers*. CRC Press, 2009.

[17] S. Boyd and L. Vandenberghe, *Convex Optimization*, C. U. Press, Ed. Cambridge University Press, 2009.

[18] C. Shannon, "A mathematical theory of communication," *The Bell System technical Journal*, vol. 27(3), pp. 379–423, 1948.

[19] V. Rajan, "Optimatility of the delaunay traingle in R^d," *Discrete and Computational Geometry*, vol. 12(2), pp. 189–202, 1994.

[20] N. Sukumar and R.-B. Wets, "Deriving the continuity of maximum-entropy basis functions via variational analysis," *SIAM Journal on Optimization*, vol. 18(3), pp. 914–925, 2007.

[21] A. Rosolen, R. Millan, and M. Arroyo, "On the optimum support size in meshfree methods: a variational adaptivity approach with maximum entropy approximants," *International Journal for Numerical Methods in Engineering*, vol. 82, pp. 868–895, 2010.

[22] N. Sukumar, "Construction of polygonal interpolants: a maximum entropy approach," *International Journal for Numerical Methods in Engineering*, vol. 61, p. 21592181, 2004.

[23] M. Arroyo. (2012) Local maximum entropy matlab routine. Matlab code. Universitat Politcnica de Catalunya-BarcelonaTech. Jordi Girona 1-3 E-08034 Barcelona, Spain. [Online]. Available: http://www.lacan.upc.edu/arroyo/Site1/Research/Entries/2012/9/12_Maximum_entropy_approximation.html

[24] V. Fuster, R. O'Rourke, R. Walsh, and P. Poole-Wilson, *Hurst's the heart*. McGraw-Hill Co., 2007.

[25] J. W. Holmes, T. K. Borg, and J. W. Covell, "Structure and mechanics of healing myocardial infarcts." *Annual Review of Biomedical Engineering*, vol. 7, pp. 223–253, 2005.

[26] Z. Li and J. Guan, "Hydrogels for cardiac tissue engineering," *Polymers*, vol. 3, pp. 740–761, 2011.

[27] E. Tous, B. Purcell, I. J.L., and J. Burdick, "Injectable acellular hydrogels for cardiac repair," *Journal of cardiovascular translational research*, vol. 4, p. 528542, 2011.

[28] J. Kortsmit, N. Davies, R. Miller, J. Macadangdang, P. Zilla, and T. Franz, "The effect of hydrogel injection on cardiac function and myocardial mechanics in a computational post infarction model," *Computational Methods Bimech Biomed Eng*, 2012.

[29] J. Hill, "Partial solution of finite elasticity - three-dimensional deformations," *J Appl Math Phys*, vol. 24, pp. 609–618, 1973.

[30] S. Reese, T. Raible, and P. Wriggers, "Finite element modelling of orthotropic material behaviour in pneumatic membranes," *International Journal of Solids and Structures*, vol. 52, pp. 9525–9544, 2001.

[31] S. Klinkel, C. Sansour, and W. Wagner, "An anisotropic fibre-matrix material model at finiite elastic-plastic strains," *Computational Mechanics*, vol. 35, pp. 409–417, 2005.

[32] J. Guccione and A. McCulloch, "Passive material properties of intact ventricular myocardium determined from a cylindrical model," *ASME JOURNAL OF BIOMECHANICAL ENGINEERING*, vol. 113, pp. 42–55, 1991.

[33] R. C. P. Kerckhoffs, P. H. M. Bovendeerd, J. C. S. Kotte, F. W. Prinzen, K. Smits, and T. Arts, "Homogeneity of cardiac contraction despite physiological asynchrony of depolarization: A model study," *Annals of Biomedical Engineering*, vol. 31, pp. 536–547, 2003, 10.1114/1.1566447. [Online]. Available: http://dx.doi.org/10.1114/1.1566447

[34] S. Niederer and N. Smith, "The role of the frankstarling law in the transduction of cellular work to whole organ pump function: A computational modeling analysis," *PLoS Computational Biology*, vol. 5(4), 2009.

[35] J. Rijcken, P. H. Bovendeerd, A. J. Schoofs, D. H. van Campen, and T. Arts, "Optimization of cardiac fiber orientation for homogeneous fiber strain during ejection," *Ann Biomed Eng*, vol. 27, no. 3, pp. 289–97, May-Jun 1999.

[36] S. Skatulla, "Computational aspects of generalized continua based on moving least square approximations," Ph.D. dissertation, University of Adelaide, 2006.

[37] K. B. Gupta, M. B. Ratcliffe, M. A. Fallert, L. H. Edmunds, and D. K. Bogen, "Changes in passive mechanical stiffness of myocardial tissue with aneurysm formation," *Circulation*, vol. 89, pp. 2315–2326, 1994.

[38] A. Bompadre, L. Perotti, C. Cyron, and M. Ortiz, "Convergent meshfree approximation schemes of arbitrary order and smoothness," *Comput. Methods Appl. Mech. Engrg.*, vol. 221-222, pp. 83–103, 2012.

[39] D. Gonzalez, E. Cueto, and M. Doblare, "A higher order method based on local maximum entropy approximation," *Int. J. Numer. Meth. Engng*, vol. 83, pp. 741–764, 2010.

[40] T. Belytschko, Y. Y. Lu, and L. Gu, "Element-free galerkin methods," *International Journal for Numerical Methods in Engineering*, vol. 37, pp. 229–256, 1994.

[41] P. Bovendeerd, T. Arts, J. Huyghe, D. Van Campen, and R. Reneman, "Dependence of local left ventricular wall mechanics on myocardial fiber orientation: a model study," *Journal of biomechanics*, vol. 25, no. 10, pp. 1129–1140, 1992.

[42] G. Buckberg, J. Hoffman, A. Mahajan, S. Saleh, and C. Coghlan, "Cardiac mechanics revisited : The relationship of cardiac architecture to ventricular function," *Journal of the American Heart Association*, vol. 118, pp. 2571–2587, 2008.

[43] O. Cakmakci, G. Fasshauer, H. Foroosh, K. Thompson, and J. Rolland, "Meshfree approximation methods for free-form surface representation in optical design with applications to head-worn displays," in *Proc. of SPIE*, 2008.

[44] P. Colli Franzone, L. Guerri, and S. Rovida, "Wavefront propagation in an activation model of the anisotropic cardiac tissue: asymptotic analysis and numerical simulations," *Journal of Mathematical Biology*, vol. 28, pp. 121–176, 1990, 10.1007/BF00163143. [Online]. Available: http://dx.doi.org/10.1007/BF00163143

[45] G. Fasshauer and J. Zhang. Iterated approximate moving least squares approximation. Portable Document Format. Department of Applied Mathematics. Illinois Institute of Technology. [Online]. Available: http://www.math.iit.edu/~fass/Lisbon05.pdf

[46] A. Gossler, "Moving least-squares: A numerical differentiation method for irregularly spaced calculation points," Sandia National Laboratories, Tech. Rep., 2001.

[47] J. M. Guccione, L. K. Waldman, and A. D. McCulloch, "Mechanics of active contraction in cardiac muscle: Part ii-cylindrical models of the systolic left ventricle." *ASME Journal of Biomechanical Engineering*, vol. 115, pp. 82–90, 1993.

[48] R. Kerckhoffs, S. Narayan, J. Omens, L. Mulligan, and A. McCulloch, "Computational modeling for bedside application," *Heart failure clinics*, vol. 4, no. 3, pp. 371–378, 2008.

[49] M. Kocica, A. Corno, F. Carreras-Costa, M. Ballester-Rodes, M. Moghbel, C. Cueva, V. Lackovic, V. Kanjuh, and F. Torrent-Guasp, "The helical ventricular myocardial band: global, three-dimensional,functional architecture of the ventricular myocardium," *European Journal of Cardio-thoracic Surgery*, vol. 29S, pp. S21–S40, 2006.

[50] D. Levin, "The approximation power of moving least-squares," *Mathematics of Computation*, vol. 67(224), pp. 1517–1531, 1998.

[51] G. Maisuradze, A. Kawano, D. Thompson, F. Albert Wagner, and M. Minkoff, "Interpolating moving least-squares methods for fitting potential energy surfaces: Applications to classical dynamics calculations," *Journal of Chemical Physics*, vol. 121 (21), pp. 10 329–10 338, 2004.

[52] D. Mann and M. Bristow, "Mechanisms and models in heart failure : The biomechanical model and beyond," *Journal of the American Heart Association*, vol. 111, pp. 2837–2849, 2005.

[53] M. McCourt, "A bayesian approach to determining a good shape parameter for meshfree approximation," January 2009. [Online]. Available: http://www.thefutureofmath.com/mathed/bayesrbf.pdf

[54] T. Most and B. C., "A moving least squares weighting function for the element-free galerkin method which almost fulfills essential boundary conditions," *Structural Engineering and Mechanics*, vol. 21(3), pp. 315–332, 2005.

[55] A. Nealen, "An as-short-as-possible introduction to the least squares, weighted least squares and moving least squares methods for scattered data approximation and interpolation," September 2012. [Online]. Available: http://www.nealen.net/projects/mls/asapmls.pdf

[56] J. H. Omens and Y. C. Fung, "Residual strain in rat left ventricle," *Circulation Research*, vol. 66, pp. 37–45, 1990.

[57] J. H. Omens, T. P. Usyk, Z. J. Li, and A. D. McCulloch, "Muscle lim protein deficiency leads to alterations in passive ventricular mechanics," *American Journal of Physiology-Heart and Circulatory Physiology*, vol. 282, no. 2, pp. H680–H687, Feb 2002.

[58] S. Schaefer, T. McPhail, and J. Warren, "Image deformation using moving least squares," *ACM Transactions on Graphics (TOG)*, vol. 25(3), pp. 533–540, 2006.

[59] N. Sukumar and A. Tabarraei, "Conforming polygonal finite elements," *International Journal for Numerical Methods in Engineering*, vol. 61, pp. 2045–2066, 2004.

[60] R. Tily and C. Brace, "A study of natural neighbour interpolation and its application to automotive engine test data," in *Proceedings of the Institution of Mechanical Engineers*, 2006.

[61] K. A. Tomlinson, "Finite element solution of an eikonal equation for excitation wavefront propagation in ventricular myocardium," Ph.D. dissertation, University of Auckland, 2000.

[62] K. Tomlinson, P. Hunter, and A. Pullan, "A finite element method for an eikonal equation model of myocardial excitation wavefront propagation," *SIAM Journal on Applied Mathematics*, vol. 63, no. 1, pp. 324–350, 2002.

[63] D. Weiss, D. Keller, G. Seemann, and O. Dossel, "The influence of fibre orientation, extracted from different segments of the human left ventricle, on the activation and repolarization sequence: a simulation study," *Europace*, vol. 9, pp. vi97–vi104, 2007.

[64] R. Raducanu, Ed., *Moving least squares method, revisited*, vol. 8, University Politehnica of Bucharest. Romania: Geometry Balkan Press, April 2002.

Appendix A

Seska

SESKA is a C++-based code build up on top of several libraries by Dr S. Skatulla since the start of the 2000s. It consists mainly in providing an almost complete solution of solving any set of equation system based on the Element Free Galerkin Method (EFG). This basically means that, the preprocessing, calculation process and post-processing are all carried out by the code itself with the exception of geometry definition and 3D solution visualisation. The latter is done in a pre/post-processing software package called GiD. Most of SESKA's processes are parallelised using the OpenMPI library, thus allowing large problems to be solved on high performance computers.

Once started, the work flow of SESKA is straight forward. It calculates the shape functions, build-up the stiffness matrix and/or mass matrix (for dynamic problems) and solve the set of equations either in a linear or non-linear way, depending on how the problem has been defined.

A.1 Shape Functions

Since SESKA employs the EFG method, it needs to primarily find the supporting nodes of all individual particles belonging to the domain. Actually two methods have been used. Either, all the nodal distances relative to a particular particle is calculated and nodes found within the defined radius of support are included in a support particle list, or, the elements connectivity, within a mesh, is used to find the neighbouring nodes. Regarding the influencing zone, SESKA defines them in a flexible way. For example, a geometry with different densities of scattered nodes have different supporting radius. Their shape is defined as either a cuboid or a sphere, with the influence radius being different in each direction (useful if shape functions are computed while taking the anisotropic material properties into consideration). After finding all supporting nodes, the MLS method is then employed to calculate the shape functions and its derivatives.

A.2 Calculation

The calculation process is carried out using external libraries coupled with the constitutive laws setup in SESKA. The actual version of the code uses the following packages:

BLAS Basic Linear Algebra Subprogram is a set of code that allows a user to perform simple vector and matrix manipulation. The library is ordered in 3 levels. Level 1 allows a vector-vector multiplication, Level 2, a vector-matrix multiplication and level 3, a matrix-matrix multiplication.

LAPACK Linear Algebra PACKage is code library written in Fortran for numerical linear algebra. It can solve systems of linear equations, eigenvalue problems and single value decomposition. Moreover, functions for matrix factorisation and decomposition is also available. Lapack heavily relies on the BLAS libraries to carry out the matrix calculation efficiently.

ParMETIS The ParMETIS library contains several algorithms which can split a structured or unstructured meshed domain, during parallelisation, in an effective way that produces better sparse matrices.

PETSc The Portable, Extensible Tool-kit for Scientific computation set are libraries that allows BLAS, Lapack and MPI to work together. It naturally inherits the capability of solving linear equation systems but also add the functionality of working with non-linear ones. Moreover, different partial differential equations can be solved for. Another useful features that Petsc brings along are the pre-conditioners. The latter typically enhance a matrix in such a way that it behaves nicely during the calculation process thus reducing the risk of encountering numerical difficulties and the solving time in certain cases.

Appendix B

The canine LV ellipsoidal model

B.1 Parametric Equation

The equations of the canine ellipsoidal LV has been derived based on parameters extracted from Bovendeerd et al [41] and that fitted in the Spheroid Prolate Coordinate (section 5.5.1) equation system. In that paper, the authors used experimental data extracted from a canine ventricle and suggested the followings parameters:

Parameters	Values
H(mm)	24.8
a(mm)	43.0
η_{epi}	0.68
η_{endo}	0.37

Table B.1: *Kerckhoff's parameters for a canine ellipsoid ventricle*

where H is the height of the base from the centre of the ellipse, a is the prolate constant and η_{epi} and η_{endo} are the parameters that defines the walls of a ventricle. Based on these values, a set of parametric equations is derived and used in GiD to generate the ellipses of the geometry. Firstly ϕ is set to 0. This helps in drawing a 2D geometry of the endocardium and epicardium ellipses. Consequently, the corresponding x and z coordinates are found.

Considering the endocardium case,

$$\begin{aligned} x &= a\ \sinh\eta\ \sin\theta\ \cos\phi \\ &= a\ \sinh\eta\ \sin(90)\ \cos(0) \\ &= a\ \sinh\eta \end{aligned} \tag{B.1}$$

With the endocardium radius of 2.4 mm at $\mu = 0.37$

$$\begin{aligned} x &= 43 \sinh 0.37 \\ &= 16.28 \end{aligned} \tag{B.2}$$

And along the z-axis,

$$\begin{aligned} z &= 43 \cosh 0.37 \\ &= 43.98 \end{aligned} \tag{B.3}$$

For the epicardium case, the above procedure is repeated with a radius of 5.1 mm and $\mu = 0.68$. Table B.2 summarises the values of the spheroidal prolate coordinate system unknowns obtained so far.

Location	x	z
Epicardium	16.28	43.98
Endocardium	31.55	53.33

Table B.2: *Parametric Equation's constants*

The spheroidal prolate equations now in hand, the latter needs to be converted into a set Cartesian equations for each axes. The equation of an ellipse is used and can be given by:

$$\left(\frac{x}{\upsilon}\right)^2 + \left(\frac{z}{\xi}\right)^2 = 1 \tag{B.4}$$

with

- υ : polar radius, related directly to the spheroidal prolate constant a
- ξ : maximum radius of either the endocardium or epicardium

Letting

$$\left(\frac{x}{\upsilon}\right)^2 = t \tag{B.5}$$

the equation corresponding to the x-axis is:

$$x(t) = \upsilon\sqrt{t} \tag{B.6}$$

On the other end, if z is made subject of formula in eq B.4,

$$\begin{aligned} \left(\frac{z}{\xi}\right)^2 &= 1 - \left(\frac{x}{\upsilon}\right)^2 \\ z &= \xi^2\sqrt{1 - \left(\frac{x}{\upsilon}\right)^2} \end{aligned} \tag{B.7}$$

Applying eq B.5,

$$z(t) = \xi^2\sqrt{1-t} \tag{B.8}$$

Therefore the set of Cartesian equations is

$$\begin{aligned} x(t) &= \upsilon\sqrt{t} \\ y(t) &= 0 \\ z(t) &= \xi^2\sqrt{1-t} \end{aligned} \tag{B.9}$$

while the parametric equation being

$$f(t) = \left(\upsilon\sqrt{t}\,,\, 0\,,\, \xi^2\sqrt{1-t}\right) \tag{B.10}$$

B.2 Drawing

Making use of the parametric equation derived from the previous section, the left ventricle ellipsoidal geometry is built-up. The ellipses representing the epicardium and endocardium in 2D is drawn and ϕ is set to zero. The arc spanned from the positive to the negative region of the z-axis. A horizontal line, parallel to the x-axis is drawn at a height of 24.8 mm from the centre of the ellipse. The line typical crosses through the wall of the ellipse, representing the base of the LV ellipsoidal model. All the lines, belonging to the ellipses, are trimmed off if they are found above the base line. The resulting shape is shown in Fig B.1(a). From the 2D geometry, the 3D one is built. The actual lines are simply rotated 360° around the z-axis, forming the surfaces and volume of the ellipsoid (Fig B.1(b)).

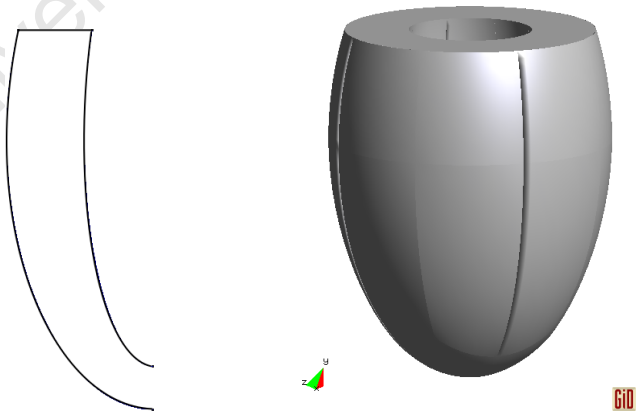

(a) (b)

Figure B.1: *Canine Ellipsoidal model : (a) Half 2D geometry and (b) Full 3D ellipsoidal geometry*

The 3D geometry of a healthy LV with an infarct is shown in Fig B.2 (infarct represented by blue region). This is achieved by splitting the geometry into several smaller volumes in order

to specify the infarct region and also help GiD in creating elements of better quality during the meshing process. The final geometry looked as follows:

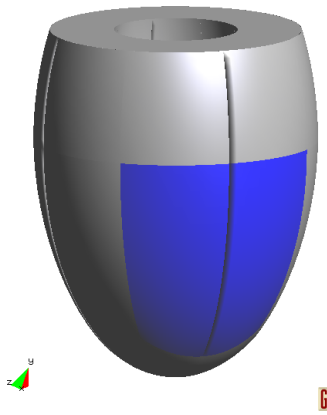

Figure B.2: *Ellipsoidal geometry with a infarct region defined*

B.3 Meshing

The geometry is then meshed using hexahedral elements in a non-uniform way in order to cater for different surfaces and the curved shape of the apex. Different meshing options are used from GiD, to increase the overall quality of the elements in order to reduce numerical difficulties as well as to increase smoothness in the final results. The final mesh obtained is given in Fig B.3 with a discretisation of 684 elements and 549 nodes.

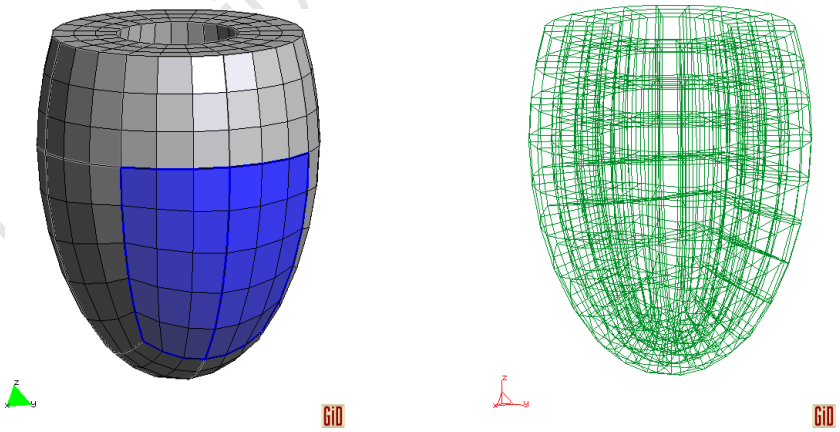

(a) (b)

Figure B.3: *Meshed ellipsoidal model : (a) Rendered view and (b) Plane view*

B.4 Boundary Conditions

Starting with the Dirichlet (Essential) boundary conditions, observations of an actual heart-beat movements revealed that the whole ventricle undergoes vertical, horizontal and transversal

movements except at the base. There, the heart muscles stay almost fixed along the vertical direction. In addition, it has been also noted that the endocardium at this position remains roughly stationary. Therefore, the followings are specified:

- The movement of the base surface (Fig B.4(a)) is restrained along the z-axis
- The inner ring (intersection of the base with the endocardium wall, as shown in Fig B.4(b)) is fixed in all 3 directions.

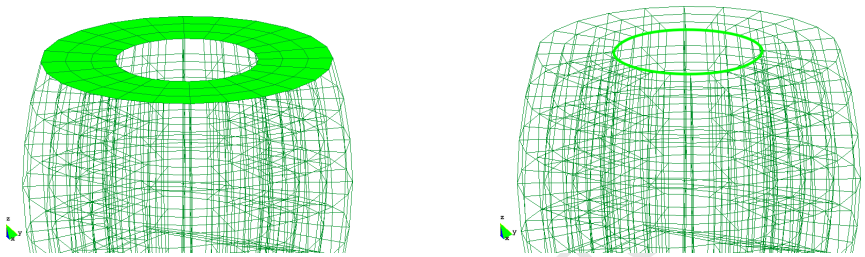

(a) (b)

Figure B.4: *Essential boundary condition applied at the base : (a) surface constrained in the z-direction (b) epndocardium line constrained in all 3 directions*

Regarding the Neumman boundary conditions, a surface pressure of 1 kPa is applied along the endocardium wall. The direction of the force at any point act perpendicular to the surface pointing in the outward direction (away from the cavity volume, Fig B.5), representing the diastolic filling.

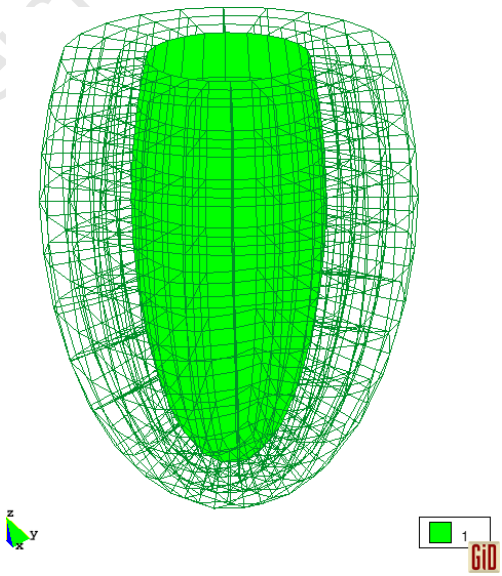

Figure B.5: *Pressure load applied along the endocardium*